Magnetization Dynamics and Spin Transfer Effect in Nanometric Spin Valves

Christel Berthelot

To cite this version:

Christel Berthelot. Magnetization Dynamics and Spin Transfer Effect in Nanometric Spin Valves. Other [cond-mat.other]. Université de Lorraine, 2012. English. NNT : 2012LORR0076 . tel-01749237

HAL Id: tel-01749237
https://hal.univ-lorraine.fr/tel-01749237v1

Submitted on 29 Mar 2018

U.F.R Faculté des Sciences et Technologies
École doctorale EMMA
D.F.D Physique, spécialité Nanociences

Thèse

pour obtenir le grade de

Docteur de l'Université de Lorraine

en Physique

par Christel BERTHELOT

Modélisation de la dynamique d'aimantation par effet de transfert de spin dans des vannes de spin de taille nanométrique

Soutenue publiquement le 9 juillet 2012 devant le jury composé de :

Président du Jury:	M. Dragi Karevski	Professeur de l'Université de Lorraine
Rapporteur:	M. Vincent Jeudy	Professeur de l'Université de Cergy Pontoise
Rapporteur:	M. Denis Ledue	Professeur de l'Université de Rouen
Invité:	M. Daniel Lacour	Chargé de recherches CNRS à l'Université de Lorraine
Directeur de thèse:	M. Stéphane Mangin	Professeur de l'Université de Lorraine

Thèse préparée au sein de l'Institut Jean Lamour, UMR CNRS 7198, Université de Lorraine, France

Table des matières

I État de l'art 15

II Modèle macrospin 59

III Dynamique d'aimantation à l'aide de diagrammes d'état 87

Remerciements

Ce travail a été en partie réalisé à l'Institut Jean Lamour de Nancy. Je remercie Monsieur Jean-Marie Dubois, le directeur de l'Institut Jean Lamour de Nancy et Monsieur Michel Vergnat, le directeur du département de Physique de la Matière et des Matériaux, pour leur acceuil.

Je remercie de même Monsieur Andrew Kent de son accueil au laboratoire de la matière condensée à New York University.

J'aimerais aussi remercier M. Dragi Karevski d'avoir présidé mon jury, ainsi que M. Vincent Jeudy et M. Denis Ledue d'avoir accepté d'être les rapporteurs de ce manuscrit. Je remercie également M. Daniel Lacour d'avoir participé à mon jury.

Tout d'abord je souhaite remercier mon directeur de thèse Stéphane Mangin pour son enthousiasme et sa bonne humeur ainsi que sa disponibilité, ce qui n'était pas toujours simple avec toutes ses responsabilités.

Je n'aurais jamais pu aller au bout de cette thèse sans tous les thésards, post-docs et ingénieurs que j'ai pu rencontrés au cours de ma thèse et qui m'ont soutenus : Clément, Anthony, Cédric, Sylvain, Julien, Matthias, Kaname, Albert, Michael, Sylvie, Alex, Christian, Hamid, Stéphane Suire, Damien, Ferran, Pradeep, Steve et Daniel avec qui j'ai fait de nombreuses pauses cafés. Je n'oublie pas Amina et Mathias (merci pour le thé).

Merci aux thésards du groupe de physique statistique pour toutes les soirées : Xavier, Mario et Nelson. Merci à Amandine, Aurélie et Émilie avec qui j'ai partagé des années d'études et un bureau pendant quelques temps, Mathieu avec qui j'ai passé de très bons moments à discuter sur des sujets divers.

Je souhaite aussi remercier Stéphanie avec qui j'ai beaucoup skypé pendant mon année à New York et qui était là pendant les moments de blues.

Un grand merci à Hanna avec qui je n'aurais finalement partagé qu'une année de thèse mais qui est très vite devenue une très bonne amie, merci de m'avoir supportée pendant la rédaction et d'avoir même changé de souris quand elle cliquait trop bruyamment.

Un aussi grand merci à Sophie, qui me supporte depuis la L2 (même si théoriquement on ne se parle vraiment que depuis le M1), avec qui on a fait de nombreuses soirées ciné et sorties. Mes remerciements pourraient être plus longs si on ne m'avait pas volé mon sac.

Finalement, je tiens à remercier ma famille pour m'avoir supporté pendant les moments de rédaction et de m'avoir soutenue toutes ses années d'étude et plus particulièrement mon frère pour m'avoir aidé avec le programme et tout simplement pour avoir toujours été là.

Je suis sure que j'en ai oublié alors désolée de vous avoir oublié et merci ^_^

Liste des notations

CIP: Current In Plane
CPP: Current Perpendicular to Plane
GMR: Giant MagnetoResistance
LLG: Landau Lifshitz Gilbert
PMA: Perpendicular Magnetic Anisotropy
STT: Spin Transfer Torque
α: damping constant
γ_0: gyromagnetic ratio
$\mathbf{\Gamma}$: torque
μ_0: vacuum permeability
μ_B: Bohr magneton
A: parameter characterizing the link between charge and spin-angular momentum
A_{ex}: exchange constant
e: charge of the electron
$\hbar$: reduced Planck constant ($\hbar = h/2\pi$)
k: anisotropy constant
$k1$, $k2$: anisotropy constant of the first, second order
M_S: spontaneous magnetization
$\mathbf{H_{ani}}$: anisotropy field
$\mathbf{H_{demag}}$: demagnetization field
$\mathbf{H_{eff}}$: effective field
$\mathbf{H_{ext}}$: external field
N_D: demagnetization tensor
$\mathbf{M}$: magnetization
M_S: spontaneous magnetization
m_e: mass of the electron
$\mathfrak{m}$: magnetic moment
$\mathbf{m}$: unit vector of the magnetization
$\mathbf{p}$: unit vector of the polarizer magnetization
t: thickness
T: temperature
V: volume

Introduction

La découverte en 1988 de la magnétorésistance géante par Albert Fert[1] et Peter Grünberg[2] a été récompensée par un prix Nobel en 2007. Elle a depuis permis d'ouvrir un nouveau domaine de la physique : la spintronique. Jusque là, seule la charge de l'électron était prise en compte dans les dispositifs électroniques ce qui changea lorsque l'on réalisa que l'on pouvait aussi utiliser son moment cinétique de spin. En effet, la capacité de manipuler le spin de l'électron ouvre la voie à de nombreuses applications. À partir de nanostructures telles que les vannes de spin ou les jonctions tunnel, on a pu construire des éléments pour les têtes de disques durs,[3,4] permettant ainsi d'augmenter la densité de stockage. Une autre application très prometteuse est la MRAM[5] (Magnetoresistive Random Access Memory) qui combine les avantages de la mémoire vive et des disques durs, c'est-à-dire vitesse et non volatilité.

En 1996, John Slonczewski[6] et Luc Berger[7] prédirent le phénomène de transfert de spin. Celui-ci décrit l'effet d'un courant polarisé en spin sur l'aimantation d'une nanostructure. En effet, une partie du moment cinétique de spin des électrons peut être transférée à l'aimantation, ceci générant un couple : le couple de transfert de spin. Depuis ces prédictions, ce sujet de recherche a suscité un grand intérêt et de nombreux résultats comme le renversement d'aimantation,[8] la précession d'aimantation,[9,10] ainsi que la propagation de parois de domaines magnétiques induites par un courant polarisé en spin.[11] Ceux-ci devraient donner naissance à de nouvelles applications et améliorer les appareils actuels.[12] Le renversement d'aimantation par un courant polarisé en spin pourrait grandement améliorer les MRAMs, tandis que la précession par courant polarisé en spin pourrait ouvrir la voie vers des oscillateurs hautes fréquences.[13,14] La propagation de paroi de domaines magnétiques par courant polarisé en spin, quant à elle, est le coeur du projet sur les mémoires *racetrack* développé par Stuart Parkin.[15]

Une limitation importante dans la technologie de l'information est la durée de vie. Les disques durs, par exemple, sont conçus pour fonctionner correctement pendant dix ans. Cette limite est due à un phénomène appelé superparamagnétisme,[16] qui décrit le temps nécessaire à un grain magnétique pour que son aimantation se renverse sous l'effet de l'agitation thermique. Ce temps caractéristique est nommé temps de relaxation de Néel. Il est fonction du rapport entre la barrière d'énergie séparant les deux configurations d'aimantation (up et down) et la température. La barrière d'énergie est donnée par la constante d'anisotropie et le volume du grain, ce dernier représentant un bit d'information. Il est ainsi très important d'étudier la dynamique d'aimantation à température finie. Jonathan Sun proposa un modèle[17] décrivant le renversement d'aimantation en tenant compte la température, et de nombreux résultats expérimentaux ont déjà été obtenus.[18,19]

Bien que le domaine de la spintronique soit en plein essor, le phénomène de transfert de spin n'est toujours pas entièrement compris. De plus, nous avons besoin de renversements rapides d'aimantation, ce qui nécessite une bonne compréhension de la dynamique d'aimantation. Dans cette optique, nous avons développé un programme simulant cette dernière dans une structure de vanne de spin. Nous nous sommes concentrés sur des matériaux avec une anisotropie perpendiculaire au plan, plus efficaces. Les premiers résultats sur ces types de vannes de spin furent obtenus en 2006[20,21] et une partie de cette thèse consiste à les comparer à nos simulations. De cette manière, nous avons pu vérifier la solidité de notre modèle et de ses hypothèses.

Ce manuscrit est divisé en quatre parties. La première partie présente l'état de l'art de la dynamique d'aimantation, comprenant les interactions magnétiques fondamentales, la magnétorésistance géante et l'effet de transfert de spin. La deuxième partie décrit le programme de simulation développé au cours de cette thèse. La troisième partie présente les diagrammes d'états calculés. Ces derniers permettent de cartographier les états possibles de configurations de la nanostructure en fonction du courant injecté et du champ magnétique appliqué. Une comparaison avec un diagramme d'état expérimental permet de comprendre l'influence des différents paramètres sur la dynamique d'aimantation. La quatrième et dernière partie est consacrée à la dynamique rapide d'aimantation, c'est-à-dire à l'échelle subnanoseconde. En effet, nous avons étudié l'influence des pulses de courant de très courte durée sur la dynamique d'aimantation. Le code source du programme est fourni en annexe.

Introduction (English)

The discovery of the giant magnetoresistance in 1988 by Albert Fert[1] and Peter Grünberg,[2] for which a Nobel prize was awarded in 2007, has opened a new domain of research: spintronics. Until then, only the charge of the electron was used in electronic devices. That changed when it was realized that the spin momentum could also come into play. Indeed, the ability to manipulate the spin of the electron is found to generate many applications. Nanostructures such as spin valves or tunnel junctions were then integrated into hard disk heads,[3,4] increasing information storage density. Another promising application is the magnetoresistive random access memory (MRAM),[5] it combines the advantages of random access memory and hard disks, that is to say speed and non-volatility.

In 1996, John Slonczewski[6] and Luc Berger[7] predicted the spin transfer effect. It describes the effect of a polarized spin current on a nanostructure layer. A part of the spin momentum of the current electrons can be transfered to the magnetization, generating a torque: the spin transfer torque. Since those predictions, this research topic has generated a lot of interest and many results such as current induced magnetization switching,[8] precession[9,10] or domain wall motion[11] among others, which could generate some applications and improve current devices.[12] Current induced switching may greatly improve MRAMs, whereas current induced precession may lead the way to current-tunable high-frequency oscillators.[13,14] Current induced domain wall motion is the core of the racetrack memories project developed by Stuart Parkin.[15]

An important limitation in information storage technology is the lifespan, which usually is of ten years for hard disk drives. This limit is due to a phenomenon called superparamagnetism,[16] which describes the time for a magnetic grain to change its magnetization under thermal activation, called the Néel relaxation time. It is function of the ratio between the energy barrier between both magnetization configurations (up and down) and the temperature. The energy barrier is given by the anisotropy constant and the volume of the grain, the latter representing a bit of information. It is therefore very important to study finite temperature magnetization dynamics. Jonathan Sun proposed a model[17] describing magnetization switching taking into account the temperature, and many experimental results followed.[18,19]

Although a lot of research has been done in spintronics, the phenomenon of spin transfer torque is not fully understood. Moreover, since fast magnetization switching is needed, understanding magnetization dynamics is of prime importance. In order to get a better comprehension, we developed a software simulating the magnetization dynamics in a spin valve structure. We mainly concentrated on spin valves with a material showing strong perpendicular anisotropy. The first results on those types of spin valves were obtained in 2006[20, 21] and part of this thesis was to compare them with our simulations. This way, we were able to verify our model and its hypotheses veracity.

This thesis is divided in four parts. The first part presents the state of the art of magnetization dynamics, consisting of the fundamental magnetic interactions, the giant magnetoresistance and the spin transfer effect. The second part describes the simulation software developed during this thesis. The third part presents the calculated state diagram, which permits to map the possible magnetic configurations of the nanostructure as a function of the injected current and the applied magnetic field. A comparison of the calculated state diagram with the experimental one allows us to understand the influence of several parameters on the magnetization dynamics. The fourth part focuses on fast dynamics, i.e. at the subnanosecond time scale. Indeed, we studied the influence of the injection of short current pulses on magnetization dynamics. The software source code can be found in the appendix.

Première partie

État de l'art

Résumé

Cette première partie présente l'état de l'art de la dynamique de l'aimantation et les effets de transfert de spin. Nous présentons tout d'abord l'origine du moment magnétique et, dans un deuxième temps, les interactions fondamentales qui sont à l'origine du ferromagnétisme et des configurations magnétiques. Ensuite, nous décrivons la dynamique de l'aimantation, puis le phénomène de magnétorésistance géante, le transfert de spin et finalement le modèle décrit par Jonathan Sun en 2000.

L'aimantation dans un solide résulte du mouvement des électrons. Dans une description quantique, nous pouvons distinguer la contribution provenant du moment cinétique de spin et celle du moment cinétique orbital.

En revanche, l'orientation des moments est régie par différentes interactions magnétiques.
L'interaction Zeeman correspond à l'interaction d'un champ magnétique sur un moment magnétique. Pour minimiser l'énergie Zeeman, les moments magnétiques et donc l'aimantation auront tendance à s'aligner avec le champ appliqué.
L'interaction d'échange est une interaction à courte portée, elle n'est en effet ressentie qu'entre moments magnétiques proches voisins. Cette interaction va tendre à orienter les moments magnétiques soit parallèlement, nous serons alors en présence d'un ordre ferromagnétique, soit antiparallèles, on parlera d'antiferromagnétisme. Dans le premier cas, les moments auront tendance à s'aligner ce qui donnera une aimantation uniforme. Si le matériau possède un arrangement antiferromagnétique de ses moments, l'aimantation est alors nulle. Les phénomènes d'ordre ferromagnétique et antiferromagnétique disparaissent lorsqu'on atteint une température critique. On parlera de température de Curie pour le ferromagnétisme et de température de Néel pour l'antiferromagnétisme.
Chaque moment magnétique à l'intérieur d'un objet magnétique crée un champ nommé champ dipolaire. Ce champ interagit avec les moments magnétiques environnants, c'est ce phénomène que l'on appellera interaction dipolaire. Lorsque l'on considèrera un système constitué de plusieurs couches magnétiques, on nommera champ démagnétisant le champ dipolaire créé par les moments magnétiques d'une couche mince sur elle-même tandis que lorsque l'on parlera de champ dipolaire, on entendra implicitement qu'il s'agit du champ dipolaire d'une couche magnétique sur une autre.
La dernière interaction présentée est l'anisotropie magnétocristalline. Elle provient du couplage spin-orbite et de l'interaction du moment orbital avec le champ cristallin. Dû à cette interaction, l'aimantation va tendre à s'aligner suivant certaines directions privilégiées du cristal. On présentera le cas de l'anisotropie

magnétocristalline uniaxiale qui peut s'exprimer simplement.
Ces interactions sont bien entendu en compétition, particulièrement l'interaction d'échange, très locale, et le champ démagnétisant, qui a un effet à plus grande distance. C'est ainsi que l'on peut définir une longueur caractéristique, la longueur d'échange en dessous de laquelle l'interaction d'échange est prédominante. Si l'objet magnétique a une taille inférieure à cette longueur, l'aimantation restera uniforme. Dans le cas contraire, des domaines peuvent se former. Ainsi cette compétition est à l'origine de la formation de domaines. À l'interface entre ces domaines se forment des parois de domaines magnétiques dont la taille résulte de la compétition entre l'interaction d'échange et l'anisotropie magnétocristalline.
Le modèle de Stoner et Wohlfarth permet de décrire le retournement de l'aimantation d'un objet suffisamment petit pour qu'il puisse être considéré comme un macro-spin. On considère alors une anisotropie uniaxiale et l'effet d'un champ appliqué à température nulle. Ce modèle permet de définir et décrire ce qu'est un cycle d'hystérésis. En collectant les cycles d'hystérésis pour différentes orientations de champs appliqués, il est possible de construire ce qu'on appelle l'astroïde de Stoner-Wohlfarth.
Concernant la dynamique d'aimantation, elle peut être obtenue à l'aide de l'équation de Landau Lifshitz Gilbert (LLG), qui est une équation différentielle qui permet d'écrire la variation d'aimantation en fonction du temps comme la somme des couples agissant sur l'aimantation. Elle est composée de deux termes, le premier entraînant la précession de l'aimantation autour du champ magnétique effectif, le deuxième terme introduit de manière phénoménologique, décrivant l'amortissement qui tend à aligner l'aimantation avec le champ effectif. Chacune des interactions décrites ci-dessus peut être assimilée à un champ magnétique et la somme de ces champs forme le champ effectif.

Le phénomène de magnétorésistance géante (ou GMR) est observé dans des structures de taille nanométrique appelées vannes de spin. Ces dernières sont des multicouches composées de deux couches magnétiques séparées par une couche non magnétique mais conductrice comme le cuivre. Les couches magnétiques sont appelées libre ou dure selon le champ nécessaire pour renverser l'aimantation de la couche. Un important champ magnétique est nécessaire pour renverser la couche dure, de telle manière que l'on peut considérer que son aimantation reste fixe dans la gamme de champs utilisée ici. Les vannes de spin peuvent comprendre des couches dont l'aimantation est dans le plan ou au contraire perpendiculaire au plan, les deux aimantations sont dans la même direction dans le cas général. Ainsi nous pouvons observer deux états pour les vannes de spin, selon que les aimantations des couches libre et dure soient parallèles ou antiparallèles.
La magnétorésistance géante permet de déterminer expérimentalement la configuration des vannes de spin. En effet, nous allons observer des résistances différentes selon l'état de la vanne de spin. En général, lorsque les aimantations des deux couches sont parallèles, nous observons une résistance faible, alors que la résistance sera plus importante en cas de configuration antiparallèle.
Ce phénomène peut être expliqué de façon simple à l'aide du modèle à deux courants, qui établit que les électrons se déplacent avec des conductivités différentes selon leur état de spin, de telle manière que l'on peut considérer qu'ils se déplacent dans deux canaux de conduction indépendants l'un de l'autre. C'est

cette différence de conductivité qui est à l'origine de la différence de résistance entre les différents états parallèles et antiparallèles. En général, la configuration parallèle favorise ainsi la conduction des électrons par rapport à la configuration antiparallèle ce qui explique la différence de résistance entre les deux états.
Ce modèle simple peut être amélioré en tenant compte des effets d'interface entre le ferromagnétique et la couche non magnétique. Comme cela a déjà été décrit, l'aimantation est nulle dans la couche non magnétique, ce qui n'est pas le cas dans les autres couches qui présentent aussi une dissymétrie des populations de spin. Ainsi, une des populations de spin traversera beaucoup plus facilement l'interface que l'autre. Or dans la couche non magnétique, il faut absolument que les deux populations soient égales, ce qui conduit à une accumulation des spins près de l'interface, jusqu'à une longueur caractéristique qui est la longueur de diffusion du spin, c'est-à-dire la longueur pour laquelle le spin conserve son orientation. Ce phénomène est appelé tout simplement le phénomène d'accumulation.
Bien que ces structures ne soient pas étudiées dans cette thèse, il est intéressant de noter qu'il existe aussi le phénomène de magnétorésistance tunnel, qui provient de l'effet tunnel en mécanique quantique. Il est observé dans des structures appelées jonctions tunnel, qui elles, sont composées de deux couches magnétiques séparées par un isolant.

Le transfert de spin est un phénomène complémentaire à la magnétorésistance géante. Dans ce cas, une vanne de spin est traversée par un courant polarisé en spin. Schématiquement, les spins du courant vont s'aligner avec l'aimantation de la couche dure, puis se déplacent dans la couche non magnétique, et enfin arrivent au niveau de la couche libre, où ils vont exercer un couple sur l'aimantation, afin de l'aligner avec l'aimantation de la première couche. La couche dure est aussi parfois appelée polariseur, et la deuxième analyseur par analogie avec l'optique.
L'orgine du transfert de spin peut être comprise facilement à l'aide de la mécanique quantique en étudiant les courants de spin et leur comportement aux interfaces. Différent modèles furent développés pour décrire le couple de transfert de spin, le plus utilisé étant celui de Slonczewski dont l'expression est :

$$\mathbf{\Gamma_{ST}} = \frac{\beta I g(\vartheta)}{\gamma_0} \mathbf{m} \times (\mathbf{m} \times \mathbf{p})$$

où γ_0 est le facteur gyromagnétique, β une constante dépendante des paramètres de la vanne de spin, I le courant, $g(\vartheta)$ une fonction dépendante de l'angle entre les aimantations $\mathbf{m}$ et $\mathbf{p}$ des couches libre et dure respectivement.
Ce couple peut être alors ajouté à l'équation de Landau Lifshitz Gilbert décrite précédemment. Le terme de transfert de spin est dans la même direction que l'amortissement. Il est dépendant du courant, d'après son expression, ce qui signifie que selon le signe du courant, le transfert de spin alignera l'aimantation avec le champ ou au contraire renversera l'aimantation, et sera donc opposée au champ. Un dernier cas est possible si le transfert de spin compense exactement l'amortissement, dans ce cas l'aimantation sera en état de précession. Il est donc ainsi possible de changer l'état d'une vanne du spin avec seulement un courant polarisé en spin.

La température n'a jusqu'alors pas été prise en compte. Elle joue cependant un rôle prépondérant dans les dynamiques d'aimantation. C'est pour cela qu'un champ, donné par une distribution gaussienne, a été ajouté à l'équation LLG. Il est alors possible de définir un temps d'activation thermique obéissant à la statistique de Boltzmann. Ce développement a tout d'abord été réalisé sans transfert de spin, mais il a été montré que l'on pouvait obtenir des résultats équivalents en redéfinissant la température d'activation.

Après intégration pour de petits angles, nous pouvons redéfinir le temps de renversement en fonction du moment angulaire et du courant. C'est grâce à cette grandeur qu'il est possible d'étudier la dynamique d'aimantation à des échelles de temps de l'ordre de la nanoseconde, ce qui sera la pierre angulaire de la dernière partie de cette thèse.

Chapitre 1

Dynamique de l'aimantation

This manuscript mainly focuses on magnetization reversal in magnetic nano-objects induced by a polarized current. The goal of this chapter is to summarize the important notions needed in the following: the origin of magnetism, the different interactions affecting the magnetic configuration inside a nano-object and finally how magnetization dynamics is described by the Landau Lifshitz Gilbert equation. A more detailed description of magnetization dynamics can be found in [22].

1.1 Origin of Magnetism

In 1913, Niels Bohr described the atom as electrons moving around a positive nucleus following a circular orbit. The period of the electron T is given by $T = 2\pi r/v$ where r is the radius and v the velocity of the electron. The motion will create a current $I = q/T$ where q is the charge of the electrons. The orbital magnetic moment is the product of the the current and the surface such as $\boldsymbol{\mathfrak{m}}_{\boldsymbol{\mathfrak{o}}} = IS\mathbf{n}$ where $\mathbf{n}$ is a unit vector perpendicular to the surface S. In the simple case of one electron of charge e circling around the nucleus, we have:

$$\boldsymbol{\mathfrak{m}}_{\boldsymbol{\mathfrak{o}}} = -\frac{e}{2}\mathbf{r} \times \mathbf{v} = -\frac{e}{2m_e}\boldsymbol{\mathfrak{L}}_{\boldsymbol{\mathfrak{o}}} = \gamma \boldsymbol{\mathfrak{L}}_{\boldsymbol{\mathfrak{o}}} \tag{1.1}$$

where $\boldsymbol{\mathfrak{L}}_{\boldsymbol{\mathfrak{o}}}$ is the angular momentum, m_e the mass of the electron and γ the gyromagnetic ratio.

The orbital angular momentum operator in quantum mechanics is quantized along the quantization axis z such as $\mathfrak{l}_z \left|\psi\right\rangle = \hbar m_l \left|\psi\right\rangle$ with $\hbar$ the reduced Planck constant and m_l an integer.

Therefore, the projection of its orbital magnetic moment along this axis is also quantized and

$$\mathfrak{m}_{oz} = -\frac{\hbar e}{2m_e} m_l = -\mu_B m_l \tag{1.2}$$

μ_B is called the Bohr magneton.

As demonstrated by Stern and Gerlach in 1922, we also have to take into account an intrinsic momentum: the spin, whose quantized projections along z are $\pm\frac{1}{2}$. Using the same reasoning we did for the magnetic momentum, the projection of the spin momentum along z becomes:

$$\mathfrak{m}_{sz} = -g_S \mu_B m_S \tag{1.3}$$

where $g_S \simeq 2$ is the Landé g-factor for the spin momentum and m_S an integer. Both the spin moment and the orbital moment will contribute to the total magnetic moment. The Hund rules permit to determine the total magnetic moment held by one atom. This model is accurate for rare earth elements where magnetism is due to the localized 4f electrons. However, for transition metals 3d delocalized electrons, the magnetic moment is given by the spin contribution only.

1.2 Magnetic Interactions

The sum of the different magnetic moments in a material results in its magnetization. The magnetization dynamics is ruled by the competition between the different interactions we will describe in this section.

1.2.1 Zeeman Interaction

When a magnetic moment $\mathfrak{m}$ lies in an applied magnetic field $\mathbf{H}$, it gets an energy $-\mu_0 \mathfrak{m} \cdot \mathbf{H}$ with μ_0 the vacuum permeability. For a ferromagnet with a volume V and the magnetization $\mathbf{M} = \sum_i \mathfrak{m}_i / V$, we can define a Zeeman energy:

$$E_{Zeeman} = -\mu_0 \iiint_V \mathbf{M} \cdot \mathbf{H} dV \tag{1.4}$$

In the case of a uniform magnetization, the Zeeman energy becomes

$$E_{Zeeman} = -\mu_0 \mathbf{M} \cdot \mathbf{H} V \tag{1.5}$$

From equation (1.4), one can see that the Zeeman energy is minimized when the external field and the magnetic moment are aligned.

1.2.2 Exchange Interaction

The exchange energy, whose origin is found in quantum mechanics, describes the reciprocal action between two magnetic moments $\mathfrak{m}_1$ and $\mathfrak{m}_2$ and its expression is given by:

$$E_{ex} = -\mu_0 A_{ex} \mathfrak{m}_1 \cdot \mathfrak{m}_2 \tag{1.6}$$

with A_{ex} the exchange constant.
The exchange is a short distance interaction in a crystal taking into account first neighbor interatoms, which is a very good approximation. In the case of a positive exchange constant, it will favor a configuration where the two moments are parallell, which will incite a uniform magnetization on a larger scale (see Figure 1.1(a)), although this interaction is negligible between two distant moments. The materials whose exchange constant is positive are called ferromagnetic, such as iron, cobalt or nickel. However, if A_{ex} is negative, an antiparallell configuration will be favored. As the magnetic moments will compensate themselves on a localized scale, there will be no magnetization observed macroscopically,

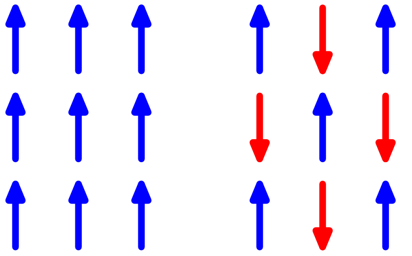

(a) ferromagnetic order (b) antiferromagnetic order

Figure 1.1: Schematic representation of the magnetic moments found in ferromagnetic and antiferromagntic orders

defining antiferromagnetism (see Figure 1.1(b)). Chromium is, for example, antiferromagnetic.

The ordering of magnetic moments is, of course, influenced by temperature. If we heat the material, some magnetic moments will change their orientation due to thermal activation. Once the critical temperature, called respectively Curie or Néel temperature for ferromagnetic or antiferromagnetic materials, is reached, the exchange interaction has no influence, the ferromagnetic or antiferromagnetic order disappears.

1.2.3 Magnetocrystalline Anisotropy

The magnetocrystalline anisotropy is both due to the spin orbit coupling and the crystal field interaction, it renders the fact there are privileged directions for the magnetization. Those directions of course depend on the crystallographic structure of the material.

The magnetocrystalline anisotropy takes different forms, depending on the crystal symmetry. In the case of uniaxial symmetry, the density of magnetocrystalline anisotropy energy is given by:

$$\frac{E_{ani}}{V} = k_1 \sin^2 \vartheta + k_2 \sin^4 \vartheta + \dots \tag{1.7}$$

with k_1, k_2... the anistropy constants, and ϑ the angle between the magnetization and easy the anistropy axis. The latter is the axis along the privileged magnetization direction, while the hard axis is perpendicular to it.

As an illustration, the magnetocrystalline anisotropy energy for a cubic crystal is shown on Figure 1.2. It may be noted that, for most cases, the first term is sufficient to describe correctly the anisotropy.

1.2.4 Dipolar Interaction

The dipolar interaction corresponds to the field produced by a magnetic moment or a magnetization. It will thus affect other neighbor magnetic moments. The

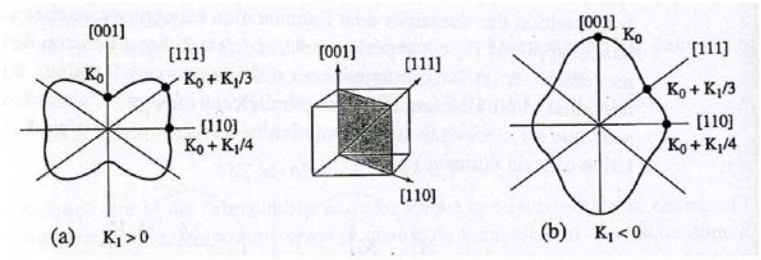

Figure 1.2: Cubic crystal: the energy is represented as a function of the magnetization direction in the plane (perpendicular to an axis with binary symmetry). This plane contains the three major symmetry axes. As the anisotropy is defined except to a constant term, k_0 is added to the anisotropy in order to facilitate the graphic presentation. Figure extracted from [22]

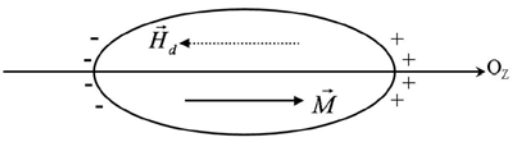

Figure 1.3: Ellipsoid uniformly magnetized along the z axis. $\mathbf{H}_{\text{dem}}$ is the demagnetizing field due to the existence of magnetic poles at the surface of the ellipsoid. Figure extracted from [23]

dipolar field created by a magnetic moment $\mathfrak{m}$ at a distance r is given by:

$$\mathbf{H}_{\text{dip}} = \frac{1}{4\pi}\left(\frac{(\mathfrak{m}\cdot\mathbf{r})\mathbf{r}}{r^5} - \frac{\mathfrak{m}}{r^3}\right) \tag{1.8}$$

The dipolar interaction is a long range interaction.
If we consider the dipolar field of a magnetization produces on itself, it will be given by:

$$\mathbf{H}_{\text{dem}} = -\hat{N}\cdot\mathfrak{m} \tag{1.9}$$

where $\hat{N}$ is the demagnetization tensor, represented by a 3x3 matrix, whose values are only dependent on the shape of the sample. In the case of a spherical one, the matrix becomes diagonal and its factors are $N_{xx} = N_{yy} = N_{zz} = 1/3$. It becomes for thin films with the surface in the x-y plane: $N_{xx} = N_{yy} = 0$ and $N_{zz} = 1$.
The energy density, in the specific case of a thin film is given by:

$$E_{\text{dem}} = -\frac{1}{2}\mu_0 M^2 \sin^2\vartheta V \tag{1.10}$$

with ϑ the angle between the sample surface and the magnetization (see Figure 1.3).
This energy is a uniaxial anistropy. Since it depends on the shape of the sample, it is often called shape anisotropy.

1.3 Competition between Interactions

The magnetic configuration is determined by the minimization of the energy composed of the different interactions previously described:

$$E = E_{\text{ani}} + E_{\text{ex}} + E_{\text{dip}} + E_{\text{Zeeman}} \tag{1.11}$$

The different interactions present in the system will tend to align the magnetization in different directions. They show different interaction lengths. The exchange interaction decreases rapidly whereas the dipolar interaction has a longer range.
Therefore on can define the exchange length l_{ex}, which determines a typical length for which exchange is dominant over the dipolar interaction.

$$l_{ex} = \sqrt{\frac{A_{ex}}{\mu_0 M_S^2}} \tag{1.12}$$

Consequently, the magnetization tends to be uniform when the sample size is smaller than the exchange length, it may then be considered as a macrospin. If it exceeds l_{ex}, domains appear. The latter are separated by domain walls, with the magnetization rotating within. Their width and energy are specific to the considered material.

1.3.1 Stoner-Wohlfarth Model

The Stoner-Wohlfarth model[24] was introduced in 1948. It determines the possible magnetization configurations, considering two hypotheses: the ferromagnet magnetization is described as a macrospin and thermal activation is not taken into account The external field **H** makes an angle φ with the z direction, while ϑ is the angle between the magnetization and the easy anisotropy axis which is also along the z direction (see Figure 1.4) and whose anisotropy constant is k. We can thus define the energy density as:

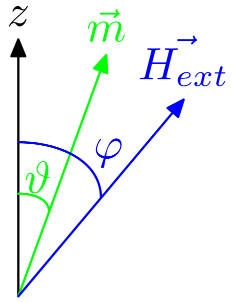

Figure 1.4: Definition of the angles. The easy anisotropy is along z. ϑ represents the angle between the z axis and the magnetization **m**. φ is the angle between the external field and the z axis.

$$\varepsilon = k\cos^2\vartheta - \mu_0 M_S H \cos(\varphi - \vartheta) \tag{1.13}$$

with M_S the spontaneous magnetization.
We need to differentiate equation (1.13) to obtain the equilibrium positions

$$\frac{\partial \varepsilon}{\partial \vartheta} = 2k \sin\vartheta \cos\vartheta + \mu_0 M_S H \sin(\varphi - \vartheta) = 0 \tag{1.14}$$

Another derivation gives us the stable and unstable positions:

$$\frac{\partial^2 \varepsilon}{\partial \vartheta^2} = 2k(\cos^2\vartheta - \sin^2\vartheta) + \mu_0 M_S H \cos(\varphi - \vartheta) = 0 \tag{1.15}$$

From those equations, in the case where the applied field is aligned with the easy axis, one can determine the hysteresis loop. Indeed, equation (1.14) has a solution for $\sin\vartheta = 0$, i.e. $\vartheta = 0$ or $\vartheta = \pi$, it corresponds to the positions aligned with the easy anisotropy axis, they are the maximum and minimum of energy. The other solution is $\cos\vartheta = -\frac{\mu_0 M_S}{2k} H$, which corresponds to an energy maximum between the two minima for $\vartheta = 0$ and $\vartheta = \pi$. Equation (1.15) gives the position where the energy barrier disappears, which is $H = \pm H_k = \pm \frac{2k}{\mu_0 M_S}$. These two fields correspond to the applied fields needed to reverse the magnetization (H_k for the $\pi \to 0$ transition and $-H_k$ for $0 \to \pi$). This reversal process is called hysteretic and is represented on Figure 1.5(a).

In the case of an applied field perpendicular to the easy anisotropy axis, one of the solutions of the equation (1.14) is $\cos\vartheta = 0$, hence $\vartheta = \pi/2$ or $\vartheta = -\pi/2$. The energy extrema lie along the hard anisotropy axis here. The other solution is $\sin\vartheta = -H/H_k$. If $H > H_k$, the magnetization is saturated and along the applied field. Otherwise, the magnetization is given by: $M = M_S \frac{H}{H_k}$.The loop for $\varphi = \pi/2$ is plotted on Figure 1.5(b).

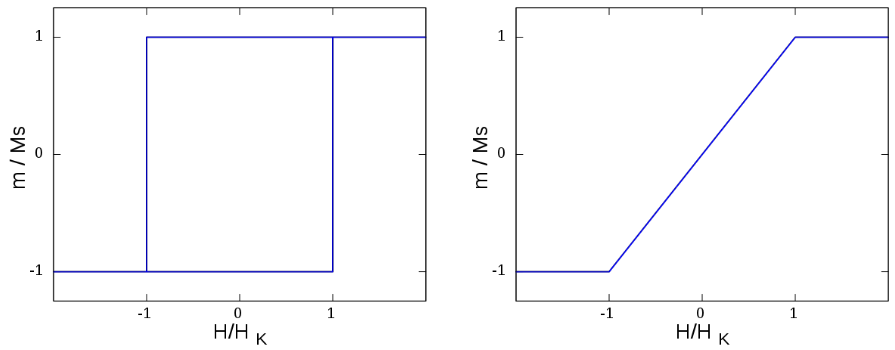

(a) The applied field is along the easy anisotropy axis. $\varphi = 0$

(b) The applied field is perpendicular to the easy anisotropy axis. $\varphi = \pi/2$

Figure 1.5: Hysteresis loops for two different system configurations

Using the substitutions $H_z = H\cos\vartheta$ and $H_y = H\sin\vartheta$, we can solve equations (1.14) and (1.15)

$$\begin{cases} H_y = -H_k \sin^3\vartheta \\ H_z = H_k \cos^3\vartheta \end{cases} \tag{1.16}$$

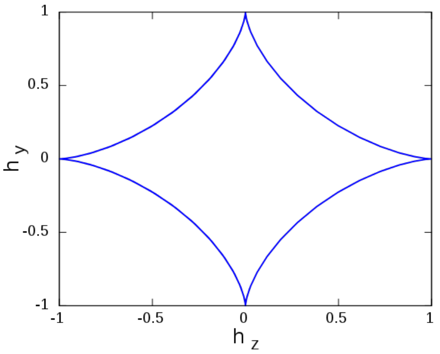

Figure 1.6: Stoner Wohlfarth astroid. h_y and h_z are the reduced fields given by $h_y = H_y/H_k$ and $h_z = H_z/H_k$

We can then plot equation (1.16) to obtain the Stoner-Wohlfarth astroid on Figure 1.6.

The astroid shows the value of the reversal field for different angles of the applied field. It is a collection of the hysteresis loops obtained while varying the angle between the applied field and the easy anisotropy axis.

1.4 Landau-Lifshitz-Gilbert Equation

Although the Stoner-Wohlfarth model does explain the magnetization reversal between two states, it is not enough to understand magnetization dynamics. However, a much better description is possible with the help of the Landau Lifshitz equation.

If we place a ferromagnet in a uniform magnetic field $\mathbf{H}$, a torque $\mathbf{\Gamma}$ will act on the magnetization $\mathbf{M}$, such as $\mathbf{\Gamma} = \mu_0 \mathbf{M} \times \mathbf{H}$. As the magnetic moment is proportional to the angular momentum, the magnetization obeys:

$$\frac{d\mathbf{m}}{dt} = -\gamma_0 \mathbf{m} \times \mathbf{H} \tag{1.17}$$

where $\mathbf{m}$ is the unit vector of the magnetization given by $\mathbf{m} = \mathbf{M}/M_S$ and the constant γ_0 is the product of the vacuum permeability and the gyromagnetic ratio $\gamma_0 = \gamma\mu_0$.
We can see from equation (1.17) that the magnetization will precess around the field at the frequency $\gamma_0\mathbf{H}$, if the field and magnetization are not aligned.

However, the previously described interactions are also operating on the magnetization. As they can all be expressed as a magnetic field, we can regroup them in an effective field $\mathbf{H_{eff}}$ that will rule the magnetization dynamics as:

$$\frac{d\mathbf{m}}{dt} = -\gamma_0 \mathbf{m} \times \mathbf{H}_{\text{eff}} \tag{1.18}$$

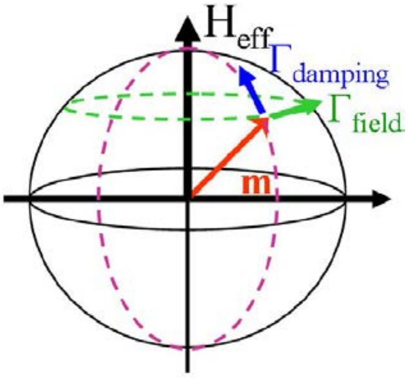

Figure 1.7: Schematic representation of the torques acting on the magnetization

In the case of the effective field $\mathbf{H}_{\text{eff}}$ aligned with the z axis with $\mathbf{H}_{\text{eff}} = H_{\text{eff}}\mathbf{e_z}$, equation (1.18) becomes

$$\begin{cases} \frac{dm_x}{dt} = -\gamma_0 m_y H_{\text{eff}} \\ \frac{dm_y}{dt} = \gamma_0 m_x H_{\text{eff}} \\ \frac{dm_z}{dt} = 0 \end{cases} \tag{1.19}$$

If ϑ is the angle between the magnetization and the effective field, the solution is given by

$$\begin{cases} m_x(t) = \sin\vartheta\cos\left(\gamma_0 t H_{\text{eff}}\right) \\ m_y(t) = \sin\vartheta\sin\left(\gamma_0 t H_{\text{eff}}\right) \\ m_z(t) = \cos\vartheta \end{cases} \tag{1.20}$$

Equation (1.20) gives the trajectory of the magnetization. It corresponds to a precession around the effective field at the frequency $\gamma_0 H_{\text{eff}}$ (see Figure 1.8(a)). The effective field is given by:

$$\mathbf{H}_{\text{eff}} = -\frac{1}{\mu_0 V}\frac{\partial E}{\partial \mathbf{M}} \tag{1.21}$$

with E the total energy of the ferromagnet.
As all the interactions present in the effective field are conservative, there is no dissipation of energy. The magnetization should precess indefinitely. However, the magnetization emits magnons and phonons, thus dissipating energy.
To take the dissipation into account, we introduce a phenomenological damping term $\alpha\frac{d\mathbf{m}}{dt}$ and we find the Landau Lifshitz Gilbert equation[25, 26]:

$$\frac{d\mathbf{m}}{dt} = -\gamma_0 \mathbf{m} \times \mathbf{H}_{\text{eff}} + \alpha \mathbf{m} \times \frac{d\mathbf{m}}{dt} \tag{1.22}$$

We can thus represent the damping as a torque acting on the magnetization, as we can see on Figure 1.7.
If the magnetization is not aligned with the field, there will be damped oscillations until the magnetization and field are aligned.

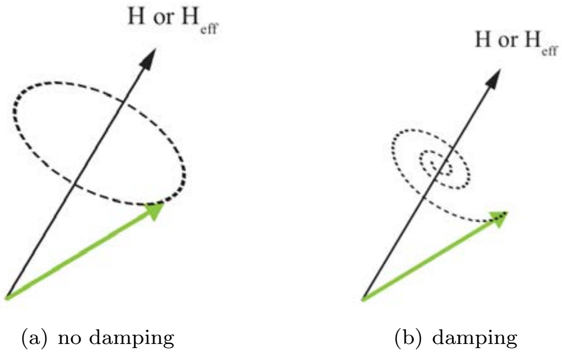

(a) no damping (b) damping

Figure 1.8: Schematic trajectory of the magnetization in the presence of a magnetic field

Chapitre 2

Magnétorésistance géante

The magnetoresistance phenomenon describes the change of resistance of a material when it is subjected to a magnetic field. It was measured for the first time by Lord Kelvin in 1856.[27] There are different types of magnetoresistance, the anisotropic magnetoresistance[28] (AMR), in that case, changes with the angle between the direction current and the magnetization.
We will focus on the giant magnetoresistance in this chapter since this effect permits to probe the relative orientation of the magnetization in the spin valve structure used to study spin torque effect.

2.1 Discovery of the Giant Magnetoresistance

The giant magnetoresistance (GMR) phenomenon was discovered concurrently by Albert Fert[1] and Peter Grünberg[2] in 1988. It was made possible by great advances in deposition techniques, which allowed for the fabrication of nanostructures such as spin valves.
A spin valve is a simple nanostructure composed of two magnetic layers separated by a non magnetic layer called a spacer, usually copper. If the spacer is an insulator, like magnesium oxide, then the structure is called a magnetic tunnel junction. The latter is not described here, as it is not the subject of the study.
It is also important to note those discoveries were done with geometries with the current in plane (CIP), i.e. the current direction is in the plane of the layer, whereas we can also find a configuration with the current direction perpendicular to the plane (CPP). GMR in CPP structures was measured a few years later by Pratt.[29]
Albert Fert worked on [Fe/Cr] superlattices, with the iron films magnetized along the surface direction and coupled antiferromagnetically between them. He found the resistance measured on the multilayer varied considerably with the applied field. Figure 2.1(a) shows the magnetoresistance of a Fe/Cr multilayer, which is reduced to almost half its value for fields greater than two teslas. The GMR was also dependent on the spacer thickness, which can be seen on Figure 2.1(a).

Peter Grünberg measured the magnoresistance of a [Fe/Cr] bilayer (Figure 2.1(b)), and found as well the GMR changed at higher fields and its value is around 1.5%.

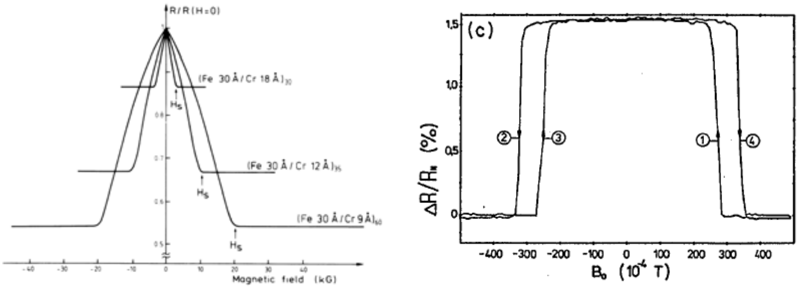

(a) Three [Fe/Cr] superlattices at 4.2 K. Figure extracted from (1)

(b) Fe double layers. Figure from (2)

Figure 2.1: Magnetoresistance of [Fe/Cr] multilayers with antiferromagnetic coupling

2.2 Theory

The considerate change of magnetoresistance with the external field can be explained with the two current model.

2.2.1 Two Current Model

The two current model was introduced by Mott in 1936[30] and refined by Fert and Campbell in 1968.[31] Its main idea is that the spin up and spin down electrons are transported in two channels with different conductivities and little interaction between them.
To understand the model, it is important to differentiate the electron states. The $3d$ electrons are mostly localized, while the s and p ones can propagate easily in the material. Therefore, the conductivity is mainly given by the s and p electrons.
Figure 2.2 shows a schematic band structure of a transition metal, for both spin

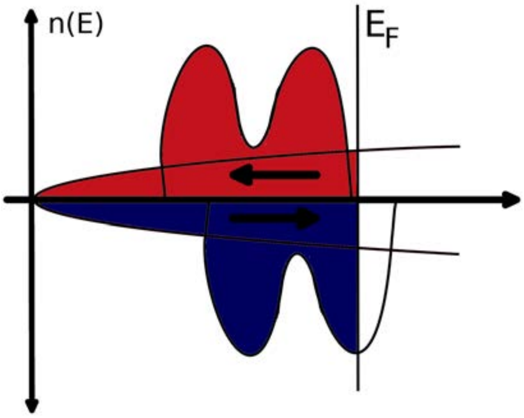

Figure 2.2: Schematic band structure of a $3d$ metal

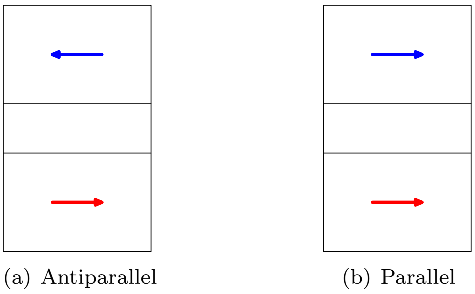
(a) Antiparallel (b) Parallel

Figure 2.3: Possible spin valve configurations

configurations. It is clear there's an asymetry in the density of states between the spins up and down. At the Fermi level, we can see the $3d$ band for the electrons ↑ are more filled than the ↓ ones, it means there are less s electrons of spin up to diffuse to the d band compared to the s electrons of spin down. Thus the conductivity for the channel of spins ↑ will be larger than the spins ↓, which means in terms of resistivity:

$$\rho_{\downarrow} > \rho_{\uparrow} \tag{2.1}$$

2.2.2 Application on spin valves

Let's now consider a spin valve to understand its resistance in the two current model. The current injected in the spin valve will be conducted in two channels, one for spins ↑ and another one for spins ↓. If the spin valve layer magnetization is parallell with the spin direction, its resistance is called r. If it is antiparallell with it, the resistance is R.

The spin valves we describe here can be in two states depending on the layer magnetizations: parallel if both magnetizations are aligned, antiparallel if they are antialigned, as presented on Figure 2.3

Using a circuit analogy(Figure 2.4), we can easily deduce the resistance value in the parallell (P) and antiparallell (AP) cases (equation (2.2)).

$$R_P = \frac{2Rr}{(R+r)} \qquad\qquad R_{AP} = \frac{R+r}{2} \tag{2.2}$$

If $r << R$, then $R_P \approx 2r$ and $R_{AP} \approx R/2$. The giant magnetoresistance is defined as:

$$GMR = \frac{R_{AP} - R_P}{R_P} = \frac{(R-r)^2}{4Rr} \tag{2.3}$$

2.3 Spin Accumulation

Although the giant magnetoresistance phenomenon can be explained easily enough with the two currrent model, it doesn't take into account the effect of a spin polarized current at the interfaces.

The spin accumulation effect is located at the interfaces and describes transport properties.

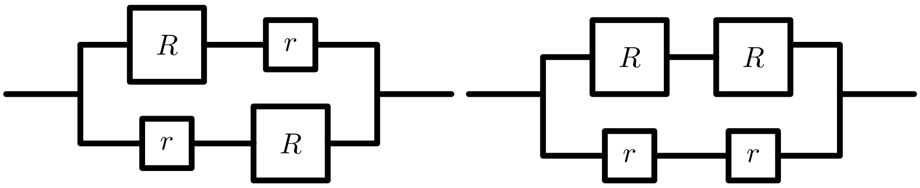

(a) Antiparallell configuration (b) Parallell configuration

Figure 2.4: Equivalent electrical circuits for both spin valve configurations

Let's consider an interface between a ferromagnet and a non magnetic layer. As it was explained in section 2.2.1, there's an asymetry in the spin conduction channels, which means there will be more spins ↑ than spins ↓ crossing the interface. However, the conduction in the non magnetic layer relies equally on the spins up and down. Those two conditions can only be fulfilled if there is an accumulation of spins ↑ near the interface, and also a depletion of the spins ↓. The difference of population between both spins produces a chemical gradient $\Delta\mu$ described in the Valet-Fert model as:

$$\Delta\mu = \mu^{\uparrow} - \mu^{\downarrow} \tag{2.4}$$

where μ is the chemical potential associated with one type of spin population. This phenomenon is limited by the spin diffusion length l_{sd}, which is the distance along which the electron doesn't change its spin. When this length is reached, there is an equilibrium between the spins up and down in the non magnetic layer, whose characteristic lengths respectively are $l^{\uparrow}$ and $l^{\downarrow}$. Its expression is given by:

$$\frac{1}{l_{sd}} = \sqrt{\left(\frac{1}{l^{\uparrow}}\right)^2 + \left(\frac{1}{l^{\downarrow}}\right)^2} \tag{2.5}$$

The spin accumulation effect is represented on Figure 2.5.

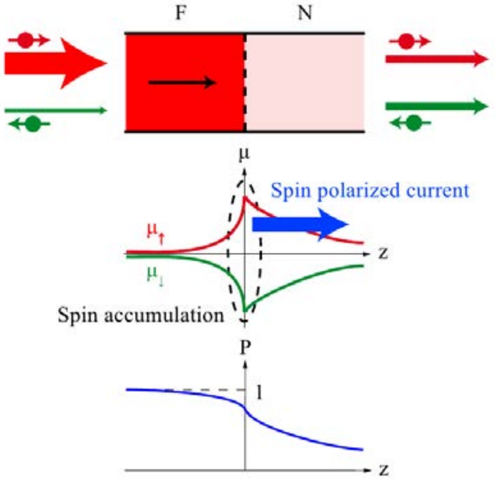

Figure 2.5: Spin accumulation at a NM/FM interface. Figure extracted from [32]

Chapitre 3

Transfert de spin

This chapter will give a general description of the spin transfer effect, before using a quantum approach to explain the spin transfer torque, and then we will present the Slonczewski model, and its integration in the Landau Lifshitz Gilbert equation. Afterwards, we will look at the the effect of spin transfer torque on trajectories and the Stoner Wohlfarth astroid. The last part will describe a powerful tool to study magnetization dynamics: state diagrams.

For a more thorough description of the spin transfer torque, the reader is referred to the reviews by Mark Stiles.[33, 34]

3.1 General Description of the Spin Transfer Effect

Since spin transfer was predicted in 1996 by Luc Berger[7] and John Slonczewski,[6] spintronics has garnered a lot of attention.

Let's consider a spin valve composed of two ferromagnetic layers separated by

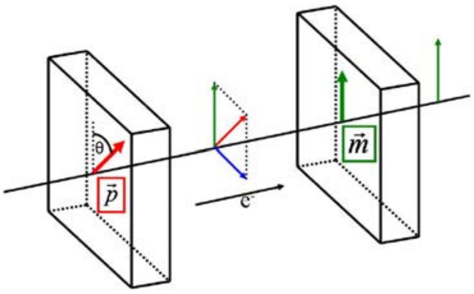

Figure 3.1: Schematic view of the spin transfer phenomenon inside a spin valve. **p** and **m** are the magnetizations of the hard and free layer respectively. The blue arrow represents the transverse component of the free layer magnetization. ϑ is the angle between **p** and **m**.

a spacer. The first layer is called the hard or reference layer, and the second one is the free layer. The former has a magnetization **p** that is considered fixed, whereas the free layer magnetization **m** can move freely (see Figure 3.1). To keep the magnetization in the same position, we can increase the thickness of the layer, or include materials with a larger anisotropy, so that the magnetization stays fixed unless a huge magnetic field is applied on the spin valve.
When a current is injected perpendicularly to the layer surface, the spin of the current electrons will align in the same direction of the hard layer, hence the name of polarizer. As the magnetizations in the two layers are not collinear, there will be an angle between the spins of the current electrons and the free layer magnetization. The spins can be decomposed in a transverse and a parallel direction with **m**. When the current electrons are passing through the free layer, the transverse component of their spin is absorbed, leaving it aligned with the free layer magnetization. However, the total momentum must be conserved, which implies the difference of spin moment leads to a difference of magnetic moment, i.e. the magnetization. This difference results in a torque called the spin transfer torque (STT) given by:

$$\mathbf{\Gamma_{ST}} = \frac{\beta I g(\vartheta)}{\gamma_0}\mathbf{m} \times (\mathbf{m} \times \mathbf{p}) \tag{3.1}$$

where I is the injected current, $g(\vartheta)$ a function of the angle ϑ between both magnetizations, and

$$\beta = \frac{\hbar\gamma_0}{2e\mu_0 M_S V} \tag{3.2}$$

with V the volume of the free layer, M_S its spontaneous magnetization, e the electron charge, $\hbar$ the reduced Planck constant and μ_0 the Bohr magneton.

3.2 Quantum Approach

Spin transfer results from the conservation of the total angular momentum, comprised of the spin moment of the current electrons injected in the spin valve, and the magnetization of the free layer. In the following, we describe this process with a quantum approach, as presented by D. C. Ralph and Mark Stiles.[34]

First, we can define a spin current density **Q** as:

$$\mathbf{Q} = \mathbf{v} \otimes \mathbf{s} \tag{3.3}$$

where **v** is the average electron velocity and **s** the spin density. In the case of a single electron, the spin current density is:

$$\mathbf{Q} = \frac{\hbar^2}{2m_e}\mathrm{Im}(\psi^* \sigma \otimes \nabla\psi) \tag{3.4}$$

where m_e is the mass of the electron, σ are the Pauli matrices, ψ the spin electrons wavefunctions.
Let's consider a single electron with a wave vector **k** in the x direction colliding with a magnetic layer with an angle ϑ with respect to $\mathbf{e_z}$. A sketch of the different vectors and angles can be found on Figure 3.2. The incident part of

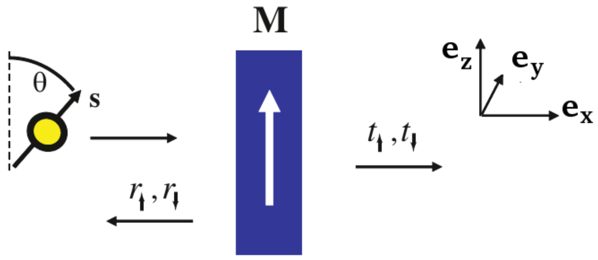

Figure 3.2: Definition of the vectors in the system. Figure extracted from [34]

the wavefunction is:

$$\psi_{inc} = \frac{e^{ikx}}{\sqrt{\Omega}}(\cos(\vartheta/2)\,|\uparrow\rangle + \sin(\vartheta/2)\,|\downarrow\rangle) \tag{3.5}$$

with Ω is a normalization volume.
The transmitted and reflected parts are respectively given by:

$$\psi_{trans} = \frac{e^{ikx}}{\sqrt{\Omega}}(t_\uparrow\cos(\vartheta/2)\,|\uparrow\rangle + t_\downarrow\sin(\vartheta/2)\,|\downarrow\rangle) \tag{3.6}$$

$$\psi_{refl} = \frac{e^{-ikx}}{\sqrt{\Omega}}(r_\uparrow\cos(\vartheta/2)\,|\uparrow\rangle + r_\downarrow\sin(\vartheta/2)\,|\downarrow\rangle) \tag{3.7}$$

Using equation (3.4) to calculate the spin current densities of the three parts of the wave function (3.5), (3.6) and (3.7) we obtain:

$$\mathbf{Q_{in}} = \frac{\hbar^2 k}{2m_e\Omega}[\sin\vartheta\mathbf{e_x} + \cos\theta\mathbf{e_z}] \tag{3.8}$$

$$\begin{aligned}\mathbf{Q_{trans}} &= \frac{\hbar^2 k}{2m_e\Omega}\sin\vartheta\mathrm{Re}(t_\uparrow t_\downarrow^*)\mathbf{e_x} + \frac{\hbar^2 k}{2m_e\Omega}\sin\vartheta\mathrm{Im}(t_\uparrow t_\downarrow^*)\mathbf{e_y}\\ &+ \frac{\hbar^2 k}{2m_e\Omega}[|t_\uparrow|^2\cos^2(\vartheta/2) - |t_\downarrow|^2\sin^2(\vartheta/2)]\mathbf{e_z}\end{aligned} \tag{3.9}$$

$$\begin{aligned}\mathbf{Q_{refl}} &= -\frac{\hbar^2 k}{2m_e\Omega}\sin\vartheta\mathrm{Re}(r_\uparrow r_\downarrow^*)\mathbf{e_x} - \frac{\hbar^2 k}{2m_e\Omega}\sin\vartheta\mathrm{Im}(r_\uparrow r_\downarrow^*)\mathbf{e_y}\\ &- \frac{\hbar^2 k}{2m_e\Omega}[|r_\uparrow|^2\cos^2(\vartheta/2) - |r_\downarrow|^2\sin^2(\vartheta/2)]\mathbf{e_z}\end{aligned} \tag{3.10}$$

If we look at the total spin current, we can see that $\mathbf{Q_{in}} + \mathbf{Q_{refl}} \neq \mathbf{Q_{trans}}$, which means the total spin current is not conserved. Thus, we can calculate the spin transfer torque $\mathbf{\Gamma_{ST}}$ for an area A:

$$\mathbf{\Gamma_{ST}} = A\mathbf{e_x}\cdot(\mathbf{Q_{in}} + \mathbf{Q_{refl}} - \mathbf{Q_{trans}}) \tag{3.11}$$

$$= \frac{A}{\Omega}\frac{\hbar^2 k}{2m_e}\sin\vartheta[1 - \mathrm{Re}(t_\uparrow t_\downarrow^* + r_\uparrow r_\downarrow^*)]\mathbf{e_x} - \frac{A}{\Omega}\frac{\hbar^2 k}{2m}\sin\vartheta\mathrm{Im}(t_\uparrow t_\downarrow^* + r_\uparrow r_\downarrow^*)\mathbf{e_y} \tag{3.12}$$

Looking at equation (3.12), we can see there is no z component for the torque. Furthermore, there are two possibilities to cancel the torque: the first one is for

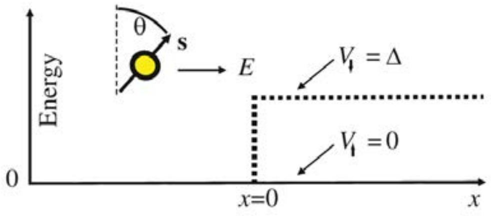

Figure 3.3: Illustration of the energy step. Figure extracted from [34]

$\vartheta = 0$ or $\vartheta = \pi$; the second one is if $t_\uparrow = t_\downarrow$ and $r_\uparrow = r_\downarrow$.
This means that if there is no angle between the spin current and the layer magnetization, no spin torque will rise. The second condition is verified for non magnetic layers.
This simple model indeed shows how spin transfer torques are created. We can now study a more complicated model, which will allow us to obtain the form of the spin transfer torque.
Let's now consider a normal metal/ferromagnet interface, the magnetic layer is described with the Stoner model, which supposes there's an exchange splitting Δ, producing the difference between the minority and majority conductivity bands (see Figure 3.3).
In this model, the different parts of the electron wavefunctions are:

$$\psi_{in} = \frac{e^{ikx}}{\Omega}(\cos\vartheta/2\,|\uparrow\rangle + \sin\vartheta/2\,|\downarrow\rangle) \tag{3.13}$$

$$\psi_{trans} = \frac{e^{ik_\uparrow x}}{\sqrt{\Omega}}\cos(\vartheta/2)\,|\uparrow\rangle + \frac{e^{ik_\downarrow x}}{\sqrt{\Omega}}\frac{2k}{k+k_\downarrow}\sin(\vartheta/2)\,|\downarrow\rangle \tag{3.14}$$

$$\psi_{refl} = \frac{e^{-ikx}}{\sqrt{\Omega}}\frac{k-k_\downarrow}{k+k_\downarrow}\sin(\vartheta/2)\,|\downarrow\rangle \tag{3.15}$$

with $k_\uparrow = k$ and $k_\downarrow = \frac{\sqrt{2m_e(E-\Delta)}}{\hbar} < k$.
In the same way as before, we can calculate the spin current and we get:

$$\mathbf{Q_{in}} = \frac{\hbar^2}{2m_e\Omega}(k\sin\vartheta\mathbf{e_x} + k\cos\vartheta\mathbf{e_z}) \tag{3.16}$$

$$\begin{aligned}\mathbf{Q_{trans}} = {} & \frac{\hbar^2}{2m_e\Omega}\sin\vartheta\frac{2kk_\downarrow}{k+k_\downarrow}\cos[(k_\uparrow - k_\downarrow)x]\mathbf{e_x} + \frac{\hbar^2}{2m_e\Omega}\sin\vartheta\frac{2kk_\downarrow}{k+k_\downarrow}\sin[(k_\uparrow - k_\downarrow)x]\mathbf{e_y} \\ & + \frac{\hbar^2}{2m_e\Omega}k_\downarrow\left[\cos^2(\vartheta/2) - \left(\frac{2k}{k+k_\downarrow}\right)^2\sin^2(\vartheta/2)\right]\mathbf{e_z}\end{aligned} \tag{3.17}$$

$$\mathbf{Q_{refl}} = \frac{\hbar^2}{2m_e\Omega}k\left(\frac{k-k_\downarrow}{k+k_\downarrow}\right)^2\mathbf{e_z} \tag{3.18}$$

If we analyse the spin currents, we can see there's a discontinuity at the interface for the x component. Indeed, the x component of the transmitted spin current is smaller than the incident one, which means there's a partial absorption of the transverse component to the layer magnetization, $\mathbf{e_z}$ in the present case.

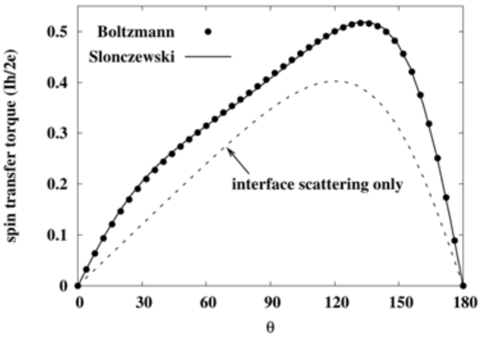

Figure 3.4: Angle dependence of the spin transfer torque derived from Slonczewski and Boltzmann. Figure extracted from [35]

Using the current densities from equations (3.16), (3.17) and (3.18), the spin transfer torque is given by:

$$\mathbf{\Gamma_{ST}} = A\frac{\hbar^2 k}{2m_e\Omega}\sin\vartheta[(1-\cos[(k_\uparrow - k_\downarrow)z])\mathbf{e_x} + \sin[(k_\uparrow - k_\downarrow)z]\mathbf{e_y}] \tag{3.19}$$

3.3 Landau Lifshitz Gilbert Slonczewski Equation

In the previous section, we presented a quantum approach to understand the origin of the spin transfer torque. A model was described by Slonczewski[6] in 1996 from which he obtained the following spin transfer torque:

$$\frac{\mathbf{\Gamma_{ST}}}{M_S} = -\beta I g(\vartheta)\mathbf{m}\times(\mathbf{m}\times\mathbf{p}) \tag{3.20}$$

with

$$\beta = \frac{\hbar\gamma_0}{2\mu_0 M_S V e} \tag{3.21}$$

and

$$g(\vartheta) = \frac{q_+}{A + B\cos\theta} + \frac{q_-}{A - B\cos\vartheta} \tag{3.22}$$

Here, $g(\vartheta)$ is a scalar function representing the angle difference between the layer magnetization $\mathbf{m}$ and the polarized electrons $\mathbf{p}$. Both $\mathbf{m}$ and $\mathbf{p}$ are unit vectors. In the scalar function $g(\vartheta)$, the terms A, B, q_+ and q_- are characteristic of the device geometry and the physical properties of the layers and interfaces. We may note the ratio q_-/q_+ depends on the asymmetry of the structure. B/A describes the asymmetry of the slope of the torque between angles close to parallell and those close to antiparallell.
The ϑ dependence of the spin transfer torque can be calculated using different models, such as the ones derived from Slonczewski or Boltzmann.[35,36] They are plotted on Figure 3.4.

Introducing the spin transfer torque into the LLG, we obtain the Landau

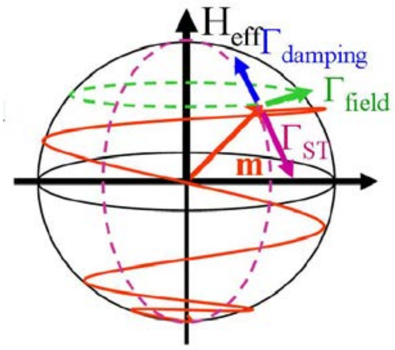

Figure 3.5: Torques exerted on the magnetization under the influence of an effective field and a spin current

	In plane	Out of plane
$H_{\text{eff}}^{P\to AP}$	$H + H_{\text{dip}} + H_{K_{\text{ip}}} + M_S/2$	$H + H_{\text{dip}} + (H_{k_{\text{oop}}} - M_S)$
$H_{\text{eff}}^{AP\to P}$	$-(H + H_{\text{dip}} + H_{K_{\text{ip}}} + M_S/2$	$-(H + H_{\text{dip}}) + (H_{k_{\text{oop}}} - M_S)$
U_k	$\mu_0(M_S V H_{k_{\text{ip}}})/2$	$\mu_0(M_S V (H_{k_{\text{oop}}} - M_S))/2$
$\lvert I_{sw}\rvert$	$\frac{2e}{\hbar}\frac{2\alpha}{g(\vartheta)p}\left(U_k + \frac{1}{2}\mu_0 M_S^2 V\right)$	$\frac{2e}{\hbar}\frac{2\alpha}{g(\vartheta)p}U_k$

Table 3.1: Effective field H_{eff}, energy barrier between two stable magnetic states U_k and switching current I_{sw} for the in plane and out of plane configurations

Lifshitz Gilbert Slonczewski equation (LLGS):

$$\boxed{\frac{d\mathbf{m}}{dt} = -\gamma_0 \mathbf{m} \times \mathbf{H}_{\text{eff}} + \alpha \mathbf{m} \times \frac{d\mathbf{m}}{dt} - \frac{\beta I g(\vartheta)}{\gamma_0} \mathbf{m} \times (\mathbf{m} \times \mathbf{p})} \tag{3.23}$$

As it was already described in section 1.4 page 27, the first term represents the precession around the external field, the second term is the damping and tends to align the magnetization with the field. The last term is aligned parallel or antiparallel to the damping torque. The sign of the spin transfer torque changes with the current. If the spin transfer compensates the damping torque exactly, then the magnetization is in a state of precession.

The switching current, as well as the anisotropy energy for CPP and CIP geometries are gathered in table 3.1. If we look at the switching current expression, we can see it should be easier to reverse the magnetization with a current perpendicular to the plane geometry than with a current in plane geometry.

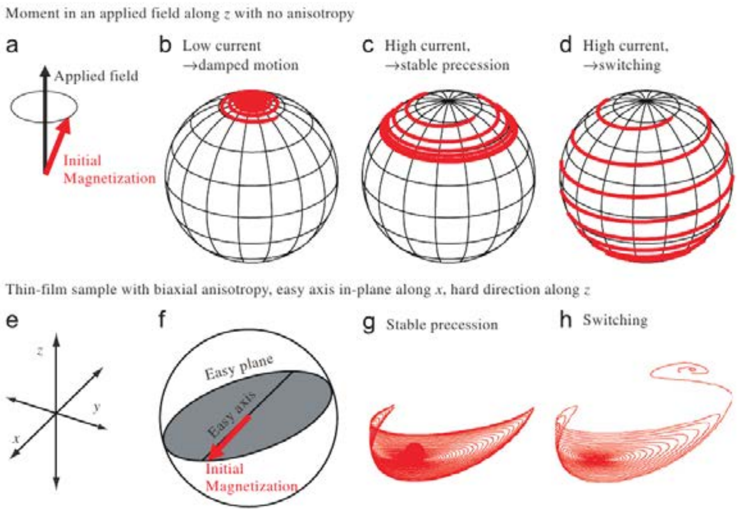

Figure 3.6: Magnetization trajectories in the presence of spin transfer torque. [a-d] represents an effective field along z. [e-h] The sample is assumed with a strong in-plane anisotropy and a weak uniaxial anistropy. Figure extracted from [34]

3.4 Effet of the Spin Transfer Torque on Trajectories

We will now describe qualitatively the effect of the spin transfer torque on the magnetization trajectories.

We first assume an effective field along the z direction as represented on Figure 3.5.

When the magnetization is not aligned with the effective field, it will precess in a circle around it, in the absence of damping. Adding a damping torque will align the magnetization with the effective field, the magnetization precesses around the effective field with the angle of the precession gradually decreasing (see Figure 3.6(b)).

As previously described, the spin transfer torque orientation depends on the sign of the current, it can be parallel or antiparallel with the damping torque.

If the spin transfer torque is aligned with the damping, it will only increase the effective damping, and the magnetization will align with the effective field more rapidly (see Figure 3.6(c)).

In the case of a spin torque antiparallel with the damping, but weaker in intensity, it will decrease the effective damping, and the magnetization will spiral more slowly to the effective field (see Figure 3.6(b)).

If the spin torque exactly compensates the damping torque, the magnetization precesses around the effective field at a certain angle (see Figure 3.6(c)).

The last possibility is high currents opposite to the damping. In that case, the precession angle will increase, until it reaches π: the magnetization is reversed (see Figure 3.6(d)).

Let's now assume a multilayer with strong in-plane anistotropy and a weaker uniaxial anisotropy along one of the in-plane axes.
For low currents, the magnetization precesses along an approximate elliptical trajectory (see Figure 3.6g). For larger currents, the precession state becomes unstable, the precession angle increases until it reaches π, thus reversing the magnetization (see Figure 3.6(h)).

3.5 Current Loops

In the case of CPP structures, two mechanisms are in competition: the self field created by a large current, which can produce vortices, and the spin transfer torque exerted on the magnetization which will make the reversal happen. The difference between both mechanisms is a scale difference, $1/d$ for the former and $1/d^2$ for the latter, d being the diameter of the nanomagnet. This means spin transfer effect is a lot more important in very small devices, such as nanopillar spin valves. This is why spin transfer torque offers great opportunities in high density non volatile memory, and the importance of studying current induced magnetization reversal.
In 2000, Albert et al. reported such a reversal for Co/Cu/Co spin valves.[37] The nanopillars were composed of Cu(80 cm)/Co(40 nm)/Cu(6 nm)/Co(2.5 nm)/Au(10 nm), and the shape was a 60 nm x 130 nm hexagon. They measured the differential resistance dV/dI in function of the applied field, represented on Figure 3.7(a), and showed a sharp reversal at low field values ($H_C = \pm 50$ Oe) (the reader is referred to section 7.1 page 93 for a detailed description of the differential resistance).
However, the differential resistance was also measured in function of the injected current, shown on Figure 3.7(b). It clearly shows the two possible states of the spin valve, i.e. antiparallell for the upper branch, and parallel for the lower one. The AP→P and P→AP reversals respectively happen for $I \simeq -4$ mA and $I \simeq 2$ mA. We may first note that the current induced reversal is asymmetric contrary to the reversal with field. This is characteristic of spin transfer effect, as the switching currents given in table 3.1 depend on the angle ϑ between both magnetizations found in the scalar function $g(\vartheta)$ ($g(0)$ or $g(\pi)$ here). For those measurements, the current is defined positive when the spin polarized electrons flow from the nanomagnet to the hard layer. At high positive currents, the spin valve configuration is antiparallel, which is expected, as the electrons flow from the nanomagnet to the polarizer, and the minority spin polarized electrons, reflected from the hard layer, tranfer enough spin angular momentum to the ferromagnet to force it into an antiparallel alignment. In the case of high negative currents, the parallel state is observed since the electrons flow from the polarizer to the ferromagnet and force it in a parallel alignment.

The difference of resistance between the antiparallel and parallel configurations is noticeably the same for both cycles (Figure 3.7(a) and Figure 3.7(b)), confirming the equivalence of the two measurements. It was thus the first time current induced reversal was demonstrated[8] on spin valves with in-plane anisotropy.
The first measurements on materials with perpendicular magnetization anisotropy were done by Mangin et al. in 2006.[20] The dV/dI versus H and dV/dI versus I loops are represented on Figure 3.8, and we can see they are look similar to Figure 3.7.

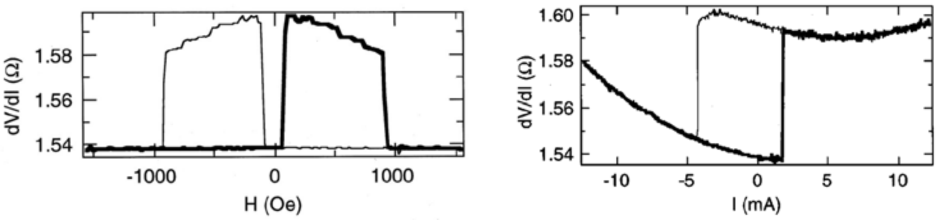

(a) Differential resistance in function of the applied field

(b) Differential resistance in function of the injected current

Figure 3.7: Field and current loops of a Cu/Co/Cu spin valve. The nanopillar has an elongated hexagon shape of 60 nm x 130 nm dimensions. The current is defined positive when the spin-polarized electrons are flowing from the nanomagnet to the polarizer. Figures extracted from [37]

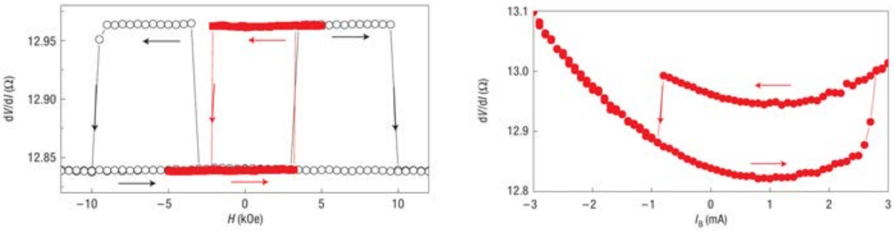

(a) dV/dI vs H

(b) dV/dI vs I

Figure 3.8: Current and field loops. Figures extracted from [20]

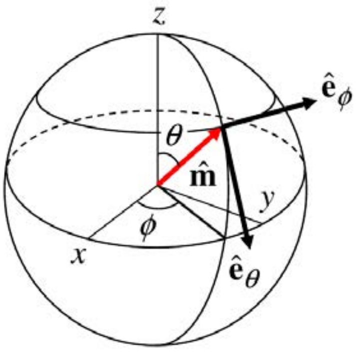

Figure 3.9: Definition of the angles ϑ and φ

3.6 Spin Transfer Effets on the Stoner Wohlfarth Astroid

The spin transfer torque changes the magnetization trajectories. It is therefore expected that the hysteresis cycles will be affected by the current, and consequently the astroid.
Let's consider a ferromagnet with uniaxial anisotropy along the z direction. The magnetization is separated from the z axis by an angle ϑ, and there is an angle φ with the x axis (see Figure 3.9).

At equilibrium, the magnetization $\mathbf{m}$ is aligned with the effective field $\mathbf{H}_{\text{eff}}$. Therefore the equilibrium conditions are:

$$\begin{cases} (\mathbf{H}_{\text{eff}} \cdot \mathbf{e}_\vartheta)_0 = 0 \\ (\mathbf{H}_{\text{eff}} \cdot \mathbf{e}_\phi)_0 = 0 \end{cases} \tag{3.24}$$

where the 0 subscript designs the equilibrium.
It is then possible to determine the stability criterion for the magnetization using the modified Landau Lifshitz Gilbert equation for the small current limit. With an analysis of the linear stability around the equilibrium position ϑ_0, one can found:

$$\frac{\partial}{\partial\vartheta}\left[\alpha(\mathbf{H}_{\text{eff}} \cdot \mathbf{e}_\vartheta) - j\,\frac{\beta(\vartheta)}{\gamma_0}\sin\vartheta\right]\Bigg|_{\vartheta=\vartheta_0} \leq 0 \tag{3.25}$$

where α is the damping constant, j is the current density, $\gamma_0 = \gamma\mu_0$, and

$$\beta(\vartheta) = \frac{\gamma_0 \hbar g(\vartheta)}{2\mu_0 M_S t e} \tag{3.26}$$

with $g(\vartheta)$ the angular dependence, t the thickness of the magnetic layer, M_S the spontaneous magnetization.
Combining equations (3.24) and (3.25),we obtain

$$\begin{cases} H_y = H_k \sin^3\vartheta_0 - j\sin\vartheta_0 C(\vartheta_0) \\ H_z = -H_k \cos^3\vartheta_0 - j\cos\theta_0 C(\vartheta_0) \end{cases} \tag{3.27}$$

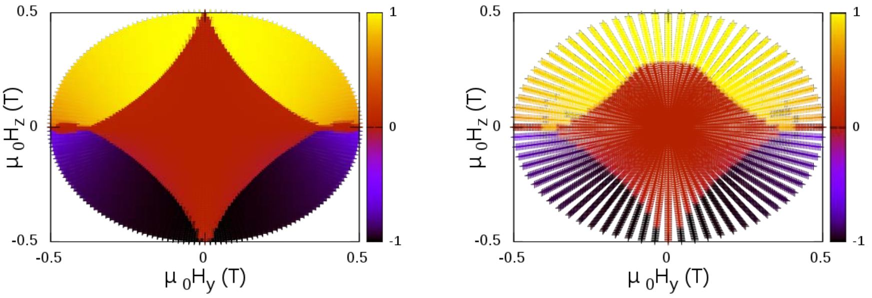

(a) I = 0 mA (b) I = 3 mA

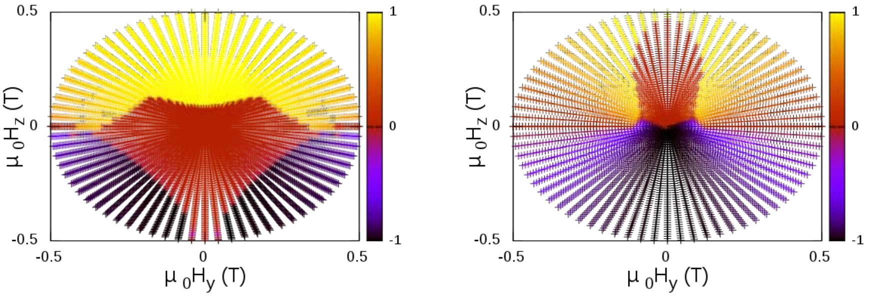

(c) I = 5 mA (d) I = -5 mA

Figure 3.10: Calculated astroids for different injected current values.

with H_k the anisotropy field, and

$$C(\vartheta_0) = \frac{1}{\alpha\gamma} \left.\frac{\partial(\beta \sin\vartheta)}{\partial\vartheta}\right|_{\vartheta=\vartheta_0} \tag{3.28}$$

where $C(\vartheta_0)$ are correction terms due to the spin transfer torque. We can see the effect on Figure 3.10 presenting calculated astroids for different values of the current. The color defines the magnetization value along z. The yellow, red and purple colors respectively represent a parallel, bistable and antiparallel states. On Figure 3.10(a), the astroid is plotted for a zero current. The shape is identical to the Stoner-Wohlfarth astroid we drew in section 1.3.1 page 27 (Figure 1.6). Figures 3.10(b) and 3.10(c) show the influence of a positive current on the astroid, respectively 3 mA and 5 mA. We can see the bistable region is reduced and the parallel state, i.e. $m_z = 1$, can be obtained for smaller positive fields H_z. However, it is important to note this effect is asymmetric. Although the bistable region in reduced for positive fields, there is no effect for negative H_z. On the other hand, when applying a negative current, -5 mA on Figure 3.10(d), there is an effect on the whole astroid. Indeed, the bistable region only appears in the upper half of the diagram, while the lower half shows an antiparallel state.

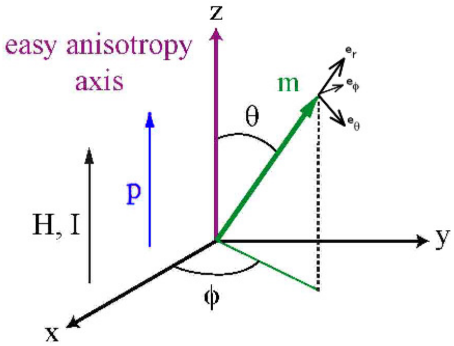

Figure 3.11: Orientation of the magnetization unit vectors **m** and **p**, applied field **H** and injected current I relative to the x,y,z axes in the case of a purely uniaxial symmetry.

3.7 State Diagrams

We shall here concentrate on the study of a state diagram (also called phase diagram, switch diagram or stability diagram in the literature) which is a map of the equilibrium magnetic states available in the $(H,\, I)$ parameter space similar to what was described earlier in [38]. The state diagram gives a complete and readable picture on the impact of the applied magnetic field and of the spin polarized current on the magnetization. In the literature, both experimental and theoretical state diagrams in $(H,\, I)$ or $(H,\, V)$ space were done previously for spin valves with in plane,[13,39,40,11,41] perpendicular[20,42,43,44,18,45,46,47,48] or both[49,50,51] anisotropy, and for magnetic tunnel junctions.[52,53,54] The aim of this section is to describe in detail how to measure, model and interpret such a state diagram with the goal to understand the effect of the intrinsic (linked to the materials properties) and the extrinsic parameters (controlled during the experiments) on the magnetization state.

In this section, we focus on a simple uniaxial anisotropy symmetry approach to describe the system. For this symmetry, the contributions of the effective magnetic field, the magnetization, the polarizer layer and current are along the same axis. Considering a spin valve structure with a hard layer, whose magnetization unit vector **p** acts as a polarizer, and a free layer whose magnetization M_S has a unit vector **m**. The free layer magnetization is affected by various interactions that can be taken into account by defining an effective field ($\mathbf{H}_{\text{eff}}$) being given by the sum of all fields: the dipolar field ($\mathbf{H}_{\text{dip}}$) created by the hard layer, the anisotropy field ($\mathbf{H}_{\mathbf{k}}$) created by the magneto-crystalline anisotropy, the shape anisotropy or demagnetization field $H_{\text{dem}} = -M_S$ in the thin film approximation i.e. the free layer thickness is supposed much smaller than the nanopillar width, and the applied field **H**.

$$\mathbf{H}_{\text{eff}} = \mathbf{H} - \mathbf{H}_{\text{dip}} + \mathbf{H}_{\mathbf{k}} + \mathbf{H}_{\text{dem}} \tag{3.29}$$

The LLGS equation is given by

$$\frac{d\mathbf{m}}{dt} = -\gamma_0 \mathbf{m} \times \mathbf{H}_{\text{eff}} + \alpha \mathbf{m} \times \frac{d\mathbf{m}}{dt} - \frac{\beta I g(\vartheta)}{\gamma_0} \mathbf{m} \times (\mathbf{m} \times \mathbf{p}) \tag{3.30}$$

where the free layer magnetization dynamic is ruled by three torques: the effective field torque ($\boldsymbol{\Gamma}_{\text{eff}} = -\gamma_0 \mathbf{m} \times \mathbf{H}_{\text{eff}}$), the damping torque ($\boldsymbol{\Gamma}_{\text{damp}} = \alpha \mathbf{m} \times \frac{d\mathbf{m}}{dt}$) and the spin transfer torque ($\boldsymbol{\Gamma}_{\mathbf{ST}} = \frac{\beta I g(\vartheta)}{\gamma_0} \mathbf{m} \times (\mathbf{m} \times \mathbf{p})$ with $\beta = \frac{\hbar \gamma_0}{2 \mu_0 M_S V e}$ with V the volume, e the elementary charge, $\hbar$ the reduced Planck constant, α the damping constant, $g(\vartheta)$ the spin transfer efficiency function and with $\gamma_0 = \mu_0 \gamma$ the product of the gyromagnetic ratio γ and the vacuum permeability μ_0).
To determine the stable equilibrium positions of the system, equation (3.30) can be written using an apparent effective field $\mathbf{H}^*_{\text{eff}}$

$$\frac{d\mathbf{m}}{dt} = -\gamma_0 \mathbf{m} \times \mathbf{H}^*_{\text{eff}} + \alpha \mathbf{m} \times \frac{d\mathbf{m}}{dt} \tag{3.31}$$

where

$$\mathbf{H}^*_{\text{eff}} = \mathbf{H}_{\text{eff}} + \frac{\beta I g(\vartheta)}{\gamma_0} \mathbf{m} \times \mathbf{p} \tag{3.32}$$

which includes the effective magnetic field and the injected current contributions to the magnetization dynamics. If the damping constant α is small enough, the damping torque term can be approximated to $\boldsymbol{\Gamma}_{\text{damp}} = -\alpha \gamma_0 \mathbf{m} \times (\mathbf{m} \times \mathbf{H}_{\text{eff}})$. At equilibrium when $\frac{d\mathbf{m}}{dt} = 0$ the magnetization of the free layer is aligned with the effective field $\mathbf{H}^*_{\text{eff}}$. Therefore, the system of equations giving in spherical coordinates the equilibrium positions of the magnetization is

$$\begin{cases} \mathbf{H}^*_{\text{eff}} \cdot \mathbf{e}_\vartheta = 0 \\ \mathbf{H}^*_{\text{eff}} \cdot \mathbf{e}_\phi = 0 \end{cases} \tag{3.33}$$

To simplify the analytical study of their stability, we will make the assumption that the motion of the magnetization along the $\mathbf{e}_\phi$ direction is negligible from the reversal point of view. It implies that the magnetization remains close to the perpendicular direction at the equilibrium. Thanks to this approximation, the stability of the equilibrium positions is only determined by the action of the torques exerted on the magnetization along the $\mathbf{e}_\vartheta$ direction.
They have to maintain the magnetization in an equilibrium position to make it stable. Consequently, the stability criterion than can be used is

$$\frac{d}{d\vartheta} \left(\frac{d\mathbf{m}}{dt} \cdot \mathbf{e}_\vartheta \right) \Bigg|_{\vartheta = \vartheta_{\text{eq}}, \phi = \phi_{\text{eq}}} \leq 0 \tag{3.34}$$

Moreover, the ϑ dependence of the $g(\vartheta)$ function will not be taken into account during the derivation but each equilibrium position will be characterized by a different $g(\vartheta)$ value. For instance, $g(0)$ and $g(\pi)$ will represent the value of the $g(\vartheta)$ function respectively in the parallel and antiparallel states whatever is the angular position of these magnetic configurations.
To determine analytically the state diagram in the case of perpendicular anisotropy, the evolution of the switching currents as a function of the applied magnetic field starting from a parallel or an antiparallel magnetic state need to be calculated. The switching occurs when these stable equilibrium positions become unstable based on the stability criterion given by equation (3.34). A first and simple approach to describe current-induced magnetization reversal in nanopillar spin-valves is to consider the hard layer magnetization as fixed and the free layer magnetization as uniform. They can be modeled as macrospins in a uniaxial symmetry potential. Indeed in that case the magnetocrystalline anisotropy

axis, the applied magnetic field and the flowing current are along the z direction. Consequently the effective field is along z and derives from the expression of the magnetic energy of the system given by

$$E(\vartheta, H) = kV \sin^2 \vartheta - \mu_0 M_S V H \cos \vartheta \tag{3.35}$$

The effective field is given by

$$\mathbf{H}_{\text{eff}} = -\frac{1}{\mu_0 M_S V} \frac{dE}{d\mathbf{m}} = (H + H_k \cos \vartheta)\mathbf{e_z} \tag{3.36}$$

where $H_k = \frac{2k}{\mu_0 M_S}$ and the apparent effective field $\mathbf{H}^*_{\text{eff}}$ is given by

$$\mathbf{H}^*_{\text{eff}} = \frac{\beta I g(\vartheta)}{\gamma_0} \left[(\sin \vartheta \sin \phi)\mathbf{e_x} - (\sin \vartheta \cos \phi)\mathbf{e_y}\right] + (H + H_k \cos \vartheta)\mathbf{e_z} \tag{3.37}$$

From equation (3.32), the equilibrium positions are the solutions of the following equation:

$$\begin{cases} (H + H_k \cos \vartheta) \sin \vartheta = 0 \\ I \sin \vartheta = 0 \end{cases} \tag{3.38}$$

The valid solutions at any injected current correspond to the exact parallel or antiparallel magnetic configurations, that is to say $\vartheta = 0$ or π. Their stability is determined by the criterion given by

$$(h + g(\vartheta)i) \cos \vartheta + \cos 2\vartheta|_{\vartheta=0 \text{ or } \pi} \geq 0 \tag{3.39}$$

Here, we used reduced coordinates for the applied magnetic field $h = H/H_k$ and for the injected current $i = \frac{\beta I}{\alpha \gamma_0 H_k}$. From the above expression, we can deduce that the parallel and the antiparallel states are respectively stable only if the current $I \geq I^P_{sw}(H)$ or $I \leq I^{AP}_{sw}(H)$

$$i^P_{sw}(h) = -\frac{h+1}{g(0)} \Leftrightarrow I^P_{sw}(H) = -\frac{2e\mu_0}{\hbar} \frac{\alpha M_S V}{g(0)} (H + H_k) \tag{3.40}$$

$$i^{AP}_{sw}(h) = -\frac{h+1}{g(\pi)} \Leftrightarrow I^{AP}_{sw}(H) = -\frac{2e\mu_0}{\hbar} \frac{\alpha M_S V}{g(\pi)} (H - H_k) \tag{3.41}$$

The theoretical determination of the switching currents given by equations (3.40) and (3.41) allows to build the state diagram of a nanopillar spin-valve with perpendicular magnetizations in this uniaxial approach (see Figure 3.12). The theoretical expressions of the switching currents respectively in the parallel and in the antiparallel states divide the (H, I) plane into two regions, one where the equilibrium position is stable and one where it is unstable based on the stability criterion given by equation (3.34). The border line between these two regions is given by the equation of the switching current evolution as a function of the applied magnetic field. The state diagram of Figure 7.5(a) is a combination of the information given by equations (3.40) and (3.41). Since the spin-transfer torque is more efficient in the antiparallel configuration than in the parallel one the slopes of the two borders which depend on the $g(\vartheta)$ function are different. So, they cross and divide the (H, I) plane into four regions. In three of them the magnetization has access to at least one stable magnetic configuration: parallel, antiparallel or both of them. In the fourth one, there

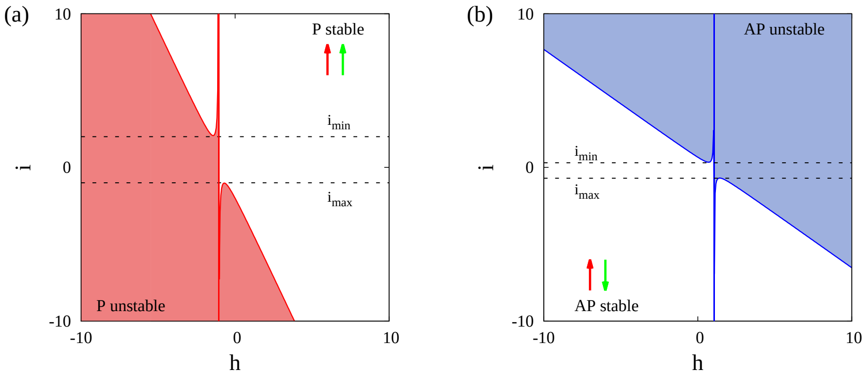

(a) Parallel state (b) Antiparallel state

Figure 3.12: Stability diagrams in the applied magnetic field and injected current plane in reduced coordinates. The colored areas correspond to the unstable regions and the lines to the theoritical evolution of the switching currents with the applied magnetic field.

are no stable and static magnetic states anymore. Therefore, the magnetization has to be in a dynamic state where $\frac{d\mathbf{m}}{dt} \neq 0$.

Such theoretical state diagrams have been described in the literature by different methods.[39, 20, 55, 51] A careful analytical study of the fourth region shows that steady magnetization precessions around the perpendicular axis are expected.[51]

Chapitre 4

Modèle de Sun

The previous chapters have described magnetization dynamics with the help of the Landau Lifshitz Gilbert equation and the spin transfer torque. Moreover we didn't take the temperature into account. In this chapter, we will focus on the magnetization reversal time, which is of utmost importance. Indeed, a good comprehension of the reversal time can open the way to even faster device applications like STT-MRAM.
This chapter will first present the thermal activation regime. Afterwards, we will focus on the Sun model, which describes magnetization reversal at short time scales. The last part will present experimental results from Bedau et al.[19] linking thermal activation and the short time regime.

4.1 Thermal Activation Regime

The model used to describe the thermal activation regime was taken from [56]. In order to take the temperature into account, we can introduce a Langevin field H_L, which simply adds noise to the system. Its expression is given by

$$H_{L,i} = \sqrt{\frac{2\alpha k_B T}{\gamma_0 M_S V}} I_{ran,i}(t) \tag{4.1}$$

where $I_{ran,i}$ $(i = x, y, z)$ is a gaussian random function, k_B the Boltzmann constant, T the temperature, V the volume.
We can rewrite the LLG equation as:

$$\frac{d\mathbf{m}}{dt} = -\gamma_0 \mathbf{m} \times [\mathbf{H}_{\text{eff}} + \mathbf{H_L}] + \alpha \mathbf{m} \times \frac{d\mathbf{m}}{dt} \tag{4.2}$$

As this equation depends on the Langevin field, its solutions will never be the same. A statistical analysis is needed.

The temperature now allows for magnetization reversal, when the latter is in a bistable state. Both minima are separated by a barrier potential ΔU following the Boltzmann statistics. The probability of the magnetization reversal is given by

$$P(t) = 1 - \exp^{-t/\tau} \tag{4.3}$$

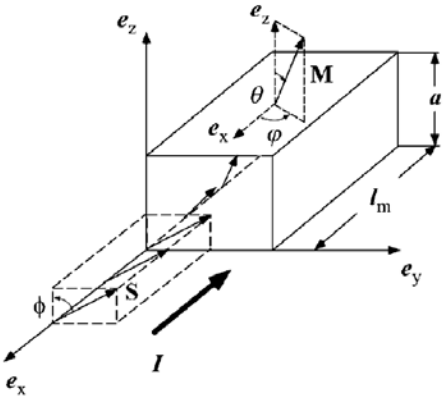

Figure 4.1: Geometry of the system. Figure extracted from[17]

where τ is the mean lifetime of the system, and $1/\tau_0$ the attempt frequency

$$\tau = \tau_0 \exp\left(\frac{\Delta U}{k_B T}\right) \tag{4.4}$$

Integrating the spin transfer torque in equation (4.2), it becomes

$$\frac{d\mathbf{m}}{dt} = -\gamma_0 \mathbf{m} \times (\mathbf{H}_{\text{eff}} + \mathbf{H}_{\mathbf{L}}) + \alpha \mathbf{m} \times \frac{d\mathbf{m}}{dt} - \beta I g(\vartheta) \mathbf{m} \times (\mathbf{m} \times \mathbf{p}) \tag{4.5}$$

In the case of the polarizer parallel with the effective field, and if the damping is small enough we can write $\mathbf{\Gamma}_{\text{damp}} = -\alpha\gamma_0 \mathbf{m} \times (\mathbf{m} \times \mathbf{H}_{\text{eff}})$, the modified LLG equation becomes

$$\frac{d\mathbf{m}}{dt} = -\gamma_0 \mathbf{m} \times (\mathbf{H}_{\text{eff}} + \mathbf{H}_{\mathbf{L}}) - \tilde{\alpha}\gamma_0 \mathbf{m} \times (\mathbf{m} \times \mathbf{H}_{\text{eff}}) \tag{4.6}$$

where $\tilde{\alpha} = \alpha(1 + I/I_{sw})$ with

$$I_{sw} = \frac{\alpha\gamma_0 H_{\text{eff}}}{\beta g(\vartheta)} \tag{4.7}$$

Equation (4.6) is equivalent to the LLG for a macrospin at temperature $\tilde{T}$ with a damping $\tilde{\alpha}$. Similarly to equation (4.2), we can rewrite the thermal activation lifetime in function of $\tilde{\alpha}$ and $\tilde{T}$.

$$\tau = \tau_0 \exp\left(\frac{\Delta U}{k_B \tilde{T}}\right) = \tau_0 \exp\left[\frac{\Delta U}{k_B T}\left(\frac{\tilde{\alpha}}{\alpha}\right)\right] = \tau_0 \exp\left[\frac{\Delta U}{k_B T}\left(1 - \frac{I}{I_{sw}}\right)\right] \tag{4.8}$$

4.2 Sun Model: Short Time Regime

In 2000, Jonathan Sun developed an expression for the magnetization reversal time in the macrospin model.[17] The ferromagnetic object is defined as a macrospin which can be described by the Stoner-Wohlfarth model. Its size is given by the product of the thickness t and the surface S.

An applied field **H**, an uniaxial anisotropy along the z direction, and an easy-plane anistropy in the $y-z$ plane, x being its normal direction, due to the shape anisotropy are considered (see Figure 4.1 for a sketch).
The starting point is the potential energy U given by:

$$U(\vartheta, \varphi) = k[\sin^2\vartheta + h_P \sin^2\vartheta \cos^2\varphi - 2h(\sin\vartheta \sin\varphi \sin\psi + \cos\vartheta \cos\psi)] \quad (4.9)$$

where $h_P = k_P/k$, $k_P = 2\pi M_S^2$ being the easy-plane anisotropy energy, and $h = H/(2k/M_S)$. The first term is the the uniaxial anisotropy, the second one is the in-plane anistropy while the third term corresponds to the applied field. Hence, we can calculate the torque applied on the magnetization per unit volume:

$$\frac{\mathbf{\Gamma_U}}{t} = -\mathbf{m} \times \nabla U(\vartheta, \phi) \quad (4.10)$$

In addition to the torques obtained from the three interactions described above, there is another one created from the absorption of the angular momentum in the direction perpendicular to the magnetization. This fourth torque is:

$$\mathbf{\Gamma_4} = s\mathbf{m} \times (\mathbf{p} \times \mathbf{m}) = 2tkh_s\mathbf{m} \times (\mathbf{p} \times \mathbf{m}) \quad (4.11)$$

where $s = (\hbar/2e)\eta J$ is the spin-angular momentum deposition per unit time. η is the spin polarization factor of the incident current J given by:

$$\eta = \frac{J_\uparrow - J_\downarrow}{J_\uparrow + J_\downarrow} \quad (4.12)$$

And h_S is the dimensionless spin current amplitude:

$$h_S = \frac{s}{2tk} = \frac{\left(\frac{\hbar}{2e}\right)\eta I}{2Vk} \quad (4.13)$$

The LLG equation can then be rewritten as:

$$\frac{d\mathbf{m}}{dt} + \alpha\left(\mathbf{m} \times \frac{d\mathbf{m}}{dt}\right) = \frac{1}{2}\Omega_k \sum_{i=1}^{4}\left(\frac{\Gamma_i}{tk}\right) \quad (4.14)$$

where $\mathbf{\Omega_k} = \gamma H_k$ is a characteristic frequency.
Introducing a new time unit $\tau = \Omega_k t/(1+\alpha^2)$, the LLG becomes:

$$\begin{bmatrix}\theta' \\ \phi'\end{bmatrix} = \sum_{i=1}^{4}\begin{bmatrix}\theta'_i \\ \phi'_i\end{bmatrix} \quad (4.15)$$

If we are in uniaxial geometry with the applied field **h** and the spin direction **p** are along the easy axis $\mathbf{e_z}$ with $h_p = 0$, equation 4.15 becomes:

$$\frac{d\vartheta}{d\tau} = -\vartheta[\alpha(1+h) + h_S] \quad (4.16)$$

$$\frac{d\phi}{d\tau} = -(1+h) + \alpha h_S \quad (4.17)$$

with the following solution:

$$\theta(\tau) = \vartheta_0 e^{-\tau/\tau_1} \quad (4.18)$$

$$\tau_1 = \frac{1}{\alpha(1+h) + h_S} \quad (4.19)$$

and a threshold spin current:

$$h_{SC} = -\alpha(1+h) \tag{4.20}$$

It is then easy to obtain the reversal time τ from equation (4.18):

$$\tau(\theta) \approx |h_S - h_{SC}|^{-1} \ln \frac{\vartheta}{\vartheta_0} \tag{4.21}$$

It is clear from the reversal time expression that the initial angle ϑ_0 has a significant role in the reversal process. τ is also proportional to the damping α. If we look at the large current limit, the reversal time becomes:

$$\tau(\theta) \propto \frac{1}{|h_S|} \ln \frac{\vartheta}{\vartheta_0} \tag{4.22}$$

Here, τ is independent of the damping, only the amount of spin current injected will influence the reversal time.
For more clarity, equation 4.21 can be rewritten as:

$$\frac{1}{\tau} = A(I - I_{C_0}) \tag{4.23}$$

This last equation describes the reversal time as a function of the dynamic parameter A, the critical current and the zero temperature critical current I_{C_0}. It will be discussed in part IV, as we will study the magnetization reversal time thanks to this equation.

4.3 Validity of both Regimes

In the two previous sections, we described the thermal activation regime and the Sun model. We will now confront them with the experiments done by Bedau et al.[19]
They studied the magnetization reversal of spin valves with perpendicular magnetic anisotropy. The spin valve description can be found in section 6.1 page 79 and in [20]. The free layer is a [Co/Ni] multilayer with a room temperature coercive field of 0.1 T. The hard layer is composed of multilayers of [Co/Pt] and [Co/Ni]. The nanopillars are shaped in 50 x 100 nm^2 squares.
To study the magnetization reversal of the spin valves, current pulses of different durations and amplitudes are injected. Repeating the measurement hundreds of times for each duration and amplitude, the probability can be found.
Figure 4.2 shows the current pulse amplitude needed to obtain a 50% reversal of the spin valve as a function of the pulse duration. The inset shows the switching rate in function of the injected current for short pulse durations. It is linear, hence obeying $A(I_C - I_{C_0})$. On the main plot, the dashed and dashed-dotted lines respectively correspond to fits obtained with the Sun model and the thermal activation regime. We can clearly see the switching behavior follows the Sun model for short pulse durations ($\tau < 10$ ns). It also fits perfectly with the thermal activation regime for longer pulses ($\tau > 1$µs). Nevertheless, there is an intermediate region, which cannot be fitted by either model, called the crossover regime. Figure 4.3 shows the switching probability as a function

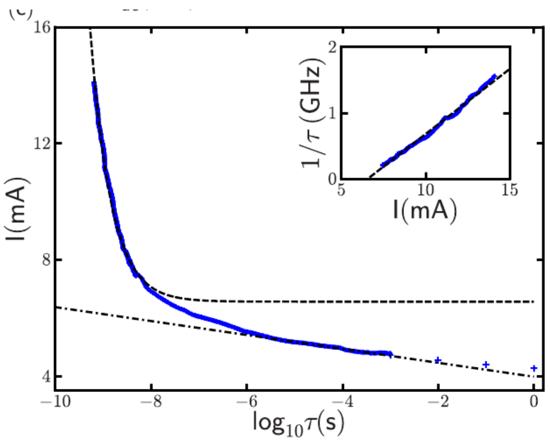

Figure 4.2: Pulse amplitude to observe a 50% reversal of the spin valve from the antiparallel to the parallel state. The pulse durations range from 0.3 ns up to 1 s. Inset: switching rate vs pulse amplitude for short pulses showing $\tau^{-1} \propto (I - I_{C_0})$, I_{C_0} is the intercept. The dashed line in the main figure shows this behavior on a logarithmic scale. The dashed dotted line is a fit to the long-time data.Figure extracted from [19]

of the pulse duration for the three different regimes. It is clear the switching probability presents different behaviors depending on the pulse duration. The curves are sigmoidal for the short time limit (Figure 4.3(a)), whereas the probability varies exponentially with the pulse duration for the long time limit (Figure 4.3(c)). Only the intermediate regime doesn't fit properly. It means both thermal fluctuations and the spin transfer are important, and both have to be taken into account.

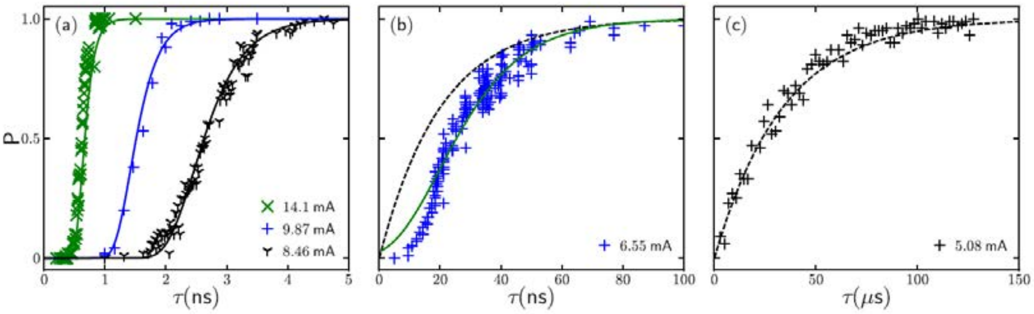

Figure 4.3: Switching probability vs pulse duration in three regimes. (a) Short time limit (b) Intermediate regime (c) Long time limit. The solid lines are fits using the Sun model and the dashed lines are obtained from the thermal activation model. Figure extracted from [19]

Deuxième partie

Modèle macrospin

Résumé

french Cette partie présente le programme de simulation macrospin développé au cours de cette thèse. Nous décrivons dans une première partie la structure du programme et les différents algorithmes utilisés. Dans une deuxième partie, nous présentons les différents types de diagrammes obtenus par simulation.

Le programme fut développé en C++ car le langage est très utilisé, et ainsi connu de beaucoup de physiciens. Ce langage est aussi particulièrement adapté pour le développement de l'interface graphique. Il permet la programmation objet, qui est une caractéristique très intéressante dans notre situation.
La programmation objet fournit, entre autres, des classes qui sont des types définis par l'utilisateur dont l''instanciation donne des objets. Ces classes sont composées d'attributs correspondant à des types usuels comme des nombres ou des chaînes de caractères ainsi que des fonctions pouvant agir sur ces attributs. Elles présentent la propriété intéssante d'héritage qui implique qu'une classe héritant d'une autre contiendra tous ses attributs et fonctions.
La majorité des objets physiques et mathématiques peuvent être décrits à l'aide de classes qui permettent de rendre le programme plus compréhensible et aisé à programmer.
Un objet horloge regroupera, par exemple, les différents temps utilisés durant la simulation, c'est-à-dire le temps physique qui s'écoule, le calcul commençant à $t = 0$, mais aussi les temps d'intervalle pour l'intégration.
Un vecteur mathématique est aussi défini, il est composé de trois composantes selon x,y et z, les calculs étant effectués en coordonnées cartésiennes, et des fonctions donnant la somme, le produit scalaire, le produit vectoriel de deux vecteurs, ainsi que le produit d'un vecteur et d'un scalaire.
Les champs physiques peuvent donc ensuite être décrits comme des vecteurs ce qui est le cas du champ appliqué, du champ d'anisotropie magnétocristalline et du champ démagnétisant.
Le courant est aussi défini dans une classe et peut prendre trois formes différentes. Il est soit constant, soit un pulse de durée et d'amplitude déterminée, ou bien encore un double pulse pour lesquels l'utilisateur donne les amplitudes et durées des deux pulses ainsi que la durée entre les deux.
Les couples (torques ?) sont définis dans une classe héritant des vecteurs. Il s'agit des termes obtenus dans l'équation de Landau Lifshitz Gilbert que nous séparons en deux couples. Le premier, appelé *AloneTorque* correspond aux termes ne comprenant que l'aimantation de la couche libre et le champ effectif. *SpinTorque*, quant à lui, comprend les termes avec l'aimantation de la couche polarisante.
Les couches minces sont définies par des objets dont les attributs sont les diffé-

rents paramètres de la couche comme sa taille, son anisotropie, son aimantation à saturation... Ces différentes couches sont rassemblées dans un objet multicouches afin de simuler une vanne de spin. Bien que cette thèse ne porte que sur des vannes de spin vcomposées d'une couche libre et d'une couche dure, il est possible de choisir deux couches libres et une couche dure.

Le dernier objet défini est la polarisation qui reprend la formule de Slonczewski.

Le coeur du programme est la résolution de l'équation de Landau Lifshitz Gilbert. Celle-ci est réalisée à l'aide de l'algorithme de Runge-Kutta-Cash-Karp (RKCK) qui est une variante de l'algorithme de Runge-Kutta, utilisant un pas d'intégration variable et qui permet d'en contrôler l'erreur. Cette partie s'appuie sur les algorithmes fournis par la librairie scientifique GNU (GSL).

Un algorithme Runge-Kutta a été créé afin d'appeler la fonction RKCK de la GSL, en calculant les éléments nécessaires à la résolution de la LLG, c'est-à-dire les matrices définissant les aimantations des deux couches minces, ainsi que leur jacobien.

Cet algorithme est lui-même appelé dans la procédure appelée *EvolveAlgo* qui résoud la LLG à un temps t. Une fois l'aimantation calculée, elle est normalisée.

Il existe deux possibilités pour terminer la simulation, soit le temps total de calcul donné en paramètre par l'utilisateur est atteint, soit le couple de forces total est inférieur à la limite donnée par l'utilisateur. En effet, si le couple est trop faible, nous pouvons considérer qu'il ne sera pas en état de modifier l'aimantation. À chaque temps t, le couple total est donc calculé et comparé à la valeur limite.

Dans certains cas, il est nécessaire de savoir si l'aimantation de la couche libre a été renversé. Pour le vérifier, une trajectoire est calculée sans champ extérieur ni courant, mais avec une aimantation initiale opposée. L'aimantation finale alors obtenue est comparée. Si les deux aimantations finales sont égales avec une marge d'erreur définie par l'utilisateur, l'aimantation est considérée comme renversée.

Le programme dispose d'interfaces graphique et console pour lesquelles les paramètres peuvent être entrés de manière différentes. Les paramètres sont stockés dans un fichier écrit en xml, un langage permettant un traitement facile des données.

L'interface graphique permet d'entrer directement les paramètres. Elle est séparée en différents onglets correspondant au choix de simulation, au courant, au champ et à la vanne de spin. L'interface graphique est facile d'utilisation.

L'interface console ou en mode texte ne propose que le choix de simulation et du nom du fichier de résultats. Les paramètres doivent être entrés directement dans le fichier correspondant et le programme s'arrête après une simulation. Il faut donc le relancer à chaque fois contrairement à l'interface graphique. Le principal intérêt de cette interface est le fait qu'on puisse utiliser le programme à distance.

Le programme est ainsi capable de générer des trajectoires, qui sont à la base de tous les autre types de diagramme. La trajectoire commence à être calculée à $t = 0$, pour lequel l'algorithme *EvolveAlgo* est appelé. On vérifie ensuite que l'on n'a pas atteint le temps de simulation maximal, ainsi que la valeur de torque est supérieur à la limite. L'intervalle de temps défini par l'utilisateur est ensuite ajouté au temps t défini dans l'objet horloge et le processus recommence jusqu'à ce qu'un des critères d'arrêt soit rempli.

Les trajectoires permettent de calculer les cycles d'hystérésis. Il s'agit d'utiliser une boucle qui commence au champ minimal et augmente jusqu'à un champ maximal avec des intervalles définis. Pour chaque champ, une trajectoire est calculée en prenant comme aimantation initiale, celle obtenue au champ précédent. Le processus est répété du champ maximal au champ minimal pour obtenir la deuxième branche.

Un autre type de cycle que l'on peut obtenir de la même manière que les cycles d'hystérésis sont les cycles de résistance en fonction du courant R(I). Dans ce cas, le champ extérieur est gardé constant et c'est le courant que l'on fait varier d'un minimum à une valeur maximale avec un pas donné, puis la procédure est répétée de la valeur maximale à minimale.

L'algorithme pour les diagrammes d'états génère douze fichiers correspondants aux trois composantes x, y et z pour des configurations initiales parallèles, antiparallèles et les moyenne et différence de ces derniers. Un diagramme est obtenu en calculant les trajectoires pour chaque champ et courant donnés. Ces derniers sont donnés par des valeurs minimale, maximale et de pas. Les abscisses du diagramme d'état correspondent à des cycles R(I) alors que chaque ordonnée donne un cycle d'hystérésis.

L'astroïde est obtenue en calculant des trajectoires pour différentes angles et valeurs de champ pour les configurations parallèles et antiparallèles. Leur moyenne correspond aux cycles d'hystérésis à différents angles ce qui nous donne l'astroïde de Stoner-Wohlfarth.

Le diagramme courant-longueur de pulse de courant est équivalent au diagramme d'état en remplaçant le champ par la durée de pulse. Il fait apparaîte naturellement la frontière de renversement d'aimantation.

Le diagramme courant critique en fonction de la durée de pulse donne les mêmes résultats que le diagramme précédent mais il nécessite beaucoup moins de calculs. En effet, le courant critique est recherché avec la méthode du point du milieu, ce qui est beaucoup plus efficace. Il donne ainsi pour différentes durées de pulse le courant critique.

Chapitre 5

Description du programme de simulation

The main goal of this thesis is to study the behavior of magnetization dynamics in a spin valve, in the presence of a magnetic field and subjected to a polarized current. To this end, we created a software simulating macrospins. We chose the C++ language, because of its universality, the fact it's an object oriented language and also its easy integration with Qt, the language used for the graphic interface.
The objectives of the program is to be able to calculate trajectories of the magnetization in the presence of a magnetic field and an injected current, as well as hysteresis loops, state diagrams or Stoner-Wohlfarth astroids. Another aim of the program is to simulate current pulses in order to calculate switching rates of the magnetization.

5.1 Structure

5.1.0.1 Classes in C++

As it was previously said, C++ is an object oriented language, which means an important feature is the object. Objects are instances of user defined types called classes, for which we give an overview, as they are used frequently in the software.
Classes are composed of attributes and functions. The attributes can be numbers or character strings among others, and the functions are the same as in any other language.
An interesting property of classes is the inheritance: one class can inherit from another, i.e. one class will possess all the members (attributes, functions...) from the parent class in addition to the ones specific to itself.

5.1.1 Mathematical and Physical Objects

5.1.1.1 Clock

The LLGS equation (3.23) is a differential equation, which means time is an essential part of the problem. As there are current pulses, time is also neces-

sary to define them. To take time into account, we created an object called *Clock*(12.1).
This object contains four attributes:

timeStamp: it's the physical time elapsed since the beginning of the calculation

timeStep: step used in the integration algorithm

timeWindow: the duration of the calculation if it isn't stopped by another criteria

maxTimeStep: maximum time step used in the integration algorithm

5.1.1.2 Vectors

As vectors are constantly used in magnetism for fields or magnetization, among others, an object called *Vector3*(12.2) was introduced. Its main objective is to simplify the code as we don't need to detail the equations for all components; it will be taken care of by the four different functions defined here:

add: this function adds two vectors **a** and **b** and stores the result of the addition in **a**.

dotProduct: calculates the scalar product between **a** and **b** and returns the result.

crossProduct: calculates the cross product between **a** and **b** and stores the result in **a**.

mult: multiplies the vector with a scalar

Although the parameters are entered in spherical coordinates, the calculations are done in the Cartesian coordinate system thanks to this transformation matrix:

$$\begin{aligned} x &= r\cos\theta\sin\phi \\ y &= r\sin\theta\sin\phi \\ z &= r\cos\phi \end{aligned} \tag{5.1}$$

5.1.1.3 Fields

The different fields present in the system are added together in an effective field $\mathbf{H_{eff}}$ which contains:

the external Field(12.3): At the time t, the external field is the product of the B-field and the vacuum permeability μ_0 using the coordinate transformation matrix(5.1).

$$\mathbf{H_{ext}} = \begin{cases} \mu_0 B(t)\sin\phi\cos\theta \\ \mu_0 B(t)\sin\phi\sin\theta \\ \mu_0 B(t)\cos\phi \end{cases} \tag{5.2}$$

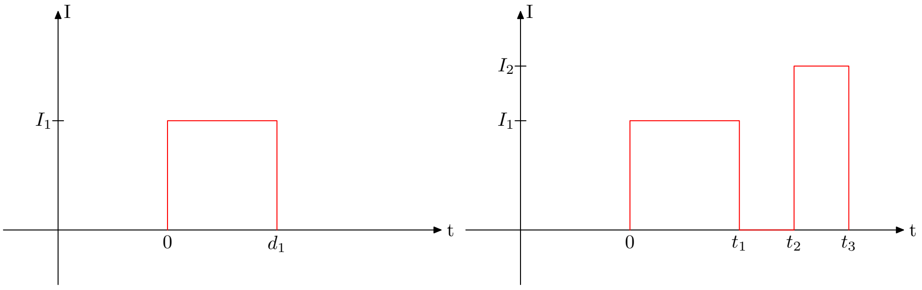

(a) Square Pulse (b) Double Square Pulse

Figure 5.1: Pulse Schemes

the anisotropy(12.4): as it was described in section **??**, the anisotropy fields for the first and second order are given by:

$$H_{K_1} = \frac{2K_1}{\mu_0 M_S} \qquad H_{K_2} = \frac{4K_2}{\mu_0 M_S} \tag{5.3}$$

A and **m** respectively represent the easy anisotropy axis and the magnetization directions, which give the field created by the anisotropy:

$$\mathbf{H_{ani}} = H_{K_1}\mathbf{A}(\mathbf{A}\cdot\mathbf{m}) + H_{K_2}\mathbf{A}(\mathbf{A}\cdot\mathbf{m})^3 \tag{5.4}$$

the Demagnetization(12.5): it was defined in section 1.2.4 and its expression is:

$$\mathbf{H_{demag}} = -M_S\mathbf{m}\widehat{N_D} \tag{5.5}$$

5.1.1.4 Current

Current is crucial in the simulations, as it is responsible for spin transfer(Chapter 3). It is possible to use constant current during the whole calculation, whereas to study fast dynamics, current pulses are needed. For now, two types of current pulses can be chosen:

square: it starts at the defined level I_1 at $t = 0$ and equals zero when the time elapsed reaches the pulse duration d_1.

doublesquare: there are five values to describe this pulse. It starts at the first level I_1 for the first pulse duration d_1, then the current goes to zero during the pulse delay, and then it equals the second level I_2 for the second pulse duration d_2 before going to zero for the rest of the calculation.

The pulses are represented on figure 5.1

5.1.1.5 Torques

The Landau-Lifshitz-Gilbert-Slonzewski equation(3.23) needs to be modified a little, as to obtain a form we can solve with a Runge-Kutta algorithm.

$$\frac{d\mathbf{m}}{dt} = -\gamma_0 \mathbf{m} \times \mathbf{H_{eff}} + \alpha \mathbf{m} \times \frac{d\mathbf{m}}{dt} - \beta \mathbf{m} \times (\mathbf{m} \times \mathbf{p}) \tag{5.6}$$

$$\mathbf{m} \times \frac{d\mathbf{m}}{dt} = -\gamma_0 \mathbf{m} \times (\mathbf{m} \times \mathbf{H_{eff}}) + \alpha \mathbf{m} \times (\mathbf{m} \times \frac{d\mathbf{m}}{dt}) - \beta \mathbf{m} \times (\mathbf{m} \times (\mathbf{m} \times \mathbf{p})) \tag{5.7}$$

$$\mathbf{m} \times \frac{d\mathbf{m}}{dt} = -\gamma_0 \mathbf{m} \times (\mathbf{m} \times \mathbf{H_{eff}}) - \alpha \frac{d\mathbf{m}}{dt} + \beta \mathbf{m} \times \mathbf{p} \tag{5.8}$$

$$\frac{d\mathbf{m}}{dt} = -\gamma_0 \mathbf{m} \times \mathbf{H_{eff}} + \alpha \left[-\gamma_0 \mathbf{m} \times (\mathbf{m} \times \mathbf{H_{eff}}) - \alpha \frac{d\mathbf{m}}{dt} + \beta \mathbf{m} \times \mathbf{p} \right] - \beta \mathbf{m} \times (\mathbf{m} \times \mathbf{p}) \tag{5.9}$$

$$(1 + \alpha^2) \frac{d\mathbf{m}}{dt} = -\gamma_0 \mathbf{m} \times \mathbf{H_{eff}} - \alpha\gamma_0 \mathbf{m} \times (\mathbf{m} \times \mathbf{H_{eff}}) + \beta(\alpha \mathbf{m} \times \mathbf{p} - \mathbf{m} \times (\mathbf{m} \times \mathbf{p})) \tag{5.10}$$

$$\frac{d\mathbf{m}}{dt} = -\frac{\gamma_0}{1+\alpha^2} \mathbf{m} \times \mathbf{H_{eff}} - \frac{\alpha\gamma_0}{1+\alpha^2} \mathbf{m} \times (\mathbf{m} \times \mathbf{H_{eff}}) + \frac{\alpha\beta}{1+\alpha^2} \mathbf{m} \times \mathbf{p} - \frac{\beta}{1+\alpha^2} \mathbf{m} \times (\mathbf{m} \times \mathbf{p}) \tag{5.11}$$

Equation (5.11) is obtained by making the cross product of $\mathbf{m}$ and equation (5.6) and using the following formula:

$$\mathbf{a} \times (\mathbf{b} \times \mathbf{c}) = \mathbf{b}(\mathbf{a} \cdot \mathbf{c}) - \mathbf{c}(\mathbf{a} \cdot \mathbf{b}) \tag{5.12}$$

To simplify (5.11), we use new coefficients $\bar{\gamma_0}$, $\bar{\alpha}$, $\bar{\beta_1}$, $\bar{\beta_2}$ and finally have:

$$\boxed{\frac{d\mathbf{m}}{dt} = -\bar{\gamma_0} \mathbf{m} \times \mathbf{H_{eff}} - \bar{\alpha} \mathbf{m} \times (\mathbf{m} \times \mathbf{H_{eff}}) + \bar{\beta_1} \mathbf{m} \times \mathbf{p} - \bar{\beta_2} \mathbf{m} \times (\mathbf{m} \times \mathbf{p})} \tag{5.13}$$

Equation (5.13) is composed of four terms that can be gathered into two different torques.

AloneTorque(12.6): it corresponds to the first two terms in equation (5.13). It only includes the effective field(5.1.1.3) and corresponds to the effect on the layer without taking into account the other layers, which is why it is called *AloneTorque*.

$$\mathbf{\Gamma_{alone}} = -\bar{\gamma_0} \mathbf{m} \times \mathbf{H_{eff}} - \bar{\alpha} \mathbf{m} \times (\mathbf{m} \times \mathbf{H_{eff}}) \tag{5.14}$$

SpinTorque(12.7): this torque incorporates the other terms of (5.13) and includes interactions with the other layer(s) through $\mathbf{m} \times \mathbf{p}$.

$$\mathbf{\Gamma_{spin}} = \bar{\beta_1} \mathbf{m} \times \mathbf{p} - \bar{\beta_2} \mathbf{m} \times (\mathbf{m} \times \mathbf{p}) \tag{5.15}$$

TotalTorque(12.8): it is simply the sum of the previously described torques

$$\mathbf{\Gamma_{total}} = \mathbf{\Gamma_{alone}} + \mathbf{\Gamma_{spin}} \tag{5.16}$$

5.1.2 Sample

The calculations are done with a multilayer sample, the number of layers is chosen by the user, although it is restricted to one or two free layers.
An object called *Layer* is created with the *CreateLayer* algorithm(12.9) and has different parameters as attributes. Those parameters are, among others, the characteristics of the material, such as k_1, k_2, m_S or α, but also whether the magnetization is fixed (free or hard layer), its position in relation to other layers, the initial magnetization (see 12.9) for the exhaustive list of parameters).
MultiLayer(12.10) repeats this process until all the layers are created.

5.1.3 Polarization

The polarization(12.11) between two layers with the magnetizations $\mathbf{m}$ and $\mathbf{p}$ is inversely proportional to the scalar factor g[6] which is:

$$g^{-1} = -4 + \frac{(1+P)^3 \cdot (3\mathbf{m} \cdot \mathbf{p})}{4P^{3/2}} \tag{5.17}$$

with P the polarization of the layer with the magnetization $\mathbf{m}$.

5.2 Landau Lifshitz Gilbert Equation Resolution

5.2.1 Runge-Kutta Algorithms

The common fourth-order Runge-Kutta and the Cash-Karp methods description were taken from [57, 58]

5.2.1.1 Explicit Classic Fourth-Order Method

Let an initial value problem be specified as follows
$y' = f(t, y)$ and $y(t_0) = y_0$

$$y_{n+1} = y_n + \frac{1}{6}(k_1 + 2k_2 + 2k_3 + k_4) \tag{5.18}$$

$$t_{n+1} = t_n + h \tag{5.19}$$

$$k_1 = hf(t_n, y_n) \tag{5.20}$$

$$k_2 = hf\left(t_n + \frac{1}{2}h, y_n + \frac{1}{2}k_1\right) \tag{5.21}$$

$$k_3 = hf\left(t_n + \frac{1}{2}h, y_n + \frac{1}{2}k_2\right) \tag{5.22}$$

$$k_4 = hf(t_n + h, y_n + k_3) \tag{5.23}$$

k_1 is the delta based on the slope at the beginning of the interval, using y_n (Euler's method)
k_2 is the delta based on the slope at the midpoint of the interval, using $y_n + k_1/2$
k_3 is again the delta based on the slope at the midpoint, but now using $y_n + k_2/2$
k_4 is the delta based on the slope at the end of the interval, using $y_n + k_3$.

In averaging the four deltas, greater weight is given to the deltas at the midpoint:

$$\delta = \frac{k_1 + 2k_2 + 2k_3 + k_4}{6} \tag{5.24}$$

5.2.1.2 Runge-Kutta Cash-Karp(4,5) Method

The Runge-Kutta Cash-Karp[59] method is an embedded one, that is to say, it is designed to produce an estimate of the local truncation error of a single Runge-Kutta step, and as result, allow to control the error with adaptive stepsize. This is done by having two methods in the tableau, one with order p and one with order p-1.
The lower-order step is given by

$$y^*_{n+1} = y_n + h \sum_{i=1}^{s} b^*_i k_i \tag{5.25}$$

where the k_i are the same as for the higher order method. Then, the error is

$$e_{n+1} = y_{n+1} - y^*_{n+1} = h \sum_{i=1}^{s} (b_i - b^*_i) k_i \tag{5.26}$$

which is $O(hp)$. The Butcher Tableau for this kind of method is extended to give the values of b^*_i

$$\begin{array}{c|cccc}
c_1 & a_{11} & a_{12} & \cdots & a_{1s} \\
c_2 & a_{21} & a_{22} & \cdots & a_{2s} \\
\vdots & \vdots & \vdots & \ddots & \vdots \\
c_s & a_{s1} & a_{s2} & \cdots & a_{ss} \\
\hline
 & b_1 & b_2 & \ldots & b_s \\
 & b^*_1 & b^*_2 & \ldots & b^*_s
\end{array}$$

The extended has two methods of order 5 and 4. Its extended Butcher Tableau is:

$$\begin{array}{c|cccccc}
0 & & & & & & \\
1/5 & 1/5 & & & & & \\
3/10 & 3/40 & 9/40 & & & & \\
3/5 & 3/10 & -9/10 & 6/5 & & & \\
1 & -11/54 & 5/2 & -70/27 & 35/27 & & \\
7/8 & 1631/55296 & 175/512 & 575/13825 & 44275/110592 & 253/4096 & \\
\hline
 & 37/378 & 0 & 250/621 & 125/594 & 0 & 512/1771 \\
 & 2825/27648 & 0 & 18575/48384 & 13525/55296 & 277/14336 & 1/4
\end{array}$$

The first row of b coefficients gives the fifth-order accurate solution, and the second row has order 4.

5.2.1.3 Software algorithms

The Runge-Kutta algorithms are solved thanks to two files called *OneLayerRungeKutta*(12.12) and *TwoLayerRungeKutta*(12.13) used respectively for samples with one free layer or two free layers. They both are composed of three functions called *llg(3)*, *jac(3)*, *rungekutta(3)* defined in the Gnu Science Library (GSL).

llg(3): defines the constants and parameters found in the LLG equation(5.13) into a column matrix $p[\,]$ and $d\mathbf{m}/dt$ in $f[\,]$.

jac(3): defines the Jacobian J of $d\mathbf{m}/dt$:

$$J = \begin{pmatrix} \frac{\partial}{\partial x}\left(\frac{d\mathbf{m}}{dt}\right)_x & \frac{\partial}{\partial y}\left(\frac{d\mathbf{m}}{dt}\right)_x & \frac{\partial}{\partial z}\left(\frac{d\mathbf{m}}{dt}\right)_x \\ \frac{\partial}{\partial x}\left(\frac{d\mathbf{m}}{dt}\right)_y & \frac{\partial}{\partial y}\left(\frac{d\mathbf{m}}{dt}\right)_y & \frac{\partial}{\partial z}\left(\frac{d\mathbf{m}}{dt}\right)_y \\ \frac{\partial}{\partial x}\left(\frac{d\mathbf{m}}{dt}\right)_z & \frac{\partial}{\partial y}\left(\frac{d\mathbf{m}}{dt}\right)_z & \frac{\partial}{\partial z}\left(\frac{d\mathbf{m}}{dt}\right)_z \end{pmatrix} \tag{5.27}$$

rungekutta(3): this is the function that will solve the LLG equation, using the *llg* and *jac* functions previously defined.

5.2.2 Calculation Algorithm

5.2.2.1 EvolveAlgo

An algorith called *EvolveAlgo* is used to solve the LLG equation. It simply calculates the total torque at a given time and calls the *OneLayerRungeKutta* or *TwoLayerRungeKutta* routine with all the system parameters. Once it gets the results, the vector magnetization is normalized. The final step is to return the final magnetization.

5.2.2.2 Torque Limit

One of the criteria to stop the calculation is the torque limit presented in 12.14. At a given time, it compares the norm of the total torque(5.1.1.5) Γ_{total} to the torque limit Γ_{lim} input in the parameters. If the norm is inferior to the limit, the calculation is stopped.

$$|\mathbf{\Gamma_{total}}^2| < \mathbf{\Gamma_{lim}} \tag{5.28}$$

5.3 Switching Criteria

For some simulations, it is necessary to know if the magnetization of the free layer reversed; that's when *SwitchingCheck*(12.20) comes into play. It simply checks if the three components of the magnetization are equal to the values of the magnetization we would have obtained, had its initial state been reversed. A 'switching tolerance' δ can be taken into account so the final configuration will need to be the reversed magnetization give or take the tolerance. This algorithm obeys the following steps:

- the initial position is $\mathbf{m} = (m_x, m_y, m_z)$

- a trajectory is computed with an inital magnetization of $\bar{\mathbf{m}} = (-m_x, -m_y, -m_z)$ and without any current
    - if $\bar{\mathbf{m}}_\mathbf{f} - \delta \leq \mathbf{m}_\mathbf{f} \leq \bar{\mathbf{m}}_\mathbf{f} + \delta$, the magnetization has been reversed
    - otherwise, the magnetization has not been reversed

5.4 User Interface

There are two ways to use the macrospin software, either with the graphical user interface(GUI) or with the console interface(CUI). While the GUI allows to change the system parameters and is more user friendly, the console mode is really efficient and has the great advantage of remote control.

5.4.1 Parameters File

The parameters file is crucial to make the software work. Although it can be created using the graphical interface, it can be as easy to modify the existing one. It is written in xml to allow a better access and modification of data. Although it can look complicated at first sight, it is quite simple as long as the structure is respected. An example of parameters file can be seen in 12.23.
We can see it is divided in different parts, e.g. current, field, sample... and there are also subdivisions. The different sections start with their name between chevrons i.e. <section> and end with the delimiter </section>. It differs a little for the subsections as it starts with a chevron with a label describing the different parameters found in that subsection and then the parameters and its value is written as ”parameter=’value’ ”, and we finally end the subsection with a ’/>’ symbol. The time parameters will thus look like :

```
<Time timeStep="5e-13" maxTimeStep="1e-10" timeWindow="5e-08"/>
```

5.4.2 Console Mode

The console mode is pretty basic and only offers the choice of simulation and to enter the output file name. All the parameters need to be entered in the parameters file before the beginning of the computation. It is very useful when there are only a few parameters varying, and contrary to the graphical interface, it is possible to see the progress of the computation.
The greatest advantage of this mode is that it can be run in a simple console, and thus be operated remotely from other computers.

5.4.3 Graphical Mode

The graphical mode offers a user friendly interface to input the parameters and run simulations. It is split in different tabs for the different features of the system. All the parameters can either be input in the system manually or be loaded from a parameters file. When the input is complete, it’s possible to save the parameters in the current file or another one. On a side note, all values need to be in the International System of Units(SI), every input box includes a tooltip with the unit for easier use.
The first tab presents the simulation choice and the computation parameters,

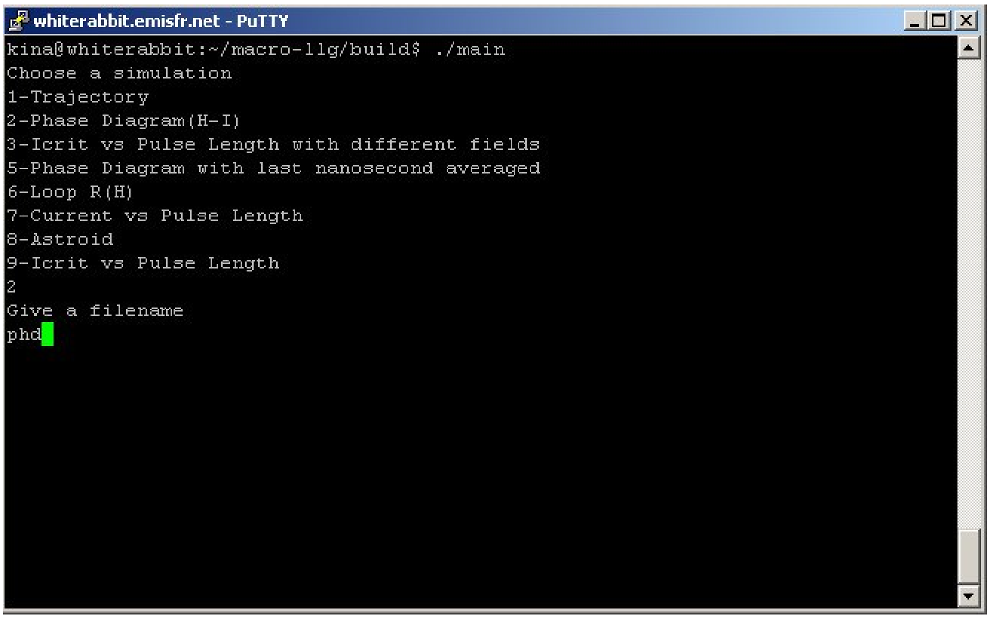

```
kina@whiterabbit:~/macro-llg/build$ ./main
Choose a simulation
1-Trajectory
2-Phase Diagram(H-I)
3-Icrit vs Pulse Length with different fields
5-Phase Diagram with last nanosecond averaged
6-Loop R(H)
7-Current vs Pulse Length
8-Astroid
9-Icrit vs Pulse Length
2
Give a filename
phd
```

Figure 5.2: Console user interface

which are necessary for any simulation e.g. the time steps and time window.

Depending on the simulation choice, the current tab will offer different parameters to fill. It is always possible to choose between a constant current and a current pulse. If a Current-Field state diagram is computed, then the maximum, minimum current as well as the step appear in boxes.

The field tab is a lot like the current tab, except there are also boxes for the angle for the field.

As the sample is defined for two or three layers, the first step is to choose the number of layers present in the system. Then all the parameters can be input for each layer, by selecting the right one with a radio button.

It usually is needed to get the results in a file for data analysis. Hence, there's a menu to choose the different variables wanted in the output file.

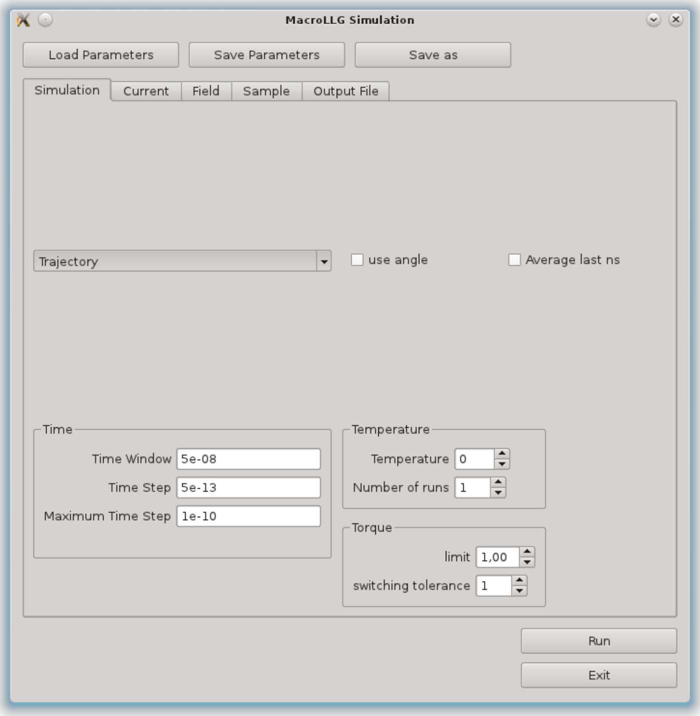

Trajectory

☐ use angle

☐ Average last ns

Time Window 5e-08

Time Step 5e-13

Maximum Time Step 1e-10

Temperature 0

Number of runs 1

limit 1,00

switching tolerance 1

Figure 5.3: Simulation Choice

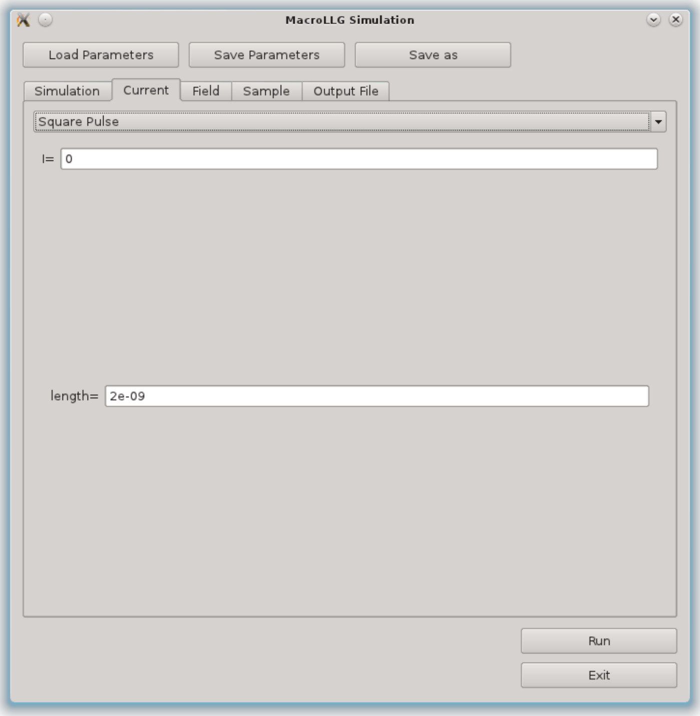

Square Pulse

I= 0

length= 2e-09

Figure 5.4: Current input

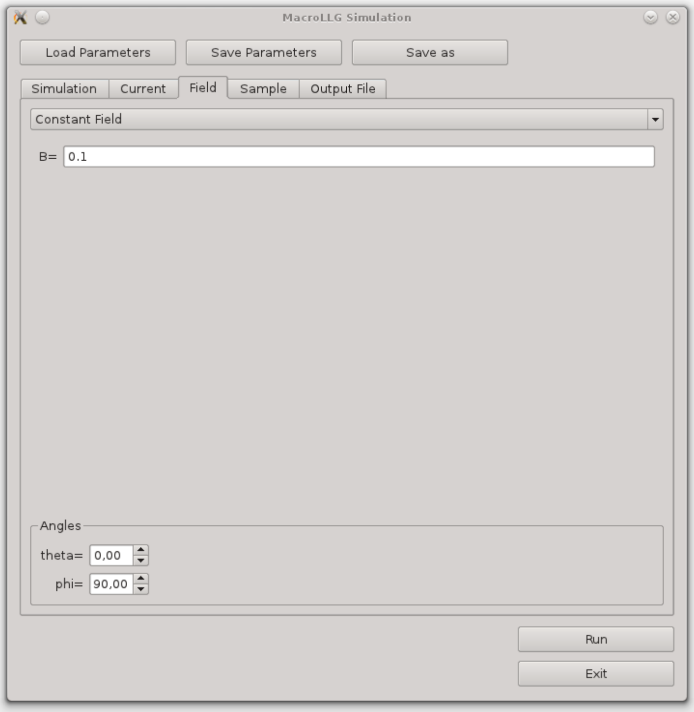

Constant Field

B= 0.1

theta= 0,00

phi= 90,00

Figure 5.5: Field input

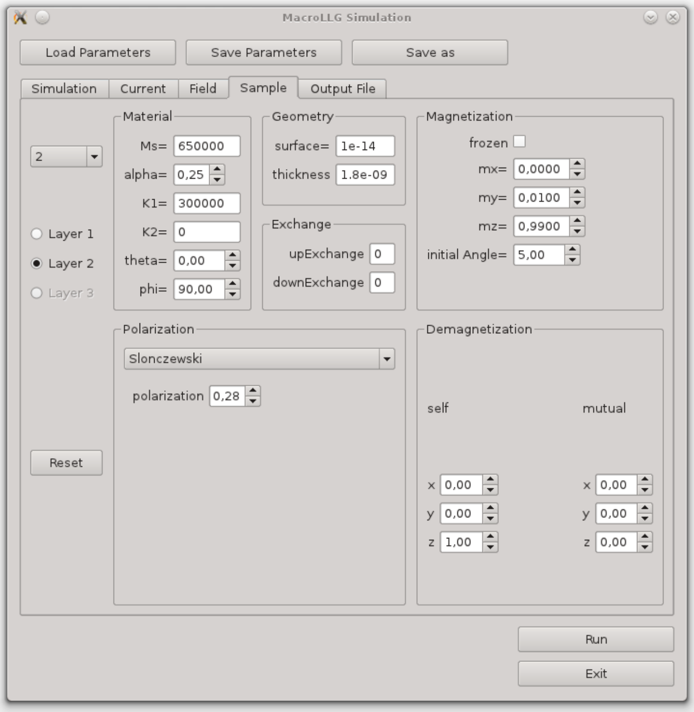

2

○ Layer 1
● Layer 2
○ Layer 3

Material
Ms= 650000
alpha= 0,25
K1= 300000
K2= 0
theta= 0,00
phi= 90,00

Geometry
surface= 1e-14
thickness 1.8e-09

Exchange
upExchange 0
downExchange 0

Magnetization
frozen ☐
mx= 0,0000
my= 0,0100
mz= 0,9900
initial Angle= 5,00

Polarization
Slonczewski
polarization 0,28

Demagnetization
self
x 0,00
y 0,00
z 1,00
mutual
x 0,00
y 0,00
z 0,00

Figure 5.6: Sample Parameters

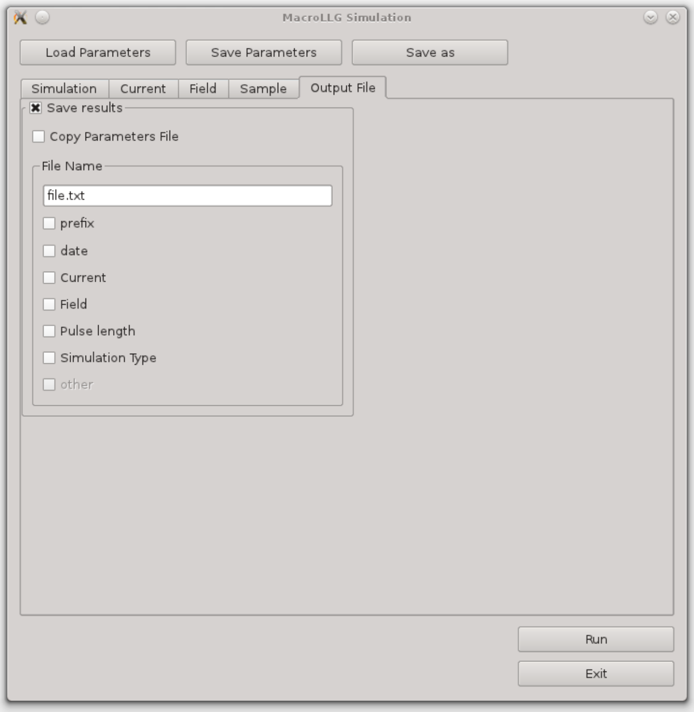

☒ Save results

☐ Copy Parameters File

File Name

file.txt

☐ prefix
☐ date
☐ Current
☐ Field
☐ Pulse length
☐ Simulation Type
☐ other

Figure 5.7: Output File Name Input

Chapitre 6

Exemples

6.1 Sample Description

The aim of the simulations was to explain the results obtained experimentally.[20, 44, 18] All the measurements were done on [Co/Ni] spin valves, which mere made at the Hitachi Global Storage Technologies center of research in San Jose, California. The spin valves are inside nanopillars whose structure is given on Figure 6.1. The samples were grown by sputtering and evaporation. Electron beam lithography and ion beam etching were then used to pattern the sample. Different shapes (circles, hexagons, ellipses and squares) as well as different size dimensions were made.

The spin valves are composed of a [Co/Ni] free layer, a copper spacer, and a hard layer comprised of a [Co/Pt] and a [Co/Ni] thin films. These materials were chosen because of their perpendicular magnetic anistropy.[60, 61]

To sample described above was simulated in the software. We used two layers, one free and one fixed whose parameters were chosen as close as the ones given in [20]. They are gathered in the following table.

	Hard layer	Free Layer
M_S (A.m^{-1})	$5 \cdot 10^5$	$6.5 \cdot 10^5$
α	0.01	0.25
polarization	0.1	0.28
thickness (m)	$1.8 \cdot 10^{-9}$	$1.8 \cdot 10^{-9}$
surface (m^2)	$5 \cdot 10^{-15}$	$5 \cdot 10^{-15}$
$\mathbf{n_d}$	(0,0,1)	(0,0,1)
k (J·m^{-1})	$3 \cdot 10^6$	$3 \cdot 10^5$
ϑ_{ani}	0	0
φ_{ani}	$\pi/2$	$\pi/2$

Table 6.1: Sample parameters used for the simulations

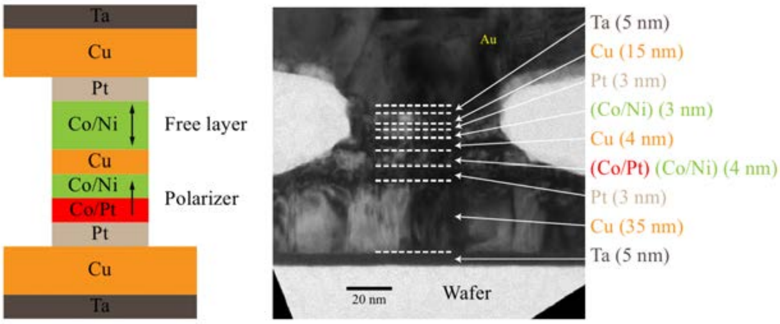

(a) Structure of the spin valve

(b) Electron microscopy image of the nanopillar

Figure 6.1: Nanopillar containing the measured spin valve

6.2 Magnetization Trajectory

We present here how to obtain magnetization trajectories. The trajectory calculations are done with the help of *TrajSimul*(12.15) and *TrajMeanSimul*(12.16). The algorithm uses *EvolveAlgo* described in section 5.2.2.1 and obeys the following steps:

1. the time t is set to zero
2. the LLG equation is solved thanks to *EvolveAlgo*
3. the magnetization and torques are saved in a file
4. checking that the time is still in the time window t_w
   - if $t \leq t_w$, we go to the next step
   - if $t > t_w$, the calculation is stopped
5. the total torque Γ_{total} is calculated and compared with the torque limit Γ_{lim}(5.2.2.2)
   - if $\Gamma_{total} < \Gamma_{lim}$, the simulation is stopped
   - if $\Gamma_{total} > \Gamma_{lim}$, the timestep is added to the time and we go back to step 2

The only parameters the user has to enter into the simulation are the current amplitude (and duration if it's a pulse) and the applied field (amplitude and angles). The output file contains 15 columns: the time, current, field, the three components of the magnetization, the alone torque, the spin torque, and the total torque. That way, it's possible to plot one component of the magnetization in function of time(Figure 6.2), or m_x, m_y and mz as a three dimensional plot (Figure 6.3).
On Figure 6.3, each point corresponds to the magnetization given by its three components m_x, m_y and m_z at a time t. At $t = 0$, the magnetization is along the z axis, with $m_z \simeq 1$.

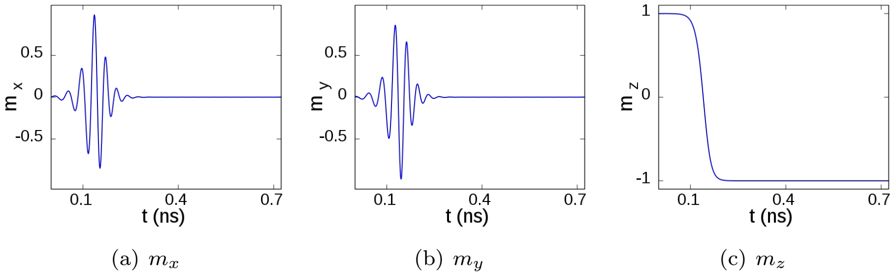

(a) m_x (b) m_y (c) m_z

Figure 6.2: Time evolution of the three components of the magnetization. The applied field is 1 tesla and no current is injected.

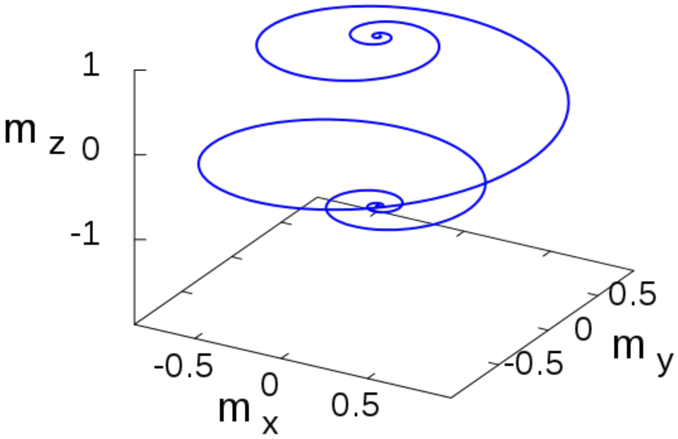

Figure 6.3: Trajectory of the magnetization at 1 Tesla and zero current. The initial magnetization is along z.

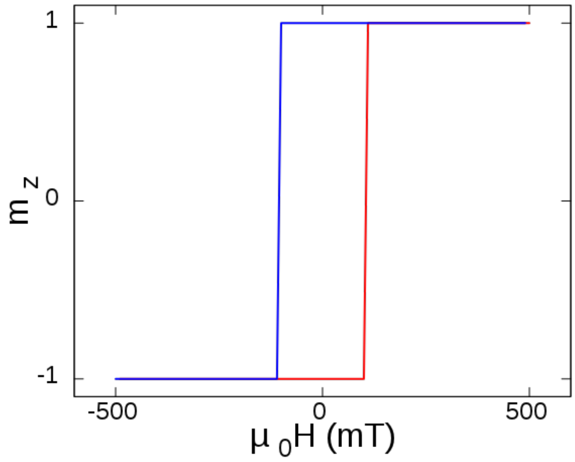

Figure 6.4: Hysteresis loop calculated between -500 mT and 500 mT at zero current. The red line represents the trajectories calculated with an increasing field, while the blue line is for the decreasing field.

6.3 Field Hysteresis Loop

The hysteresis loops, described in section **??** page **??** (see 12.17 for the complete algorithm) are easily performed thanks to the trajectory algorithm(6.2).
The user gives three values for the field scan, the minimum value H_{min}, the maximum H_{max} and the field step H_{step}. One can also enter a current. A trajectory every H_{step} following the cycle $H_{min} \rightarrow H_{max} \rightarrow H_{min}$. For each trajectory, the final magnetization is stored, and used as the initial magnetization for the following trajectory.
At the end of the simulation, one can plot the final magnetization as a function of the field from the output file. The latter contains the field and current amplitudes and the three components of the magnetization.
Figure 6.4 shows a hysteresis loop performed between -0.5 T and 0.5 T at zero current. For each plotted field corresponds a trajectory, the value of the magnetization (m_z on Figure 6.4) being the last value obtained during the calculation of the trajectory. The red and blue line respectively represent the increasing and decreasing field branches.

6.4 Current Scan

The current loops, described in section **??**, are equivalent to the hysteresis loops. The only difference is the exchange between current and field.
Indeed the user will enter a field and maximum, minimum and step values for the current. The current loop will thus follow $I_{min} \rightarrow I_{max} \rightarrow I_{min}$. As for the field loops, each trajectory final magnetization is used as the initial one for the next trajectory calculation. The final magnetizations are stored in an output file containing the current value, the field value and the three components of the magnetization. Figure 6.5 shows a current loop between -10 mA and 10 mA

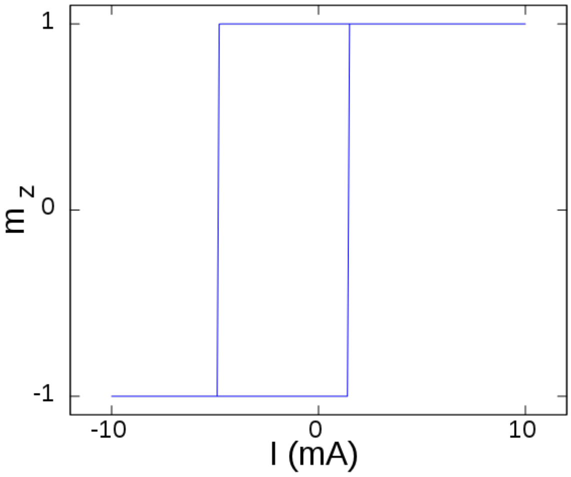

Figure 6.5: Evolution of the z component of the magnetization with the injected current between -10 mA and 10 mA at zero field

at zero field.

6.5 State Diagram

A detailed description of state diagrams is done in section **??**.
(H,I) state diagrams (12.19) are a combination of field (horizontally) and current scans (vertically). The user has to input maximum, minimum and step values for both current and field. This time, we will do a hysteresis cycle for each current value.
The results are stored in 2 x 3 files for the three components of the magnetization. For each magnetization, one file contains a matrix where each row represents the increasing field branch of the hysteresis for one current value and the other one contains the decreasing field branch. Afterwards, we just have to do the following operations on the matrices to obtain the half-sum or the difference of the magnetizations.

$$sum = \frac{m_{up} + m_{down}}{2} \qquad diff = m_{up} - m_{down} \tag{6.1}$$

Figure 6.6 shows the state diagrams representing the half-sum and difference of the final magnetizations between both branches of the hysteresis cycles.

6.6 Astroid

AstroidSimul(12.18) calculates an astroid from the Stoner-Wolfarth model(1.3.1). It calculates the hysteresis loop for different angles of the applied field. The user has to enter maximum, minimum and step values of the field angle in addition to the ones for the hysteresis loop.
As for the state diagrams, the final magnetizations are given six matrices corresponding to the three components of the magnetization for the increasing and

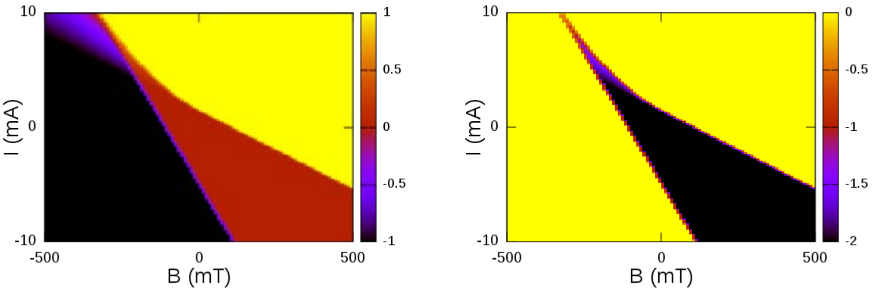

(a) half-sum of the z component of the magnetization (b) $m_{z,up} - m_{z,down}$

Figure 6.6: Theoritical state diagrams calculated between a field of -500 and 500 mT and a current of -10 mA and 10 mA.

decreasing field branches of the field. Figure **??** shows the half-sum of both branches of the hysteresis for different angles of the applied field.

6.7 Current vs. Pulse Diagrams

For current vs pulse duration diagrams(6.5), each point corresponds to a trajectory. The user has to enter the maximum, minimum and step values of the pulse duration and the current amplitude.
For each couple of (pulse duration, current value), a trajectory is calculated and the final magnetization is stored in a matrix. This time, there are only three output files corresponding to the matrices for the three components.

Figure 6.8 shows the switching probability of the spin valve as a function of current pulse amplitude and duration. Initially, the initial magnetization m_z is close to 1. The yellow and black color respectively represent the final magnetization m_z equal to 1 and -1.

6.8 Critical Current vs Pulse Length

It is possible to extrapolate the critical current defined in Chapter **??** from the current vs. pulse diagrams described in 6.7. However, this process takes too much time and resources. That's why the critical current I_C is obtained through the *ICritAlgo*(12.21) algorithm, which will give I_C for a certain pulse length between two current values I_{max} and I_{min}, chosen by the user with a defined precision. The algorithm uses a simple midpoint method described as follows:

1. three trajectories are calculated for I_{min}, I_{max} and $I_{1/2} = (I_{min}+I_{max})/2$. We call the final magnetizations $\mathbf{m_{min}}$, $\mathbf{m_{max}}$ and $\mathbf{m_{1/2}}$ for the sake of clarification.

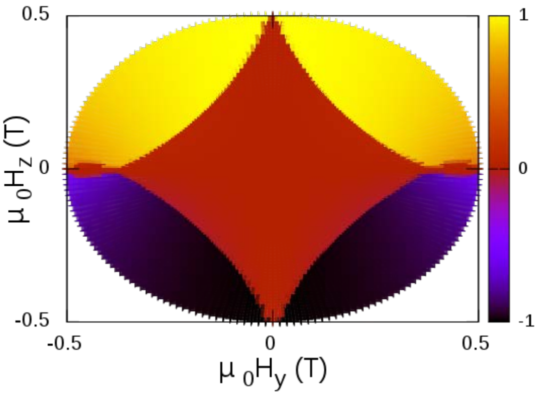

Figure 6.7: z component of the magnetization in function of fields between -500 mT and 500 mT and an angle between $-\pi$ and π

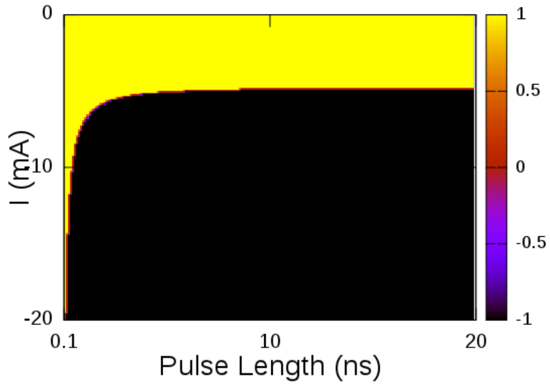

Figure 6.8: Diagram of the switching probability vs current value and pulse duration at zero field. Initially, the magnetization is almost aligned with the z direction, i.e. $m_z \simeq 1$.

2. for each trajectory, we check if there was a reversal of the magnetization with the help of the switching criteria (5.3)
    - if $\mathbf{m_{max}} = \mathbf{m_{min}} = \mathbf{m_{1/2}}$, the algorithm is stopped, as there is no critical current between I_{max} and I_{min}
    - if $\mathbf{m_{max}} = \mathbf{m_{1/2}} \neq \mathbf{m_{min}}$, we replace I_{max} by $I_{1/2}$
    - if $\mathbf{m_{max}} \neq \mathbf{m_{1/2}} = \mathbf{m_{min}}$, we replace I_{min} by $I_{1/2}$
3. the difference between I_{min} and I_{max} is calculated
    - if the difference is inferior to the defined precision, then I_{max} or I_{min} is chosen as the critical current, depending on which one is responsible for the magnetization reversal.
    - if the difference is bigger than the precision, the process goes back to step 1

The critical current vs. pulse length diagram is easily obtained by repeating the algorithm for different current pulse lengths. At the end of the simulation, we obtain an output file containing the pulse durations and the correspond critical currents. It is plotted on Figure 6.9.

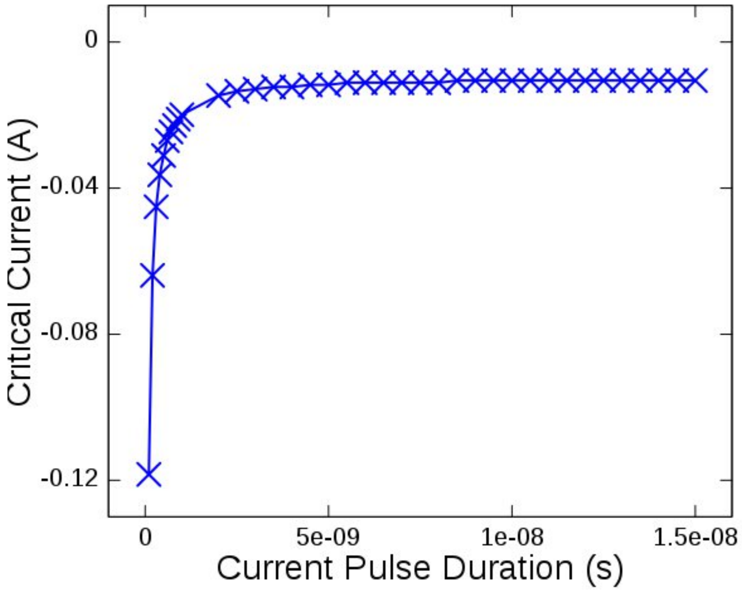

Figure 6.9: Critical current vs. pulse duration at zero field

Troisième partie

Dynamique d'aimantation à l'aide de diagrammes d'état

Résumé

Dans cette partie, nous utilisons un outil extrêmement utile pour étudier la dynamique de l'aimantation, il s'agit des diagrammes d'état. Ceux-ci donnent, pour un champ et un courant donnés, les états possibles de l'aimantation de la couche libre. Cet état est représenté par une couleur. Dans le cas de diagrammes d'état théoriques, nous avons directement accès à l'aimantation de la couche libre. En revanche, pour les diagrammes d'état expérimentaux, il nous faut les construire à partir des mesures de magnétorésistance géante. Deux types de diagramme d'état peuvent être obtenus à partir des valeurs de résistances collectées durant un cycle d'hystérésis.

En effet, il est obtenu en différenciant ou moyennant les aimantations finales provenant des états antiparallèles et parallèles. Avec la différence, nous obtenons trois zones correspondant à des vannes de spin qui restent dans la même configuration (la différence entre les deux états est alors nulle), une zone où l'on passe de la configuration antiparallèle à parallèle et la zone correspondant au changement inverse. Si l'on moyenne, nous avons accès à une zone où la vanne de spin est toujours dans l'état parallèle, une qui reste antiparallèle, et une autre zone correspondant à un retournement d'aimantation, aussi appelée zone de bistabilité. Finalement, il reste encore une zone de précession pour des forts courants. Nous utilisons principalement les diagrammes d'état obtenus avec la moyenne, car plus appropriés à notre situation.

D'après la théorie du transfert de spin, il a été montré que le courant de retournement est, dans le cas des vannes de spin à aimantation perpendiculaire, proportionnel au champ effectif ainsi qu'à la fonction scalaire $g(\vartheta)$ dépendante de l'angle entre les aimantations des deux couches. Ainsi, sur le diagramme d'état, les zones décrites précédemment, à l'exception de la précession, sont séparées par deux droites correspondant au courant de retournement et celles-ci possèdent des pentes différentes dues à la fonction scalaire (ϑ étant égal à 0 ou π). Cependant, la comparaison avec des diagrammes d'état expérimentaux montre des divergences assez importantes. Les diagrammes expérimentaux montrent, en effet, que le retournement d'aimantation est indépendant du courant pour des zones de courant assez faibles.

La théorie donnant le courant de retournement suppose une géométrie uniaxiale, c'est-à-dire, le champ appliqué est dans la même direction que l'axe facile d'aimantation. Nous allons donc briser cette symétrie dans le but de vérifier si elle ne serait pas à l'origine des résultats expérimentaux. De nombreuses simulations ont été effectuées pour différents paramètres brisant la symétrie du système.

Dans un premier temps, nous calculons des diagrammes pour différents angles d'anisotropie. Les résultats sont très clairs, et montrent qu'un angle d'anisotropie faible est amplement suffisant pour obtenir une zone de bistabilité où

le courant de retournement ne dépend que du champ appliqué. Nous pouvons remarquer que plus l'angle augmente, plus le courant seuil, pour retourner à un comportement linéaire du courant de retournement, augmente.
L'énergie d'anisotropie est définie à l'aide de constantes d'anisotropie de différents ordres. En ne tenant compte que des constantes d'ordre deux et quatre, un calcul simple de l'énergie totale du système montre que, pour des paramètres donnés, la constante d'anisotropie du quatrième ordre transforme un simple maximum en double puits. Néanmoins, les simulations ont montré qu'il était nécessaire d'ajouter au système un faible champ d'anisotropie dans le plan, physiquement équivalent à un champ dipolaire, pour briser la symétrie du système. Dans ce cas, les diagrammes d'état obtenus montrent bel et bien un effet de la constante de quatrième ordre sur le retournement d'aimantation. Cet effet reste limité par rapport à celui obtenu avec un angle d'anisotropie.
Une autre piste suivie est la variation de l'angle avec le champ appliqué. Dans ce cas, les diagrammes d'état présentent de nouveau un comportement invariant du courant de retournement proche de $I = 0$. Le courant seuil aumente aussi avec la valeur de l'angle. Contrairement à l'anisotropie, les angles nécessaires pour obtenir les mêmes résultats sont plus importants. L'effet du champ appliqué est donc plus faible.
Une dernière façon de briser la symétrie du système est de donner un angle au polariseur. Les diagrammes calculés pour différents angles avec le polariseur montrent des pentes pour le courant de retournement qui varient. Cependant, un comportement linéaire est observé à chaque fois. Nous ne pouvons qu'en conclure que l'effet du polariseur est trop faible pour briser la symétrie du système.
La variation des angles d'anisotropie ou du champ apppliqué permettent donc d'expliquer les diagrammes d'état obtenus expérimentalement.

Le programme a aussi été utilisé afin d'expliquer d'autres résultats expérimentaux. Les diagrammes d'état précédents étaient mesurés par la méthode du lock-in, c'est à dire en envoyant un faible courant électrique dont on connait la fréquence et nous permettant de mesurer la résistance dV/dI de la vanne de spin. Pour ces nouvelles mesures, un faible champ magnétique alternatif a été ajouté, afin de mesurer une nouvelle grandeur dV/dH. Celle-ci donne accès à des propriétés du système inconnues jusque là.
Des cycles d'hystérésis furent mesurés pour trois valeurs de courant, qui présentent de grandes différences. À 4 mA, seuls des processus irréversibles sont observés, contrairement à $I = 6$ mA. Des plateaux apparaissent dans la résistance pour un courant de 9.6 mA en absence de processus irréversible.
La comparaison entre dV/dI et dV/dH montre des zones similaires, mais une différence notable est une branche verticale visible pour dV/dH mais pas pour dV/dI. Cette différence est aussi obtenue avec les diagrammes d'état calculés. Les trajectoires calculées au niveau de cette branche verticales montre des états cantés, c'est-à-dire des états qui sont gelés à des angles bien définis.
Ainsi, bien que les simulations aient pu montré les domaines seulement visibles avec dV/dH, elles ne sont pas capables d'expliquer les plateaux de résistance observés à plus fort courant.

Chapitre 7

Problématique

Experimental measurements of current-induced resistance changes were first done in magnetic multilayers with spin torque driven excitations in 1998[9] and then in magnetic oxide junctions in 1999.[62] In 2000, magnetization reversal of a magnetic nano-object under a polarized current using a nanopillar spin-valve was demonstrated.[8] This has spurred extensive research in metallic spin-valve and magnetic tunnel junction (MTJ) nanopillar structures and development of new applications including spin-transfer torque magnetic random access memories (STT-MRAMs) and rf devices such as current-tunable microwave nano-oscillators (STNO).[13, 14, 63, 12] Implementation of STT-MRAM requires low critical currents to switch the nanomagnet while maintaining a sufficient thermal stability.[12] Toward this goal nanopillars with perpendicular magnetic anisotropy (PMA) have shown to be particularly interesting since they provide a way to lower the switching current. Indeed, as shown and described in this thesis the perpendicular geometry has a number of advantages over in-plane devices. The magnetic response is more strongly determined by the intrinsic properties of the materials rather than being dominated by the shape of the device. PMA is controllable by judicious engineering of material properties. High anisotropy materials with strong PMA provide stability against thermal activation down to smaller nanomagnet sizes than feasible with shape anisotropy alone.[64] Moreover, PMA materials are found to provide a model system to investigate the combine effect of applied magnetic field (H) and injected current (I).

We will focus on spin-valve structures with PMA for which their magnetic layers have an easy anisotropy axis pointing in the out-of-plane direction. Spin-valves with both the polarizer and the free layer having PMA is a uniaxial model system. Indeed all the contributions (fields, anisotropy axis, and current) in this system are expected to be aligned along the same perpendicular axis. Perpendicular geometry also provides a way to decrease the switching current required to observe current-induced magnetization reversal.[20, 21, 65, 66, 67] The reason of the larger magnetization reversal efficiency for the perpendicular case compared to the in-plane one comes from the effect of the demagnetizing field in the two geometries. Figure 7.1 and Table 7.1 point out the differences between these two cases. In the analytical expression of the switching current required to reverse the magnetization in the in-plane case, a constant term due to the demagnetization field is in addition to the in-plane anisotropy that suppresses reversal. In the perpendicular case the switching current is directly proportional to the

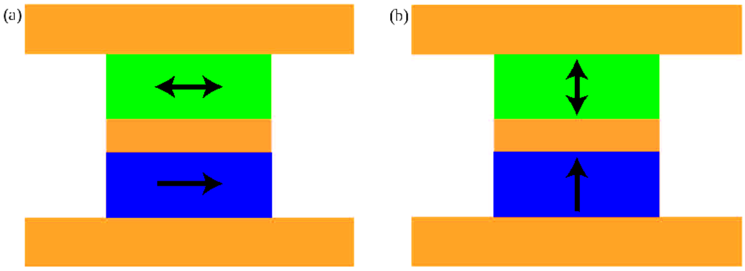

(a) in plane (b) out of plane

Figure 7.1: Sketch of a spin valve. The polarizer in blue has its magnetization fixed whereas the free layer in green can align parallel or antiparallel to it

	In plane	Out of plane
$H_{\text{eff}}^{P\to AP}$	$H + H_{\text{dip}} + H_{k_{\text{ip}}} + M_S/2$	$H + H_{\text{dip}} + (H_{k_{\text{oop}}} - M_S)$
$H_{\text{eff}}^{AP\to P}$	$-(H + H_{\text{dip}}) + H_{k_{\text{ip}}} + M_S/2$	$-(H + H_{\text{dip}}) + (H_{k_{\text{oop}}} - M_S)$
U_k	$\mu_0(M_S V H_{k_{\text{ip}}})/2$	$\mu_0(M_S V(H_{k_{\text{oop}}} - M_S))/2$
$\lvert I_{sw}\rvert$	$\frac{2e}{\hbar}\frac{2\alpha}{g(\vartheta)p}\left(U_k + \frac{1}{2}\mu_0 M_S^2 V\right)$	$\frac{2e}{\hbar}\frac{2\alpha}{g(\vartheta)p}U_k$

Table 7.1: Comparison between the effective magnetic field ($H_{\text{eff}}^{P\to AP}$, $H_{\text{eff}}^{AP\to P}$), the energy barrier between the two stable magnetic states (U_k) and the switching current (I_{sw}) of spin valves with in-plane (i.e. anisotropy field in-plane $H_{k_{\text{ip}}}$) and out of plane anisotropy (i.e. anisotropy field perpendicular $H_{k_{\text{oop}}}$). The sketch in Figure 7.1 shows 7.1(a) the in plane and 7.1(b) the out of plane cases.

height of the energy barrier between the parallel and the antiparallel states (U_k). For applications $U_k > 50$ kBT is required to ensure a 10 years stability. By controlling U_k and optimizing materials properties such as spin polarization and magnetic damping, the critical switching current can be reduced by more than one order of magnitude, while maintaining thermal stability.[42,68] Note that in perpendicular anisotropy structures with composite free layers it should be possible to further decrease the critical switching current while maintaining stability.[69]

In this chapter, we focus on nanopillar spin-valves with PMA, under the application of a magnetic field and an injected current by studying state diagrams. We first explain how to measure, plot and interpret such a state diagram. The following section focuses on the comparison with the experimental results. We present the influences of extrinsic and intrinsic parameters as lateral size of the sample, temperature, sweeping field rate, time measurement and field orientation. We then conclude that to explain our experimental results, the symmetry of the system must be broken. Consequently, we refine our modeling by considering a non-uniaxial symmetry. Finally, in chapter 8, some possible origins of the symmetry breaking as a misalignment of the magnetic field or the anisotropy field as well as the presence of a second order anisotropy constant are tested using numerical simulations.

7.1 Experimental State Diagram

The nanopillar spin-valve structures discussed here, are described in section 6.1, and have been reported in several papers before.[20,42,43,44,18,19]
Two types of resistance are measured: dc Resistance ($R_{dc} = V/I$) and ac resistance ($R_{ac} = dV/dI$). R_{dc} is measured by injecting a dc current (Idc) and measuring voltage with a nano-voltmeter in a four terminal configuration. In that case I_{dc} is used both to measure R_{dc} and to inject the current needed for spin transfer torque. The resistance dV/dI i.e the dV response to a small ac current oscillation dI measures R_{ac}[70] (see for instance Figure 7.2 and Figure 7.4). This is done using a lock-in technique. The two resistances are related as followed

$$R_{ac} = \frac{dV}{dI} = \frac{d(RI)}{dI} = R_{dc} + I\frac{dR}{dI} \tag{7.1}$$

As a consequence they are complementary since as soon as the resistance will be affected by the current reversibly as in the case of Joule heating or spin transfer torque effects the two resistances will differ. For instance, in the case of the onset of magnetization precession the resistance changes reversibly with current giving rise to a smooth R_{dc} variation and a peak in R_{ac}. The current is defined positive when the electrons flow from the reference layer to the free layer tending to align the two layers in the parallel state (P). The reference layer magnetization switches for an applied field close to 1 T. Since no fields greater than 0.5 T are applied during the measurements the reference layer is expected to be stable. For all the experiments shown here the reference layer magnetization is pinned along the positive field direction. As presented in previous studies[43] the dipolar stray field H_{dip} arising from the reference layer is acting on the free layer and affects the magnetization dynamic.

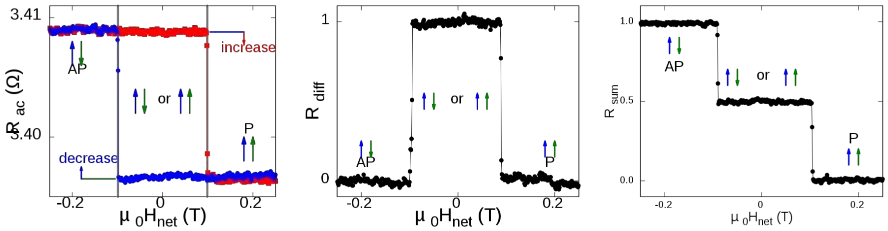

(a) Ac-resistance variation (b) Normalized difference (c) Normalized half-sum

Figure 7.2: Hysteresis loops

The experimental state diagrams are built by taking a series of field hysteresis loops for different injected currents (or are a series of current loops at different applied magnetic field). An example curve is shown in Figure 7.2 showing hysteretic switching of the free layer. Indeed, for one value of the injected current a field hysteresis loop divides the magnetic field axis into three regions of different magnetic configurations. In the middle, it is the bistable region where the spin-valve can be either in the parallel or antiparallel states. Going to the positive field, only the parallel configuration becomes available whereas going to the negative field, only the antiparallel configuration becomes available. The two borders between these three regions are marked by the switching fields (see Figure 7.2(a)). Therefore, a plot of the evolution of these switching fields as a function of the injected current gives a state diagram.

To build a state diagram, we make a two-dimensional plot of either $R_{\text{diff}}(H) = R_{\text{inc}}(H) - R_{\text{dec}}(H)$ or $R_{\text{sum}}(H) = [R_{\text{inc}}(H) + R_{\text{dec}}(H)]/2$ for different current values (see Figs. 7.2(b) and 7.2(c)) where $R_{\text{inc}}(H)$ and $R_{\text{dec}}(H)$ are the field increasing and decreasing branches of the hysteresis loop respectively (see Figure 7.2(a)). With these two methods, the state diagram is then obtained by building a two dimensional colored map in the $(H,\, I)$ parameter space where each point corresponds to a specific couple of current and field. Its color is given by the value of R_{diff} or R_{sum} at these coordinates (see Figure 7.3). Each of its lines corresponds to a unique value of the injected current and is determined from the field hysteresis loop measured at this current. The qualitative difference between R_{sum} and R_{diff} is that R_{diff} highlights the hysteretic regions of the state diagram, as non-hysteretic regions will be zero.

In order to compare the lines obtained for different injected currents, the parabolic evolution of the nanopillar resistance due to the Joule heating has to be taken into account. Using the treatment with R_{diff} this problem disappears because the giant magnetoresistance ratio is not affected by the Joule heating. On the contrary, using R_{sum}, this effect induces a vertical contrast that can complicate the reading of the state diagram. To remove this contribution, the resistance values of the concerned hysteresis curves need to be normalize using the following formula $R_{\text{norm}} = (R - R_P)/(R_{AP} - R_P)$. As a result, the normalized resistances of the parallel and of the antiparallel states are respectively 0 and 1 (see Figure 7.2(c)). Figure 7.3 presents the state diagram of a nanopillar spin-valve with

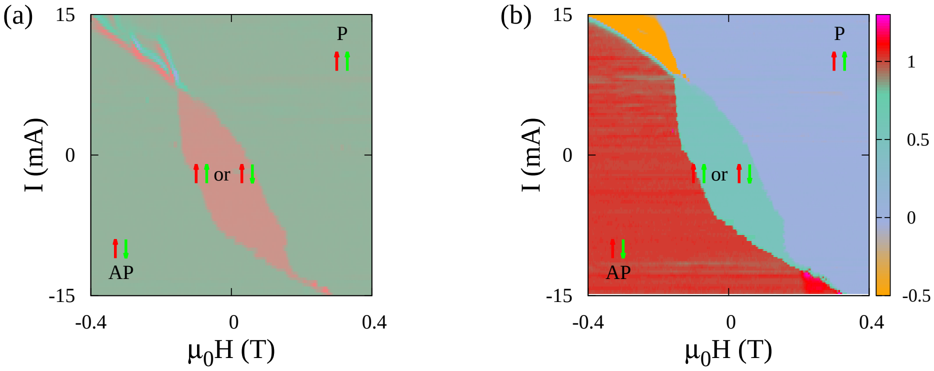

(a) difference of AC resistances

(b) half sum of AC resistances

Figure 7.3: State diagrams of an elliptical nanopillar spin valve of 50 nm by 300 nm with a hard layer made of [Co/Pt]/[Co/Ni] and a free layer made of [Co/Ni] with a platinum layer on top. The applied magnetic field step is of 1 mT and the injected current step is of 0.1 mA. Data acquired at a sample ambiant temperature unless otherwise specified.

perpendicular magnetizations similar to the previous ones where Figure 7.3(a) is R_{diff} and Figure 7.3(b) R_{sum}. These two state diagrams exhibit a similar behavior. However, R_{diff} highlights the bistable region whereas R_{sum} highlights the behavior of the nanopillar in the high field and current regions. These two treatments are therefore complementary.

Figure 7.4 shows the same state diagram as Figure 7.3(b) along with three characteristic hysteresis loops for three different injected currents values. These field hysteresis loops are horizontal cross-sections of the state diagram at the ordinate given by the value of the injected current. Similarly, a current hysteresis loop is a vertical cross-section of the state diagram at the abscissa given by the value of the applied magnetic field. The state diagram gathers the information given by field and current hysteresis loops. As mentioned previously, a state diagram is mainly divided into three regions: one for which the spin-valve is in the parallel state, one where it is in the antiparallel state and one where it can be in these two states, the bistable region. Because of our experimental conventions, the parallel state region is for the positive field and current (the blue region in Figure 7.4) whereas the antiparallel state region is for the negative field and current region (the red region in Figure 7.4). Between these two regions we find the bistable region (the green region in Figure 7.4). A field hysteresis loop crossing these three regions gives a curve such as the one represented for $I = 0$ mA. The switching fields are given by the left and right limits of the bistable region whereas the switching currents are given by the up and down limits of the bistable region. Furthermore, two additional regions appear if the current and the field are large enough. Going to the positive currents the width of the hysteresis loop shrinks because of the spin transfer efficiency difference

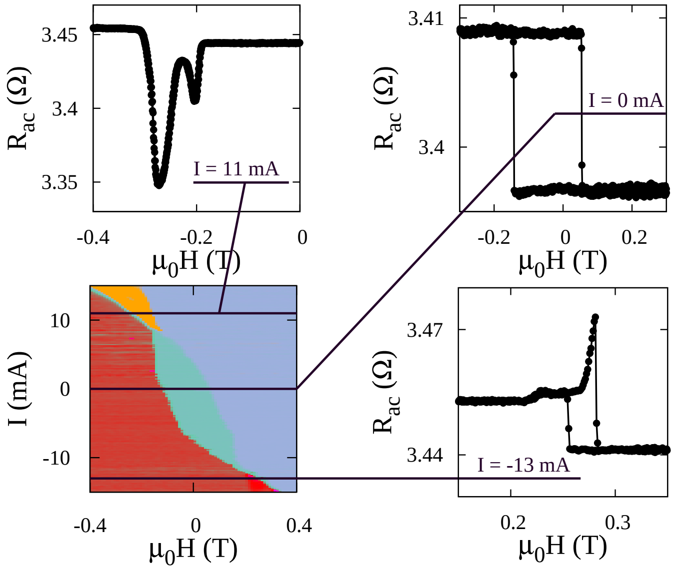

Figure 7.4: State diagram of an elliptical nanopillar spin valve of 50 nm by 300 nm with a hard layer made of [Co/Pt]/[Co/Ni] and a free layer made of [Co/Ni] obtained from the half sum method along with three characteristic hysteresis loops at $I = -13$ mA, $I = 0$ mA and $I = 11$ mA

between the parallel to antiparallel and the antiparallel to parallel transitions. Consequently, in the upper left corner corresponding to a high positive current and a high negative field, the hysteresis loop ends up disappearing. Instead of a hysteretic behavior, the spin-valve transitions reversibly between the parallel and the antiparallel state passing through similar magnetic states. This region is generally characterized by peaks in R_{ac}[44] as seen in the R_{ac} vs H curve at $I = 11$ mA in Figure 7.4. The width of these peaks appears in orange in the state diagram and they are shown to be the consequence of magnetization precessions.[45] These peaks should not appear in the state diagram obtained from the difference of resistances method because the increasing and the decreasing part of the hysteresis curve are reversible and, in principal, identical. Actually, their position between the increasing and the decreasing parts of the hysteresis are slightly shifted because of the field sweep procedure, so the difference of resistance gives a positive value at one side of the peak and a negative one on the other side. Consequently, the peaks appear as a couple of blue and red lines (see Figure 7.3(a)) more complicated to interpret than in the representation with the R_{sum} treatment.

In the opposite corner corresponding to a high negative current and a high positive field the hysteresis loop also shrinks and even, at times, disappears. Here, the AC resistance curves are often characterized by a mix of small hysteretic regions, peaks and shoulders like in the curve measured at $I = -13$ mA. The hysteretic part and the peak appear as a pink coloration inside the bistable region.

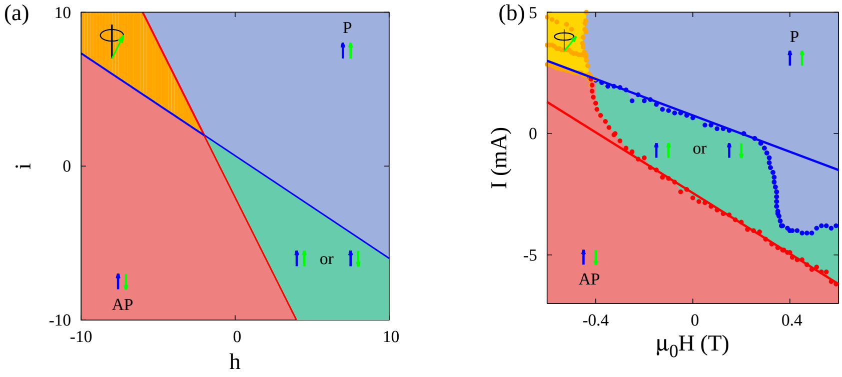

(a) Theoritical state diagram of a nanopillar spin valve with perpendicular magnetizations in the case of a uniaxial, macrospin and 0 K approach in reduced coordinates

(b) Experimental state diagram of a hexagonal nanopillar spin valve of 100 nm by 200 nm with a hard layer of [Co/Pt]/[Co/Ni] and a free layer made of [Co/Ni]. The blue and red cicles are for the measured switching fields and the orange circles indicate the presence of a peak in the differential resistance measurements. The blue and red lines present what could correspond to the expected evolution of the switching current as a function of the applied magnetic field of our simple modeling. The values of the parameters used can be found in [20]

Figure 7.5: State diagrams

Now that we have described the general shape of the experimental state diagrams of a nanopillar spin-valve with PMA, we will compare these results to modeled results.

7.2 Experimental Results vs Uniaxial Model

There are lots of similarities between the theoretical state diagram calculated in this uniaxial approach and the experimental state diagrams (see Figure 7.5). Both of them are composed of two borders dividing the (H, I) plane into the same four regions. At high positive field and current, the spin-valve is in the parallel state whereas at high negative field and current it is in the antiparallel state. At high positive field and negative current, it can be either parallel or antiparallel, this is the bistable region characterized by hysteresis loops. At high negative field and positive current it is neither parallel nor antiparallel. From the theoretical results, the field hysteresis loops has to shift toward the negative field when the current increases while its width shrinks. When the two borders cross, the hysteresis loops show a series of differential resistance peaks in the experimental state diagrams.

These peaks are compatible with the magnetization precessions predicted by the theory. Such precessions are commonly recorded in spin-valves with at least

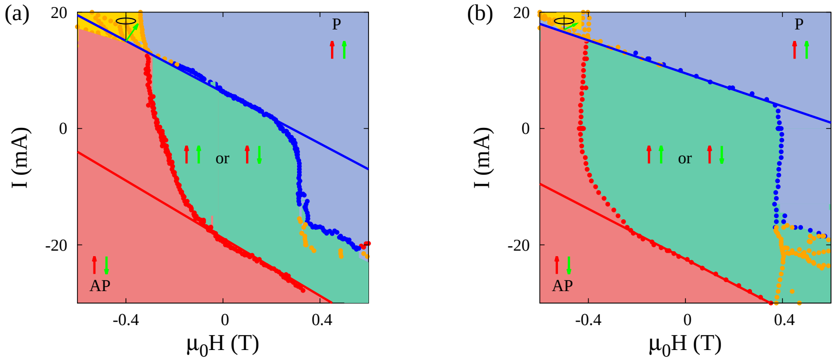

(a) T = 290 K (b) T = 20 K

Figure 7.6: Experimental state diagrams of an hexagonal nanopillar of 100 nm by 200 nm with a hard layer made of [Co/Pt]/[Co/Ni] and a free layer made of [Co/Ni]. The blue and red lines present what could correspond to the expected linear evolution of the switching current as a function of the applied magnetic field.

one magnetization in-plane because they generate an alternative voltage thanks to the angular dependence of the giant magnetoresistance. However, in these all perpendicular spin-valves, a uniform precession of the magnetization of the free layer around the out-of-plane axis does not affect the angle between the magnetizations of the free layer and of the polarizer. As a consequence, no alternative voltage can be generated in first approximation. These precessions have to be detected indirectly thanks to differential measurements and a lock-in technique. Unfortunately, these methods cannot guarantee that every measured peaks are the consequence of magnetization precessions. Note that another method using Giga-Hertz (GHz) Microwave irradiation has been developed to enhance and detect spin-torque driven magnetization precession in nanopillars with magnetic perpendicular anisotropy.[45]

The borders determined by the switching fields or currents evolve linearly in a large range of current an field however around the zero current switching fields a strong deviation from this linearity occurs. Experimentally it seems that the magnetization reversal becomes virtually independent of the injected current around these two fields and the current has to reach a critical value before the linear evolution appears. We can then define a threshold current usually named critical current in the following at which spin transfer torque affects the magnetization switching.[71,72] This observation seems in contradiction with the theoretical predictions since spin-transfer effect is expected to always modify the damping by increasing or decreasing the impact of the damping torque. The experimental state diagrams in this perpendicular geometry are actually much closer to the state diagrams in the planar geometry than expected (for instance [11, 73, 74, 41]).

The initial proposed model is based on a macrospin model with three main

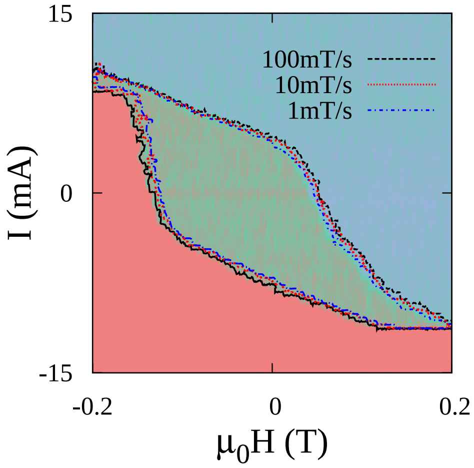

Figure 7.7: Experimental state diagram of an elliptical nanopillar spin valve of 50 nm by 300 nm with a hard layer made of [Co/Pt]/[Co/Ni] and a free layer made of [Co/Ni] for various sweeping rates of 100 mT/s (background and black line), 10 mT/s (red line) and 1 T/s (blue line)

hypotheses: there is no thermal activation, the hard and free layers can be modeled by a macrospin and the system is uniaxial. The influence of the hypotheses was tested by looking at the effect of various parameters on the state diagram: temperature (Figure 7.6), sweeping rate (Figure 7.7), time measurement (Figure 7.8), size (Figure 7.9) or field orientation (Figure 7.10).

In Figure 7.6, both temperatures (20 K and 300 K) exhibit regions around the zero current switching fields where the current influence on the reversal is weak. However, the absolute values of the critical currents seem to increase when the temperature decreases. The current influence is even weaker at low temperature, consequently, the origin of the critical currents is not the thermal activation. This conclusion is confirmed by numerical calculations of the state diagram of a nanopillar spin-valve with perpendicular magnetization by Zhu and Visscher.[46] In their modeling, they consider the same macrospin model but including temperature which is finite. In this case, they found a theoretical state diagram similar to the one presented in figure 7.6 with a linear evolution of the switching currents. Note that the change of the slope of the evolution of switching current between both temperatures remains unclear, but this behavior deviates from macrospin.

In Figure 7.7, we also could test on a different sample the influence of the sweeping rate. Note that it is another way to probe the effect of thermal activation.[75,76] Again a weak effect of thermal activation on the shape of the state

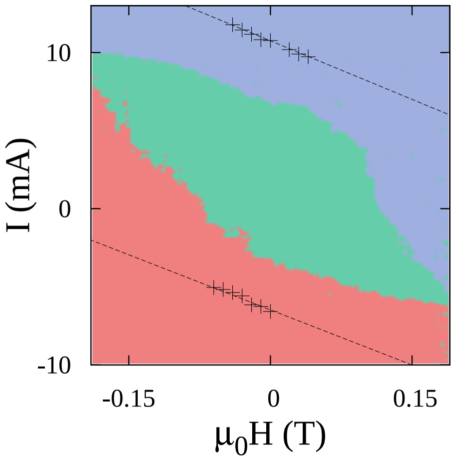

Figure 7.8: Experimental state diagram of a rectangular 100 nm by 100 nm spin valve with a hard layer made of [Co/Pt]/[Co/Ni] and a free layer made of [Co/Ni]. Blue and red correspond to the parallel and antiparallel states. The symbols (crosses) indicate the zero temperature switching current extrapolated from short-time measurements.[19] As this extrapolation eliminates the thermal excitations, the switching current is significantly larger than during the quasistatic measurement

diagram is observed.

A further approach to study the state diagram in the zero-temperature case is to reduce the measurement time. As it is not possible to directly record the phase diagram on the timescale of the magnetization dynamics, a different approach is needed. By determining the switching probability for short current pulses, it is possible to directly study the system on timescales from 100 ps upwards.[18] It is also possible to carry out measurements not only in the thermally excited regime, but also on a short-time regime, in which the switching process is only limited by the angular momentum transfer into the system.[19] For both the thermally as well as the ballistic regime the validity of the macrospin model has been studied and validated, by measuring the switching probabilities switching currents and their field dependence are directly accessible.

It is possible to eliminate the influence of thermal excitations by measuring the switching probabilities on sub-ns timescales and by extrapolating the LLG solution to infinite time, we can thus directly obtain the zero-temperature switching currents as a function of the applied magnetic field.[18]

Figure 7.8 shows the zero-temperature critical switching currents as a function of the applied magnetic field on top of the state diagram measured at room tem-

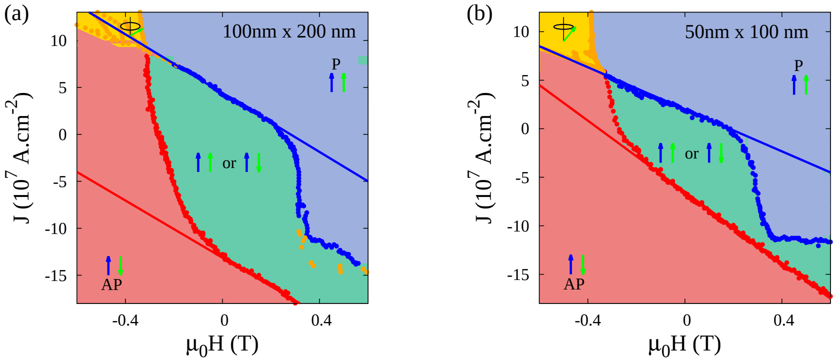

(a) 100 nm x 200 nm

(b) 50 nm x 100 nm

Figure 7.9: Experimental state diagrams of an hexagonal nanopillar spin valve with a hard layer made of [Co/Pt]/[Co/Ni] and a free layer made of [Co/Ni]. The blue and red lines present what could correspond to the expected evolution of the switching current as a function of the applied magnetic field of our simple modeling

perature. The boundary defined by the crosses is the limit the state diagram would expand to if it was measured at infinite speed and zero temperature, conversely the room temperature state diagram lies inside and at some distance to the zero-temperature lines. As expected the value of the switching current for short pulses is bigger than in the quasi-static case nevertheless a linear behavior between field and current is observed.

To test the impact of the macrospin approach on the experimental state diagram, Figure 7.9 compares the state diagrams obtained for two hexagonal nanopillar spin-valves with different sizes. Note that to compare two state diagrams measured on samples with different sizes, the state diagram are plotted with the current density ($J = I/S$ where S is the area of the nanopillar) instead of the current intensity. Smaller samples are closer to the macrospin approach because it is easier for the exchange interaction to dominate over the demagnetizing field. However, there is no clear evidence of behavior difference between Figure 7.9(a) and Figure 7.9(b). Here, the blue and red slopes can change from a pillar to another due to a slight change of the parameters values (M_S, α...) as well as the dipolar field.

As a result, it is not obvious that introducing a micromagnetic approach into the modeling of the spin-valve will reproduce a much better experimental state diagram. This conclusion is confirmed by the micromagnetic simulation presented in [20] where it is found a theoretical state diagram close from the analytical state diagram presented.

Nevertheless it is clear that non-uniform magnetization reversal plays an important role in the magnetization reversal processes. Indeed it was shown that the formation of domains and domain walls could be observed[77,78,79,80,81] and

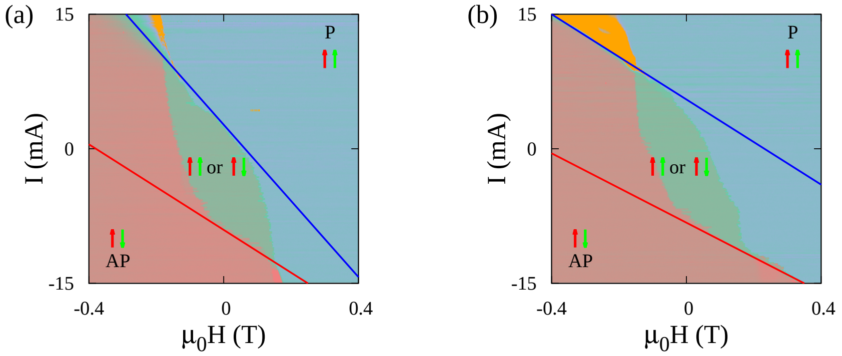

(a) 40°

(b) 0°

Figure 7.10: Experimental state diagrams of an elliptical nanopillar spin valve of 50 nm by 300 nm with a hard layer made of [Co/Pt]/[Co/Ni] and a free layer made of [Co/Ni]. The magnetic field is applied with an angle Ψ towards the perpendicular axis. The blue and red lines present what could correspond to the expected evolution of the switching current as a function of the applied magnetic field of our simple modeling.

that it was influencing the slow magnetization switching dynamics. It influences fast dynamics as well as [18, 45, 19, 82].

The last important hypothesis of our modeling is that all the contributions of the system are along the same axis. This is the uniaxial approximation. To test the impact of the symmetry on the experimental state diagrams, Figure 7.10 compares two experimental state diagrams measured on the same elliptical nanopillar spin-valve where the magnetic field is applied in two different directions. In Figure 7.10(a), it is applied at 40° from the perpendicular direction whereas in figure Figure 7.10(b) it is applied close to the perpendicular axis. When the magnetic field is applied away from the perpendicular direction, the effective field has a non-perpendicular component which breaks the uniaxial symmetry. In this case it seems that the field direction is affecting the state diagram.

This conclusion is confirmed by a study of the distortion of the Stoner Wohlfarth astroid by a spin polarized current of these nanopillar spin-valves.[72] Indeed, it shows that above a critical angle of application of the magnetic field, the injected current has no impact on the magnetization reversal. Therefore, one can state that the experimental state diagrams deviate from our modeling if the uniaxial symmetry is broken. In the following, we will try to refine our initial modeling by considering a non-uniaxial effective field exerted on the free layer due to the application of a magnetic field away from the perpendicular direction.

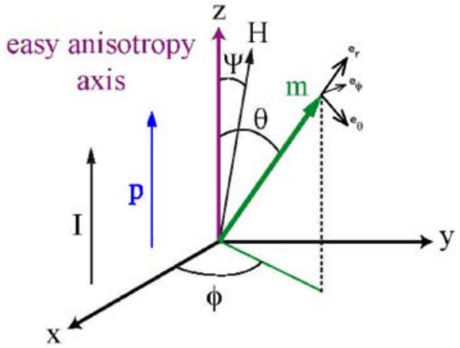

Figure 7.11: Orientation of the magnetization unit vectors **m** and **p**, applied field **H** and injected current I relative to the x, y, z axes in the case of a non-uniaxial symmetry

7.3 Non-uniaxial theoretical state diagram

In this non-uniaxial approach, we will use the same modeling as in section 3.7 page 48 except for the orientation of the applied magnetic field. Here, the field can be applied in the $y-z$ plane at an angle Ψ with the perpendicular direction with $\Psi \in]0,\pi]$ (see Figure 7.11).

We will then use equation (3.33) to obtain the equilibrium positions and equation (3.34) to study their stability. In order to perform the calculation analytically, we assume that the magnetization is close to the parallel or to the antiparallel configurations at the equilibrium. Even if these conditions are very restrictive, the following analysis shows that they nicely reproduce the behavior of our nanopillar. A more rigorous method of calculation developed by Bazaliy et al. can be found.[83] The general aspects of the theoretical state diagram obtained by these two methods are similar.

To calculate the evolution of the switching currents as a function of the applied magnetic field we need first to calculate the expression of the effective field in the framework of this non-uniaxial modeling. According to the description of the system, its magnetic energy is given by

$$E(\vartheta, H) = kV\sin^2\vartheta - \mu_0 M_S V \mathbf{m}\cdot\mathbf{H} \tag{7.2}$$

where V is the volume of the free layer. The effective field related to this magnetic energy is given in the basis ($\mathbf{e_x}$,$\mathbf{e_y}$,$\mathbf{e_z}$) by

$$\mathbf{H}_{\text{eff}} = (H\sin\Psi)\mathbf{e_y} + (H\cos\Psi + H_k\cos\vartheta)\mathbf{e_z} \tag{7.3}$$

The dipolar coupling and the demagnetizing field are not taken into account. In the basis ($\mathbf{e_x}$,$\mathbf{e_y}$,$\mathbf{e_z}$) we still have $\mathbf{m}\times\mathbf{p} = (\sin\vartheta\sin\phi)\mathbf{e_x} - (\sin\vartheta\cos\phi)\mathbf{e_y}$. As a result, the apparent effective field is given by

$$\mathbf{H}^*_{\text{eff}} = \frac{\beta I g(\vartheta)}{\gamma_0}[(\sin\vartheta\sin\phi)\mathbf{e_x} - (\sin\vartheta\cos\phi)\mathbf{e_y}] + (H\sin\Psi)\mathbf{e_y} + (H\cos\Psi + H_k\cos\vartheta)\mathbf{e_z} \tag{7.4}$$

Therefore, from equation (3.33) the equilibrium positions are the solutions of the following system

$$\begin{cases} (H\cos\Psi + H_k\cos\vartheta)\sin\vartheta = H\sin\Psi\cos\vartheta\sin\phi \\ \beta I g(\vartheta)\sin\vartheta = \gamma_0 H\sin\Psi\cos\phi \end{cases} \tag{7.5}$$

The stability of these equilibrium positions is determined by the criterion given by equation (3.34). Here, we have

$$\frac{d\mathbf{m}}{dt}\cdot\mathbf{e}_\vartheta = -\left[\alpha\gamma_0(H\cos\Psi + H_k\cos\vartheta) + \frac{\beta I g(\vartheta)}{\gamma_0}\right]\sin\vartheta + \alpha\gamma_0 H\sin\Psi\cos\vartheta\sin\phi + H\sin\Psi\cos\phi \tag{7.6}$$

With the assumption that the movement of the magnetization along the $\mathbf{e}_\phi$ direction is negligible from the reversal point of view, the stability criterion in this non-uniaxial modeling becomes

$$[(h\cos\Psi + g(\vartheta)i)\cos\vartheta + h\sin\Psi\sin\vartheta\sin\phi + \cos 2\vartheta]_{\vartheta=\vartheta_{\mathrm{eq}},\phi=\phi_{\mathrm{eq}}} \geq 0 \tag{7.7}$$

The ϑ dependence of the $g(\vartheta)$ function will not be taken into account during the derivation. To solve analytically these equations we will consider by analogy with the previous modeling that the magnetization can be into two opposite magnetization configurations: one close to the parallel state where $\vartheta \approx 0$ and $\phi \approx \frac{\pi}{2}$ and one close to the antiparallel state where $\vartheta \approx \pi$ and $\phi \approx -\frac{\pi}{2}$. As a result, the movement of the magnetization along the $\mathbf{e}_\phi$ direction is indeed negligible from the reversal point of view.

If we consider the case of a parallel to antiparallel switching ($\vartheta = 0$ and $\phi = \frac{\pi}{2}$) and in first order approximation the set of equations (7.5) gives the following coordinates for the equilibrium position

$$\vartheta_{\mathrm{eq}} = \frac{h\sin\Psi}{h\cos\Psi + 1} \tag{7.8}$$

$$\phi_{\mathrm{eq}} = \frac{\pi}{2} - \frac{\alpha g(\vartheta)i}{h\cos\Psi + 1} \tag{7.9}$$

Here, contrary to the purely uniaxial case, the position of the magnetization of the free layer at the equilibrium evolves as a function of the applied magnetic field. Moreover, it is not contained in the $y - z$ plane because of the action of the spin transfer torque.

In first order approximation and injecting the ϑ_{eq} value of the equilibrium position of equation (7.8), the stability criterion given by (7.7) becomes for the parallel magnetic configuration

$$h^2 + [(g(0)i + 2)\cos\Psi]h + g(0)i + 1 \geq 0 \tag{7.10}$$

Therefore, in this non-uniaxial modeling, the region of the $(H,\, I)$ plane where the parallel magnetic configuration is stable is given by the following expression of the switching current as a function of the applied magnetic field

$$i \geq -\frac{h^2 + 2h\cos\Psi + 1}{g(0)(h\cos\Psi + 1)} \tag{7.11}$$

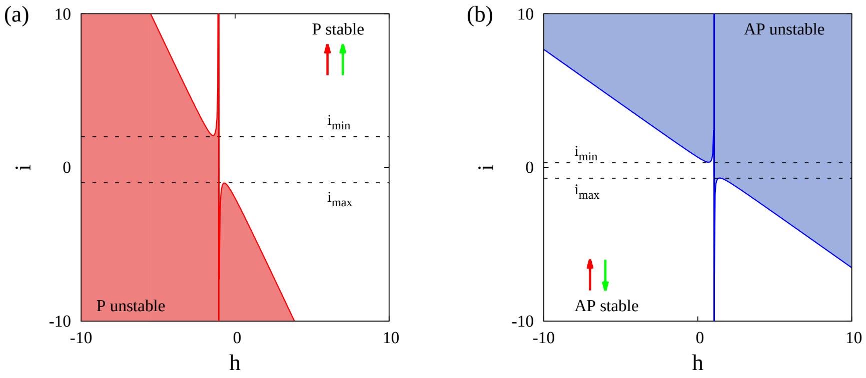

(a) Parallel state (b) Antiparallel state

Figure 7.12: Stability diagrams in the applied magnetic field and injected current plane in reduced coordinates. The colored areas correspond to the unstable regions and the lines to the theoritical evolution of the switching currents with the applied magnetic field.

In the non-uniaxial case ($\Psi \neq 0$), the evolution of the switching current is represented on Figure 7.12 (called here stability diagram). A vertical asymptote at $h = -1/\cos\Psi$ divides the curve into two branches. If $h < -1/\cos\Psi$, the switching current decreases with the applied magnetic field until it reaches a minimum value at $h = -\frac{1+\sin\Psi}{\cos\Psi}$. If $h > -1/\cos\Psi$, the switching current increases with the applied magnetic field until it reaches a maximum value $h = -\frac{1-\sin\Psi}{\cos\Psi}$. The expressions of this local minimum and of this local maximum of the switching current are respectively given by

$$i^P_{min} = \frac{2}{g(0)}\frac{\sin^2\Psi + \sin\Psi}{\cos^2\Psi} \tag{7.12}$$

$$i^P_{max} = \frac{2}{g(0)}\frac{\sin^2\Psi - \sin\Psi}{\cos^2\Psi} \tag{7.13}$$

When the injected current ranges between these two values, the stability diagram of the parallel magnetic configuration shows that the parallel state becomes unstable for a constant applied magnetic field $h = -1/\cos\Psi$ (see Figure 7.12(a)). Therefore, in this region the spin-transfer torque does not affect the stability of the parallel state. It has to reach the i^P_{min} or i^P_{max} value depending on its sign to have an impact on the parallel to antiparallel reversal. These values correspond to the critical currents highlighted in the experimental state diagrams. Outside these critical currents, the evolution of the switching currents tends to be linear and close the evolution predicted by the uniaxial model.

Similarly for the antiparallel to parallel switching ($\vartheta \approx \pi$ and $\phi \approx -\frac{\pi}{2}$), in the non-uniaxial case ($\Psi \neq 0$):

$$i \leq \frac{h^2 - 2h\cos\Psi + 1}{g(\pi)(h\cos\Psi - 1)} \tag{7.14}$$

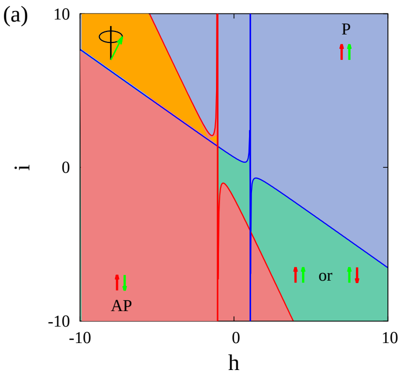

(a) Theoritical state diagram of a nanopillar spin valve with perpendicular magnetization in the case of a non-uniaxial ($\Psi = 20°$), macrospin and 0 K approach

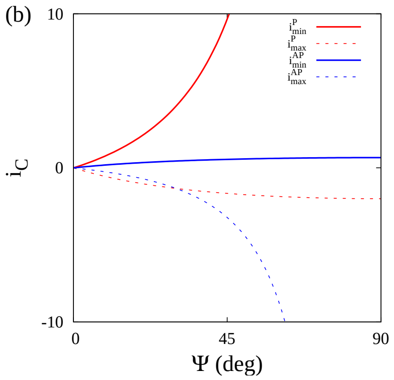

(b) Theoritical evolution of the critical currents as a function of the angle of the application of the magnetic field

and

$$i_{min}^{AP} = -\frac{2}{g(\pi)} \frac{\sin^2 \Psi + \sin \Psi}{\cos^2 \Psi} \tag{7.15}$$

$$i_{max}^{AP} = -\frac{2}{g(\pi)} \frac{\sin^2 \Psi - \sin \Psi}{\cos^2 \Psi} \tag{7.16}$$

The evolution of the switching current as a function of h is then represented on Figure 7.12(b) and is very similar to the parallel to antiparallel switching.

The theoretical determination of the switching currents given by equations (7.11) and (7.14) allows to draw a theoretical state diagram of a nanopillar spin-valve with perpendicular magnetizations in this non-uniaxial approach. Figure 7.13(a) presents the theoretical state diagram obtained in this non-uniaxial approach. Contrary to the uniaxial modeling where the evolution of the switching current is always linear (see Figure 7.5(a)), in this modeling the quasi-linear evolution of the switching current is broken between critical current values (see Figure 7.13(b)). Between these critical currents, the reversal of the magnetization does not depend on the injected current anymore. Indeed, the switching field remains constant at its value when there is no injected current. This non-uniaxial modeling gives a closer description of the experimental observations (see Figure 7.5(b)).

Therefore, it seems that the breaking of the uniaxial symmetry of the spin-valve with perpendicular magnetizations is the key parameter to understand the shape of the state diagrams in this system. In the next section, we shall search for the experimental reason that can justify such a break in the uniaxial symmetry.

Chapitre 8

Effet des différents paramètres

The origin of the non-uniaxiality can either be extrinsic as a misaligned magnetic field or intrinsic as a deviation of the free layer easy axis. Those two hypotheses have been tested by computing the LLGS equation (3.23).

The state diagrams are computed in the macrospin approximation at zero-temperature. The calculations are done taking into account the average dipolar fields resulting from a spin-valve structure with two magnetic layers having a 50 nm x 100 nm rectangular shape of 50 nm. The parameters are the ones given in section (6.1) 79. The hard layer magnetization is supposed fixed along the z axis (see Figure 3.11).

The theoretical state diagram calculated in the uniaxial case is shown on Figure 8.1. This simulated state diagram resembles to the theoretical one (see Figure 7.5(a)) calculated with the analytical model in the uniaxial approach.

Figure 8.2 exhibits two simulated state diagrams where the magnetic field is tilted with an angle from the perpendicular direction (see Figure 7.11). A critical current i.e. the deviation to the linearity of the switching current appears clearly for a tilted angle of $\Psi = 5°$(see Figure 8.2(a)). The values of the critical currents extend increases when the tilted angle increases (see Figure 8.2(b) for $\Psi = 20°$).

The influence of the misaligned easy anisotropy axis defined by Ψ_{ani} the angle between the easy axis anisotropy and the perpendicular direction is shown on Figure 8.3. For $\Psi_{ani} \neq 0$, the state diagram exhibits a part where the reversal of the magnetization does not depend on the current. The presence of a critical current is similar to the previous simulations with a tilted magnetic field (Figure 8.2). However, the influence of the anisotropy angle is much stronger than the applied magnetic field. So a slight misalignment of the anisotropy axis has a greater influence than the magnetic field on the magnetization reversal.

Finally we considered the effect of a second ordered anisotropy constant value

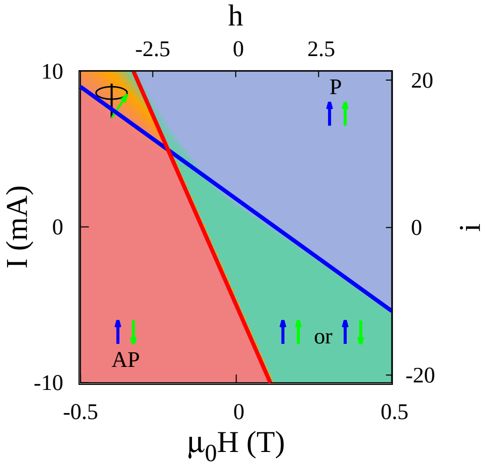

Figure 8.1: Theoritical state diagram for a uniaxial system calculated using numeric simulations. The new reduced coordinates $h = H/H_k$ (bottom) and $i = \frac{\beta I}{\alpha\gamma_0 H_k}$ (right) have been added using the new parameters (see text)

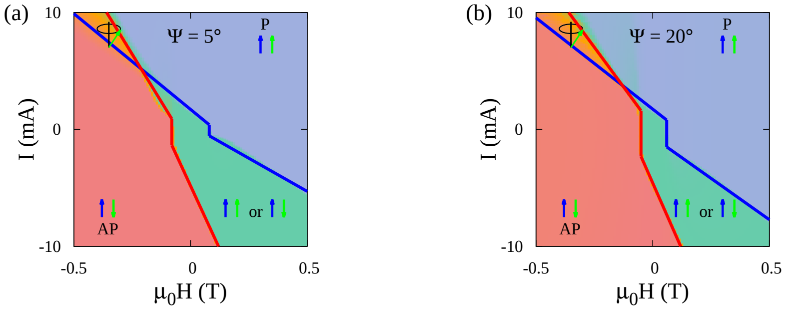

(a) 5° (b) 20°

Figure 8.2: Theoritical state diagrams in a case of a tilted applied field

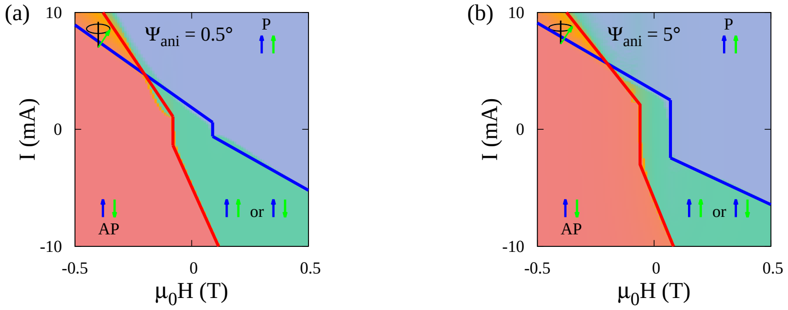

(a) 0.5°

(b) 5°

Figure 8.3: Theoritical state diagrams in a case of a tilted anisotropy field

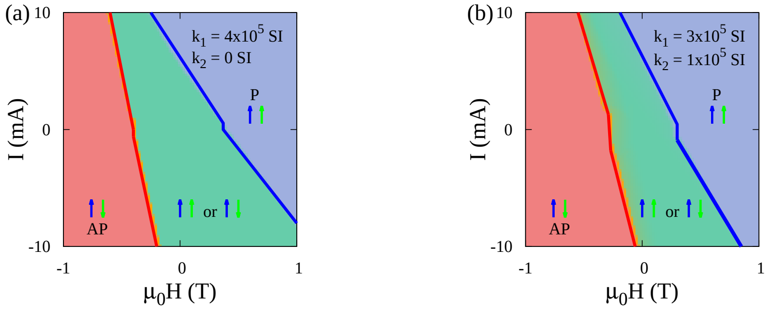

(a) $k_1 = 4 \cdot 10^5$ J/m^3 $k_2 = 0$

(b) $k_1 = 3 \cdot 10^5$ J/m^3 $k_2 = 10^5$ J/m^3

Figure 8.4: Theoritical state diagrams in the case with an added in plane $k_P = 10^4$ J/m^3 and second order anisotropy constant k_2. The value of the total anisotropy constant k is chosen to be the same in both cases.

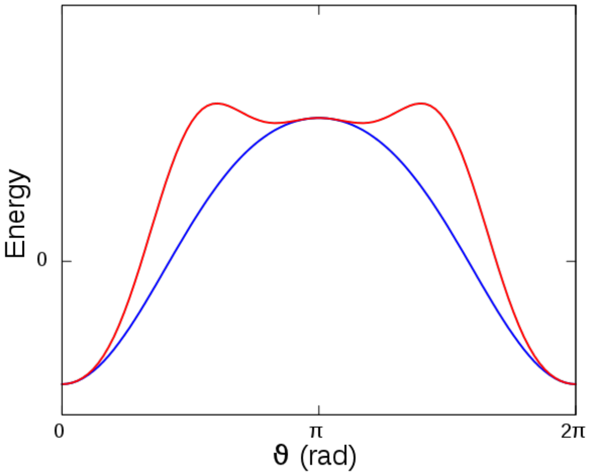

Figure 8.5: Energy landscape of the free layer as a function of the angle ϑ, for an applied field of 200 mT and without injected current. The parameters used here are $k_P = 10^4$ J/m^3, $k_1 = 3\cot 10^5$ J/m^3. The blue curve is plotted for $k_2 = 0$, the red one for $k_2 = 10^5$ J/m^3.

k_2. We assumed a sample with a weak in-plane anisotropy component k_P corresponding to the in-plane shape anisotropy. The presence of k_P induced a weak breaking on the uniaxial symmetry. Figure 8.4 compares two computed states diagrams without (Figure 8.4(a)) and with taking into account k_2 (Figure 8.4(b)). The value of $k_2 = 10^5$ J/m^3 is chosen to be one third of k. We notice an increase of the critical current due to k_2. For Figures 8.4(a) and 8.4(b), the anisotropy constants sum $(k_1 + k_2)$ is kept constant.

An energetic analysis of the system is required to explain this behavior. The expression of the magnetic energy of the system is given by

$$E(\vartheta, H) = k_1 V \sin^2\vartheta + k_2 V \sin^4\vartheta + k_p V \cos^2\vartheta - \frac{1}{2}\mu_0 M_S V \sin^2\vartheta - \mu_0 M_S V H \cos\vartheta \tag{8.1}$$

where ϑ is the angle between the perpendicular axis and the magnetization of the free layer. The first 3 terms in equation (8.1) are related to the first-order, second-order and in plane anisotropy contribution respectively, the fourth and the fifth terms are respectively the demagnetizing and the Zeeman energy. Using equation (8.1), we can calculate the energy landscape of the system as a function of ϑ (Figure 8.5). The investigation of the equilibrium positions, at the extremum of energy, gives us the static or dynamic configuration of the system respectively.[71] In Figure 8.5, we observe for the curve with $k_2 = 10^5$ J/m^3 (red curve), for an applied field of 200 mT close to the H_k value, the presence of one potential well at $\vartheta = 0$ (the parallel state) and two other stable states close to $\vartheta = \pi$. As a result, other stable states are now available. Since those two new states are not aligned with the anisotropy axis, it leads to a symmetry breaking.

We have then demonstrated that several factors lead to a symmetry breaking that can explain the experimental state diagram. Since it is unlikely that for all experiments the applied field is strongly misaligned we then suspect that the magnetocristalline anisotropy plays an important role. Indeed a misalignment of the anisotropy axis with the current flow is probable. An experimental study on an epitaxial crystalline [Co/Ni] system with well definite anisotropy axis[81] allows us to conclude. Moreover because of the presence of grains in the sputtered sample one can expect a distribution of anisotropy axis for each nanopillar. Finally since a pure hexagonal Co shows at RT a second-order anisotropy constant value k_2 ($1.44 \cdot 10^5$ J/m^3) close to first-order one k_1 ($4.53 \cdot 10^5$ J/m^3),[?] Co-based alloys as [Co/Ni] and [Co/Pt] layers are expected to exhibit a similar behavior. It is then likely that the materials used have strong second-order anisotropy constant that enhance the symmetry breaking which is responsible for the measured experimental state diagram. Note that theses materials with a strong k_2 are also of great interest in magnetic recording media since more thermal stability can be achieved.[84,85] In the future it is then of great interest to continue the characterization and the study of the origin of perpendicular magnetic anisotropy in thin film and multilayers.[86,87,88]

In conclusion, we have studied the magnetic state of nanopillar spin-valves with strong perpendicular anisotropy. We showed that the magnetic states of the layers depend on the applied magnetic field and the DC current injected to the device and that consequently maping the magnetic states of the system on a comprehensive state diagram is very convenient. The method to build and to interpret the experimental state diagram is explained. The influence of several parameters such as lateral size of the sample, temperature, sweeping field rate, time measurement and field orientation on experimental state diagrams is presented. Analytically the state diagram in a purely uniaxial system is modeled and it is demonstrated that this simple model does not properly reflect the experimental results. It is shown that if the uniaxial symmetry is broken a region for which the current has no effect on the switching can be evidenced as observed experimentally. We finally discussed the possible origins of the symmetry break using an analytical model and numerical simulations. A misalignment of the applied field, anisotropy axis or the presence of strong second order anisotropy constant could explain the experimental results. Future experimental studies are needed to determine the microscopic origin(s) of the symmetry breaking. The complete study conducted here is crucial to describe model systems for spin transfer torque in scope to develop devices for spintronic applications as STT-MRAM. But such as devices require a reproducibility of the switching current and the angular distribution of the anisotropy axis from one grain to the other can be detrimental. In this way, studies on epitaxial crystalline with well controlled PMA are in progress.

Chapitre 9

État de précession

It is now well established that magnetization switching or precession can be induced by spin polarized injected current due to the spin transfer torque effect. For a small or moderate injected current, hysteretic magnetization switching can take place. For certain combinations of current and magnetic field, the STT may balance the damping torque and give rise to steady magnetization precession in the gigahertz frequency regime.[6,56] Furthermore, other magnetic states and dynamics have also been identified such as fluctuations,[9] canted states,[20] and domains states.[77]

The most common experiments for characterizing the dynamical magnetic states consist in recording the differential resistance dV/dI, i.e., detecting the ac voltage response to a small alternating current with a frequency (e.g. 1kHz) much lower than the magnetization precession.[9,8,56,20,77,89,42,72] The differential resistance can be written as

$$\frac{dV}{dI} = R + I\frac{dR}{dI} \tag{9.1}$$

The first term is the dc resistance which directly probes the magnetoresistance (MR) effect. The second term probes the reversible processes such as steady magnetization precession, leading to reversible changes in resistance as a function of current.

Besides the polarized current, magnetization dynamics are also influenced by the magnetic field and temperature. For instance in the case of steady state precession, the magnetization angle can be modified by an ac magnetic field or alternative temperature,[90,91,92] which are still under discussion.[70] Here we addressed the voltage response to an ac magnetic field perturbation. To probe the magnetic ac-susceptibility, we measured dV/dH given by

$$\frac{dV}{dH} = I\frac{dR}{dH} + R\frac{dI}{dH} \tag{9.2}$$

The first term is related to the reversible magnetic processes induced by the magnetic field and the second term results from the ac current induced by the ac magnetic field. It should be noted that in the case of low frequency excitation, the voltage response to reversible magnetic process is in-phase with the ac magnetic field excitation. However, the current variation in response to the ac-magnetic field is an inductive phenomenon leading to an out-of-phase response, i.e., a 90° phase shift. This phase property allowed us to distinguish the two terms.

In this chapter, we report a comparative study on the spin-transfer-driven magnetization reversal and dynamics in a nanopillar spin valve with perpendicular magnetic anisotropy using R, dV/dI, and dV/dH measurements. Both voltage responses to an ac magnetic field parallel ($dV/dH_{//}$) and perpendicular ($dV/dH_{\perp}$) to the dc magnetic field were measured. Dips or peaks in dV/dI, $dV/dH_{//}$, and $dV/dH_{\perp}$ exhibit distinct features where some magnetic states are revealed by $dV/dH_{//}$ and $dV/dH_{\perp}$ while being almost absent in the dV/dI signal.

The spin valve studied here, as reported earlier, consists in a Pt(3 nm)/[Co(0.25 nm)/Pt(0.52 nm)]$_4$/Co(0.25 nm)/[Ni(0.6 nm)/Co(0.1 nm)]$_2$ reference layer and a [Co(0.1 nm)/Ni(0.6 nm)]$_2$/Co(0.2 nm)/Pt(3 nm) free layer spaced by a 4 nm Cu layer. A Ta(5 nm)/Cu(30 nm) film acts as the bottom lead and a Cu(20 nm)/Ta(5 nm) film connects the top of the pillar to an Au top lead. Both the reference and the free layer are PMA. The multilayer was then patterned to a 50 x 200 nm^2 ellipse.

The transport measurements were performed at room temperature. A dc magnetic field H_{dc} up to 1.5 T was applied perpendicular to the film plane. The dc current I_{dc} was injected from a current source and the dc voltage V_{dc} was measured with a nanovoltmeter, allowing us to determine the resistance $R = V_{dc}/I_{dc}$. The positive current is defined as the one flowing from the free layer to the reference layer. To measure dV/dI, a 50 μA current at a frequency $f = 1$ kHz was applied and the generated voltage at the same frequency was measured with a lock-in amplifier. To probe $dV/dH_{//}$ and $dV/dH_{\perp}$, a 40 Oe magnetic field at $f = 10$ Hz was generated by a pair of Helmholtz coils either parallel (P) or perpendicular to the dc magnetic field, respectively. The resulting ac voltage responses at the same frequency were probed by the lock-in amplifier and only the in-phase voltage responses were considered to define $dV/dH_{//}$ and $dV/dH_{\perp}$. Most of the measurements focus on large negative field and large positive current region where free layer precession is expected.[56]

Figure 9.1 shows a series of the typical curves of R, dV/dI, $dV/dH_{//}$, and $dV/dH_{\perp}$ as a function of H_{dc} for various I_{dc}. Initially, the spin valve was saturated in a positive magnetic field to set the magnetization of the free layer P to that of the reference layer resulting in a low resistance R_P. The dc magnetic field was swept down to -5 kOe, where the magnetization of the free layer is antiparallel (AP) to that of the reference layer, leading to a high resistance R_{AP}, and then swept back to 1 kOe, where the configuration is back to P. For $I_{dc} = 4$ mA (corresponding the current density $J \simeq 4 \cdot 10^7$ A/cm^2), shown in Figures (9.1(a)-(d)) along the magnetic field descending branch, R jumps sharply from R_P to R_{AP} at $H_{dc} = -1.6$ kOe, and falls to R_P at $H_{dc} = -0.99$ kOe for the ascending branch. This measurement shows the hysteretic switching of the free layer magnetization between P and AP configuration. The dV/dI versus H_{dc} curves display similar hysteresis loops due to the absence of reversible magnetic

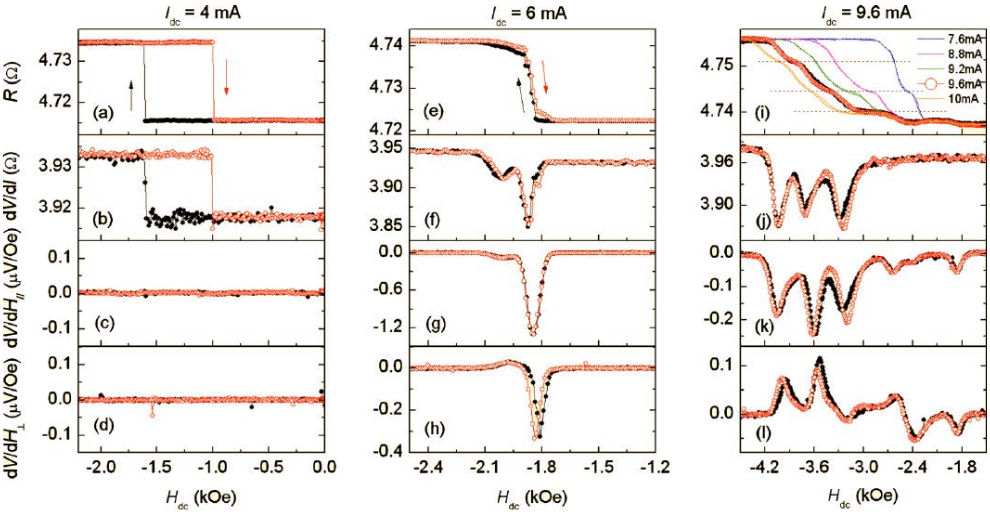

Figure 9.1: A series of the typical curves of R, dV/dI, $dV/dH_{//}$, and $dV/dH_{\perp}$ as a function of H_{dc} for various I_{dc}. [(a)-(d)] $I_{dc} = 4$ mA. [(e)-(h)] $I_{dc} = 6$ mA. [(i)-(l)] $I_{dc} = 9.6$ mA. The curves with black solid circles refer to the magnetic field descending branches and those with red open circles stand for the magnetic field ascending branches. The R as a function of H_{dc} for various I_{dc} between 7.2 and 10 mA are also shown in (i).

process induced by the current, i.e., here only the R term remains in equation (9.1). The H_{dc} dependences of both $dV/dH_{//}$ and $dV/dH_{\perp}$ show only a flat baseline meaning that almost no reversible magnetic process is induced by the magnetic field.

For $I_{dc} = 6$ mA, shown in Figures (9.1(e)-(h)) no obvious hysteresis is observed. R changes rapidly for the H_{dc} between -1.80 and -1.87 kOe but slowly between -1.87 and -2.10 kOe. dV/dI measurements show a large dip at $H_{dc} = -1.87$ kOe and a small one at $H_{dc} = -2.01$ kOe related to reversible magnetic processes. The $dV/dH_{//}$ signal shows negative peaks similar to dV/dI. The $dV/dH_{\perp}$ however shows both negative and positive peaks.

For $I_{dc} = 9.6$ mA, shown in Figures (9.1(i)-(l)), there are more dips or peaks in dV/dI, $dV/dH_{//}$, and $dV/dH_{\perp}$ in a wide H_{dc} range, corresponding to the different jumps in R.[20] The amplitude of these peaks are different for dV/dI, $dV/dH_{//}$ and $dV/dH_{\perp}$ showing the different influence of current and magnetic field on the magnetization dynamics. It is interesting that $dV/dH_{//}$ and $dV/dH_{\perp}$ exhibit some small peaks for the H_{dc} between -1.66 and -2.83 kOe corresponding to the undulation in R, while they are not visible in dV/dI.

The R as a function H_{dc} for various I_{dc} between 7.2 and 10 mA are also plotted in Fig 9.1(i). It can be seen that the curves are reversible but also show plateaus that are separated by similar giant magnetoresistance steps. Assuming these intermediate resistance plateaus represent precession states, these results would tend to show that magnetization prefers to process with particular angles. Indeed the spin valve GMR value depends on the relative angle between the free layer moments and the reference layer that is out of the film plane. In this case the precession angle can be roughly calculated from $\cos\varphi = 1 - 2[R(\varphi) - R_P]/(R_{AP} - R_P)$.[93] The reasons of those particular angles are not known and could be due to particular aspect of the nanopillar shape as the details of these steps varies from sample to sample. An alternate interpretation could be in terms of incoherent precession (spin waves).

Nevertheless those steps and plateaus give rise to dips or peaks in dV/dI and dV/dH measurements. It should be noted that different features in the dips or peaks for dV/dI, $dV/dH_{//}$, and $dV/dH_\perp$ indicate the influences of current and magnetic field on the magnetization precession. The magnetization dynamics results from the competition between the torque due to the magnetic field, the damping and the spin torque. In a macrospin approach magnetization precession appears when the spin torque balances the damping, a change in H_{dc} or I_{dc} will then change the angle of the magnetization precession and thus a variation in the resistance. The different signals coming from those measurements can be more clearly shown in the $(H_{dc}$,$I_{dc})$ state diagrams.

Figures (9.2(a)) and (9.2(b)) show the $(H_{dc}$,$I_{dc})$ state diagrams for dV/dI

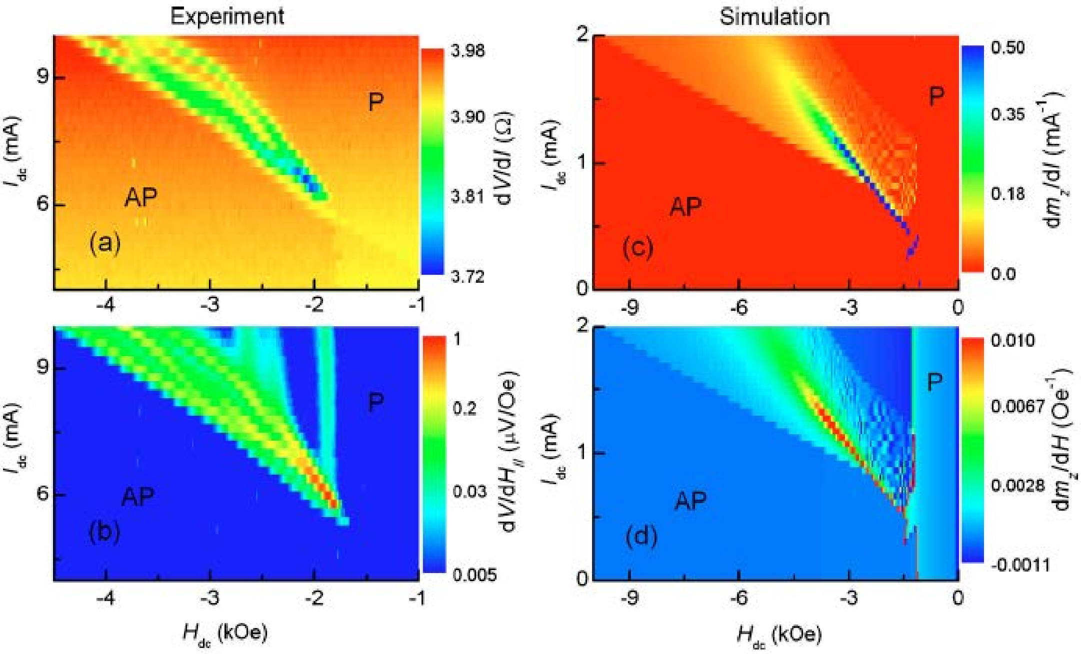

Figure 9.2: [(a) and (b)] The $(H_{dc}$, $I_{dc})$ state diagrams for the average values of dV/dI and $dV/dH_{//}$ measured by sweeping the applied dc magnetic field between 1 and -5 kOe. [(c) and (d)] The $(H_{dc}$, $I_{dc})$ state diagrams for dm_z/dI and $dm_z/dH_{//}$ from the macrospin simulation in the case of the anisotropy field tilted by 5°. The regions of the P and AP states are labeled.

and $dV/dH_{//}$. The STT-driven precession takes place when $I_{dc} > 5.6$ mA and $H_{dc} <$ -1.9 kOe. The state diagrams for dV/dI and $dV/dH_{//}$ show similar branches which indicate the transition between one steady precession and another. However those transitions are more or less pronounced depending on the kind of excitation. One key difference is the presence of a vertical line around -1.8 kOe in the $dV/dH_{//}$ state diagram but absent in the dV/dI one. It shows that the state that may be probed with dV/dH only is affected by the magnetic field and not the current which highlights the fact that these three techniques are complementary. For a better understanding we performed macrospin simulations similar to the one reported in [72] to compare to the experimental data. Similar parameters were used and the anisotropy axis was by 5° away from the normal of the film plane. Considering that the voltage changes come from GMR effect only and assuming that the hard layer is solidly fixed along the easy axis then the voltage V is proportional to the magnetization component along the easy axis that will be referred as m_z. As shown in Figures (9.2(c)) and (9.2(d)) the vertical branch appears in the $dm_z/dH_{//}$ state diagram but cannot be seen in the dm_z/dI diagram. The magnetic state related to this effect is a canted state which is a static state for which the magnetization is tilted away from the easy axis.

From this simple macrospin calculation, the plateaus in R versus H_{dc} and the branches in the precession region of the dV/dI phase diagram cannot be explained. These may show the limit of the macrospin model and suggest the presence of nonuniform magnetic configurations.

In summary, we studied STT-driven magnetization dynamics in a nanopillar spin valve with PMA using R, dV/dI, $dV/dH_{//}$, and $dV/dH_{\perp}$ measurements, respectively. R and dV/dI can give the information on hysteretic magnetization switching, and dV/dI, $dV/dH_{//}$, and $dV/dH_{\perp}$ can probe reversible magnetization processes. Both the amplitude and the sign of the peaks in dV/dI, $dV/dH_{//}$, and $dV/dH_{\perp}$ show the different influence of current and magnetic field on the magnetization dynamics. The three methods are complementary and offer new ways to study the different magnetic states and their dynamic. More precisely it is shown that canted states can be easily detected using dV/dH whereas it is nearly undetectable using dV/dI. It should be noted that these low cost and feasible methods are not limited to perpendicular magnetization systems nor to STT devices but it can be used to probe any magnetic state which lead to a MR effect.

Quatrième partie

Dynamique rapide

Résumé

Dans cette partie, nous allons étudier la dynamique d'aimantation à temps courts, c'est-à-dire de l'ordre de la nanoseconde en nous reposant sur le modèle de Sun décrit dans la partie 4.2 page 54. Jonathan Sun a en effet montré qu'à temps courts, le temps de renversement d'aimantation τ est régi par la conservation du moment cinétique total et il est donné par

$$\frac{1}{\tau} = A(I_C - I_{C_0})$$

où I_C est le courant nécessaire pour retourner l'aimantation, I_{C_0} est le courant critique à température nulle et A est le paramètre caractérisant la relation entre les charges et le transfert de moment cinétique de spin. En réécrivant l'équation précédente, il est facile de voir que le paramètre A est composé de deux termes décrivant d'une part le moment cinétique de spin et d'autre part, la quantité minimale nécessaire afin de contrer l'amortissement du système. Comme le moment cinétique total doit être conservé, A doit rester constant.

Afin de vérifier le modèle de Sun, des expériences ont été réalisées par Bedau et al.[18] Le comportement d'une vanne de spin a été étudié en y injectant des pulses de courant. Le procédé expérimental comprend quatre étapes. La vanne est tout d'abord saturée dans un état parallèle ou antiparallèle, on applique un champ magnétique puis on injecte un pulse de courant avec une durée et une amplitude déterminées. Après injection du pulse, on vérifie s'il y a eu retournement de la couche libre. Si tel est le cas, on recommence le processus. Sinon, on injecte de nouveau un courant. La probabilité de retournement est alors simplement déterminée en divisant le nombre de retournement par le nombre de pulses injectés. Des diagrammes donnant alors la probabilité de retournement en fonction de la durée et de l'amplitude peuvent alors être tracés et on peut alors vérifier que le processus de retournement obéit bien à loi donnée par Sun. Il est alors facile d'obtenir les paramètres A et I_{C_0} et observer leur comportement en fonction du champ magnétique.

Les résultats expérimentaux obtenus ont été comparés à des simulations macrospin. Il s'avère qu'il est possible d'obtenir des valeurs comparables aux valeurs expérimentales mais pour cela il est nécessaire d'utiliser des paramètres physiquement absurdes comme un angle initial entre l'aimantation de la couche libre et le polariseur d'environ 78°. Pour comprendre ces divergences, nous avons donc décidé d'étudier l'effet de différents paramètres à l'aide de simulations macrospin.

Nous avons observé l'effet de l'angle initial, de la polarisation et de l'amortissement. Tous trois font varier les paramètres A et I_{C_0} comme prédits dans la théorie et sont suffisants pour retrouver les valeurs expérimentales du courant

critique à température nulle. Néanmoins, il est impossible d'obtenir de bonnes valeurs pour A.
C'est ainsi que nous nous sommes finalement tournés vers des simulations micromagnétiques, afin de vérifier si l'hypothèse de macrospin est à remettre en cause. Nous n'avons observé le temps de retournement de l'aimantation en fonction de l'échange et il apparaît clairement que ce dernier exerce une grande influence. En traçant le temps de retournement en fonction de l'échange, nous pouvons observer deux comportements bien distincts. Pour une constante d'échange plus faible, le temps de retourment est fortement dépendant de l'échange ce qui correspond à un comportement micromagnétique. Pour des valeurs plus grandes d'échange, le temps de retournement est faiblement dépendant ce qui nous laisse approcher d'un comportment macrospin.
En calculant les paramètres A et I_{C_0} pour différents paramètres d'échange, l'influence de l'échange est évidente et il est même possible de s'approcher des valeurs expérimentales, ce qui nous laisse supposer que le comportement de l'aimantation à temps courts est régi par le micromagnétisme.

Chapitre 10

Problématique

We have previously studied magnetization dynamics with a constant current. However, when we look at the magnetization trajectory, it is clear that the reversal happens in a very short time, except in the case of precession.
It is therefore interesting to study magnetization steady state dynamics on very short time scales, with the help of short current pulses. A great advantage of using pulses is to be able to probe the role of the thermal activation, which has a considerable effect on measurements, especially when they are done at room temperature.
In order to study fast dynamics, we will use the Sun model described in section 4.2 page 54, and particularly the short time regime dominated by angular momentum conservation for which it is expected that

$$\frac{1}{\tau} = A(I_C - I_{C_0}) \tag{10.1}$$

where τ is the current pulse duration, A a constant, I_C the critical current necessary to reverse the magnetization, and I_{C_0} is the zero temperature critical current given by

$$I_{C_0\pm} = \frac{\alpha}{pg_\pm} \frac{2e}{\hbar} M_S V \mu_0 (H \pm H_k) \tag{10.2}$$

with α the damping, e the electron charge, p the polarization, $\hbar$ the reduced Planck constant, M_S the spontaneous magnetization, V the layer volume, μ_0 the Bohr magneton, H the applied field and H_k the anisotropy field. $g_\pm$ corresponds to the scalar function for the parallel and antiparallel spin valve configurations, i.e. $g(0)$ and $g(\pi)$.
Equation (10.1) can be rewritten as

$$\frac{1}{A} = \tau I_c - \tau I_{C_0} \tag{10.3}$$

The parameter A characterizes the link between charge and spin-angular momentum transport. Moreover A has to stay constant, to reflect the total momentum conservation. The second term of equation (10.3) τI_C is the product of the current pulse duration and its intensity, that is to say the spin-angular momentum. The last term, τI_{C_0} represents the minimum spin angular momentum necessary to overcome the magnetization damping.

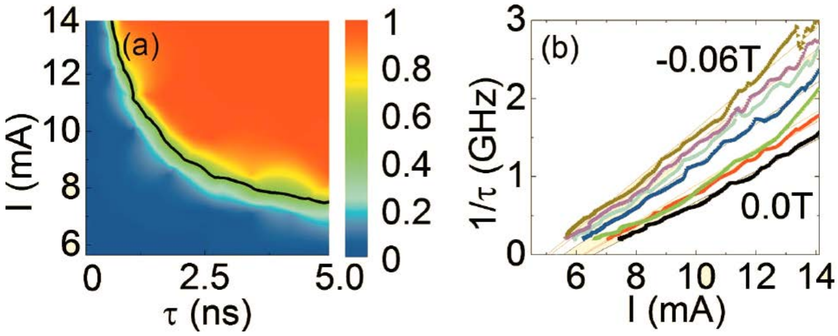

Figure 10.1: Switching probability for an AP→P reversal (a)Probability of magnetization reversal in function of current and pulse length at zero field (b) 50% probability of magnetization reversal for different fields

10.1 Experimental results

Measurements were done at the subnanosecond timescale by Bedau et al in 2010.[18] The spin valves they measured are the same ones used to study the precession states in sections 7.1 and 6.1 and described in more details in.[20]
In order to characterize the fast dynamics, current pulses were injected into the spin valves. Those pulses feature an amplitude I up to 2 V, and a duration τ comprised between a hundred picoseconds up to 10 nanoseconds. The process consists of four steps:

1. the spin valve is saturated
2. a magnetic field is applied
3. the current pulse is injected
4. the magnetization state is checked
    - if there is no reversal, we go back to step 3
    - if the magnetization switched, we go back to step 1

The switching probability is obtained by dividing the number of reversals by the number of injected current pulses. It is plotted on Figure 10.1 for the antiparallel to parallel configuration after 100 up to 100 000 injections of current pulses.
Figure 10.1(a) shows the switching probability in function of pulse length and current at zero field. We can clearly the boundary obeying equation (10.1).

Figure 10.1(b) is a plot of the 50% switching probability, i.e. the boundary, for different applied fields. The current dependence of the reversal frequency is clearly linear, as expected by equation (10.1). The slopes and the intercept change with the field.
It is quite easy to extract the parameters A and I_{C_0} from figure 10.1(b), as A is the slope of the curve, and AI_{C_0} the intercept. This was done and the resulting values are plotted on figure 10.2.
Figure 10.2 compares the experimental values (circles and triangles) with the macrospin model (solid lines). From the corresponding equations, they obtain

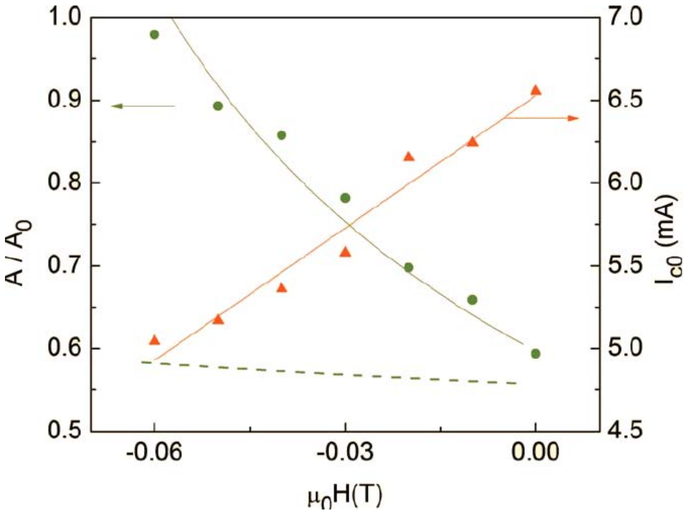

Figure 10.2: Dynamic parameter A and critical current I_{C_0} for different applied fields. The symbols (circles and triangles) represent the values measured, and the lines are obtained with macrospin simulations. The solid lines fit with the parameters $\mu_0 H_k = 245$ mT, $\alpha = 0.0111$, $p = 0.015$ and $\vartheta_0 = 1.36$ rad. The dashed line is obtained with $\vartheta_0 = 0.005$ rad from an angle dependence derived from a Boltzmann distribution. The A parameters have been normalized with the following coefficients: $A_{0,exp} = 3.3 \cdot 10^{11}$ s^{-1}A^{-1}, $A_{0,\vartheta_0=1.36} = 10^{13}$ s^{-}1A^{-}1, $A_{0,\vartheta_0=0.005} = 5 \cdot 10^{10}$ s^{-}1A^{-}1. Figure extracted from [18]

the parameters $\mu_0 H_k = 245$ mT, $\alpha = 0.011$, $p = 0.0015$ and $\theta_0 = 1.36 rad \simeq 78°$. Although the values of α/p and $\mu_0 H_k$ are close to the measured ones, it is not the case for the initial angle (too large) or the polarization (too small). The dashed line corresponds to a macrospin simulation, using the initial angle $\vartheta_0 = 0.005$ rad, found with and angular dependence derived from a Boltzmann distribution. It clearly shows a different behavior, as it almost doesn't depend on the field, contrary to the experimental parameter A.

Using the macrospin model to fit the experimental results, we obtain parameters, whose values are much too small or too large compared to the measured ones. However, when parameters close to the real ones are used, the behavior of the A parameter is not in agreement with the experiments.

10.2 Comparison with the Simulations

In this section, we will present the procedure we used to obtain the values of the critical current, the A parameter and the zero temperature critical current I_{C_0}.

The parameters used are the ones described in section 6.1 and are regiven in table 10.1. The sample is a 50 x 100 nm^2 nanopillar spin valve, with both hard and free layers with out of plane magnetizations. The current direction is perpendicular to the plane, and is considered positive when the electrons flow from

	Hard layer	Free Layer
M_S (A.m^{-1})	$5 \cdot 10^5$	$6.5 \cdot 10^5$
α	0.01	0.25
polarization	0.1	0.28
thickness (m)	$1.8 \cdot 10^{-9}$	$1.8 \cdot 10^{-9}$
surface (m^2)	$5 \cdot 10^{-15}$	$5 \cdot 10^{-15}$
$\mathbf{n_d}$	(0,0,1)	(0,0,1)
k (J·m^{-1})	$3 \cdot 10^6$	$3 \cdot 10^5$
ϑ_{ani}	0	0
φ_{ani}	$\pi/2$	$\pi/2$

Table 10.1: Parameters used for the simulations

the polarizer to the free layer. The current pulses have a square shape with a duration τ and an intensity I, called I_C when it reverses the magnetization.

Using the macrospin software, we calculate the current needed to observe a magnetization reversal for different current pulse durations. On Figure 10.3 we can see such switching rate vs. current curves, similar to the ones found experimentally (see figure 10.1(b)). This is a proof that both the analytical form and the macrospin simulations give the same $1/\tau$ behavior. The crosses correspond to the values from the simulations while the straight lines are linear fits of those values. The A parameter and AI_{C_0} simply correspond to the slope and intercept of the fits.

Afterwards, this procedure is repeated for different fields, and gives us the evolution of the I_{C_0} and A in function of the applied field H.
The theoritical values (green curve) are then compared with the experimental ones (red curve) on figure 10.4.
On Figure 10.4(a), we can see both $A(H)$ curves differ in the slopes and magnitude. The simulation values are greater than the theoritical ones, whereas the slope is smaller. This is in agreement with the simulations by Bedau et al., where the calculated A parameter was almost independent on the applied field, although the values are much bigger.
Figure 10.4(b) shows the evolution of the zero temperature critical current. The slopes between theory and simulations are much more closer, whereas both curves present a difference of $\simeq 2$ mA in magnitude.

This means the pulse duration necessary to observe magnetization reversal is much shorter experimentally. For a better understanding of the short time dynamics, a study of the influence of the different parameters will be presented in the following chapter.

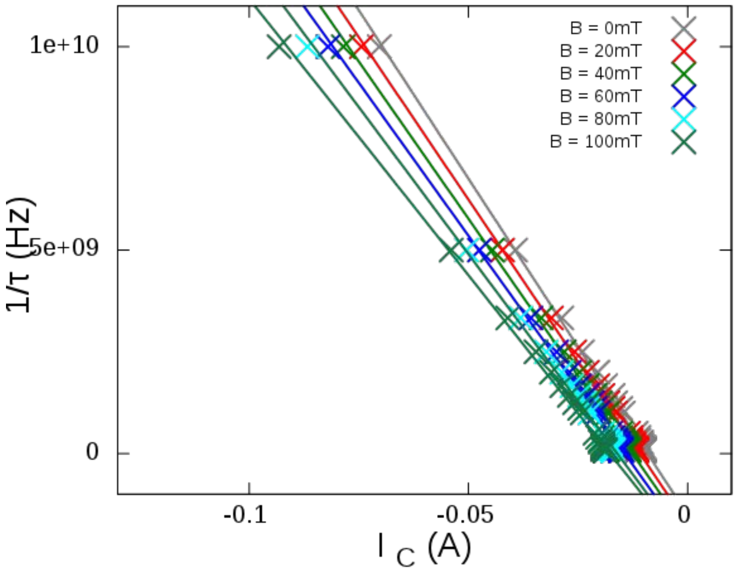

Figure 10.3: Switching rate vs critical current for different fields. The data points are represented by the crosses while the lines are obtained with the help of a linear regression.

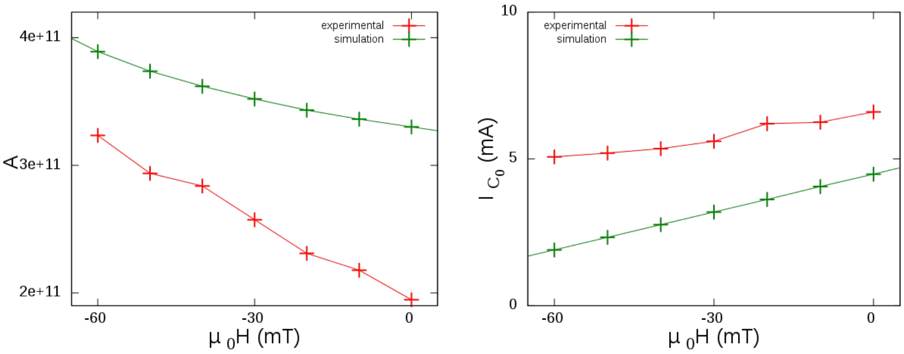

(a) A parameter in function of the applied field

(b) Critical current in function of the applied field

Figure 10.4: Comparison between the experimental and theoritical values of the critical current I_{C_0} and the A parameter. The red line represents the experimental results, while the green line represents the calculated values from the macrospin software

Chapitre 11

Simulations macrospin

As the macrospin model cannot satisfactorily describe the experimental results, we need to verify its veracity, testing the hypotheses. To this aim, we study the influence of different parameters. First, we will present the influence of the initial angle, then the anisotropy angle. Afterwards, we will describe the role of the damping, and the last parameter will be the polarization.

11.1 Role of the Initial Angle of the Magnetization

From equation (4.21) page 56, it is expected that the initial angle has a great influence on the magnetization dynamics.

Figure 11.1 shows the dynamics parameter A and the zero temperature critical current I_{C_0} in function of the external field for different initial positions, given by the angle ϑ_0 with the easy axis. The red, blue and green curves show an initial angle of 5°, 10° and 15° respectively.

It is clear that the initial angle has very little influence on the critical current, as the slope seems unaffected and the only change is a very small shift of the intercept. The critical current decreases as the initial angle increases, i.e. it is easier to reverse the magnetization the further away we start from the stable position. However, it may be noted this is only true up to a certain angle limit. Otherwise, the initial position influences greatly the A parameter : an increase of 10 degrees for the angle can result in a rise of two thirds of its value. Overall, we can see A increases with the initial angle, indicating the magnetization reversal time diminishes when we're getting further away from the stable position. Although the slopes vary with ϑ_0, it is not sufficient to approach the experimental slope.

11.2 Role of the Anisotropy Angle

In chapter 8, it was shown the anistropy angle plays an important role in the magnetization reversal. It is therefore expected to also influence the reversal time.

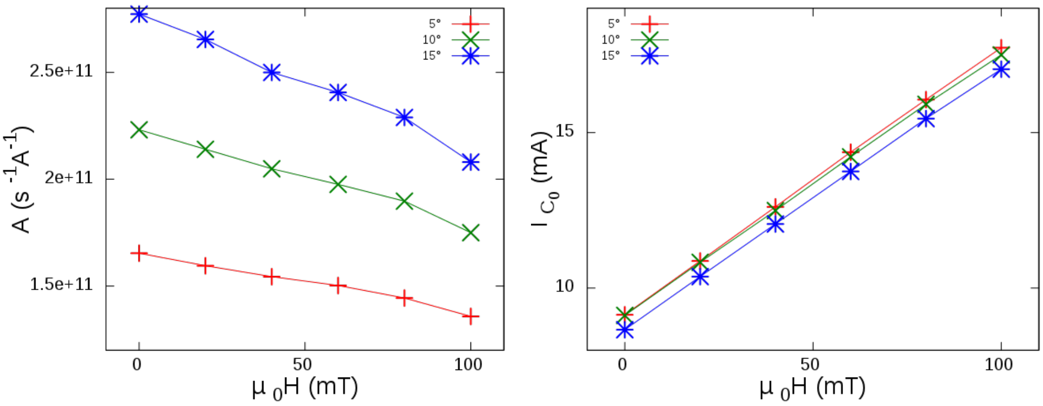

(a) Dynamic parameter A for different fields

(b) Zero temperature ritical current for different fields

Figure 11.1: A parameter and critical current at different fields for different values of the initial angle. The red, green and blue curves respectively represent an initial angle ϑ_0 of 5°, 10° and 15°.

Figure 11.2 shows the the evolution of the critical current I_{C_0} and the angular momentum A in function of the applied field for different values of the anistropy angle ϑ.

The first observation is that the critical current increases with the anisotropy angle, whereas the slope seems unchanged. The anisotropy clearly hinders the magnetization reversal.

Looking at the angular momentum, we can see ϑ influences its value, as well as the slope of $A(\mu_0 H)$. The absolute value of A decreases when the anisotropy angle decreases, confirming the reversal time is longer.

11.3 Role of the Damping

From equation (10.2) page 123, it is clear the damping plays an important role in the magnetization reversal time. To understand its influence, the parameter A and the critical current were plotted for different values of the damping constant.

The first observation is that the critical current I_{C_0} increases with the damping, which is consistent with the fact that the damping acts against the magnetization reversal, and thus more current is needed. However, the A parameter decreases when the damping increases.

The damping also has an effect on the slopes of $I_{C_0}(\mu_0 H)$. We can see the slope increases with the damping, which is expected from (10.2) as the critical current is proportional with α. Nevertheless, it isn't the case for A as the slope is weakly affected by the damping.

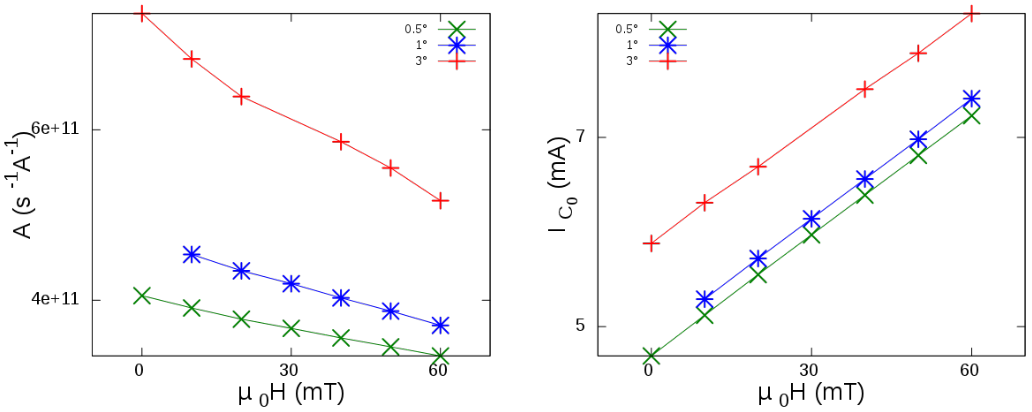

(a) Dynamic parameter A for different fields (b) Critical current for different fields

Figure 11.2: A parameter and critical current at different fields for different values of the anisotropy angle. The green, blue and red lines respectively correspond to an anisotropy angle of 0.5°, 1° and 3°.

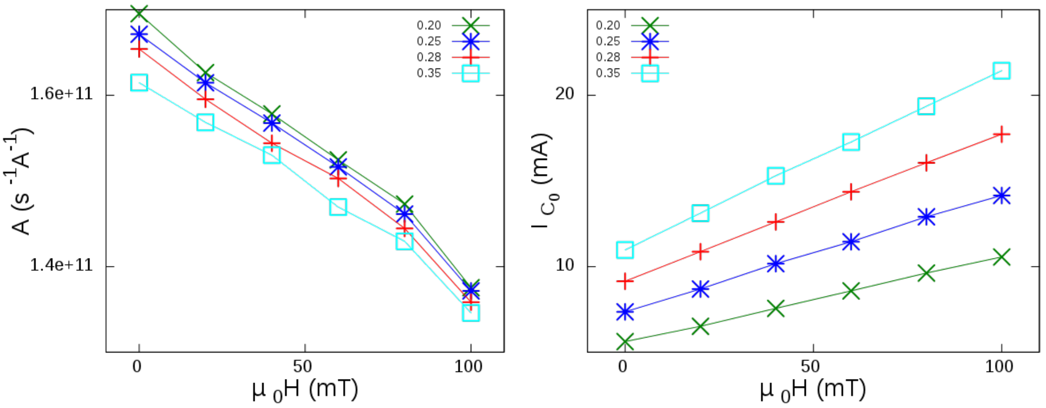

(a) Dynamic parameter A for different fields (b) Critical current for different fields

Figure 11.3: A parameter and critical current at different fields for different values of the damping

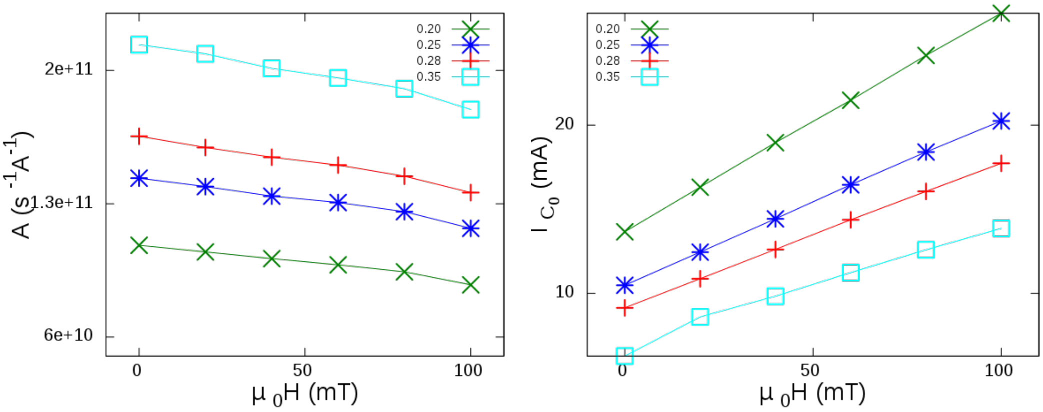

(a) Dynamic parameter A for different fields

(b) Critical current for different fields

Figure 11.4: A parameter and critical current at different fields for different values of the polarization. The green, blue, red and cyan curves represent polarizations $p = 0.20$, 0.25, 0.28 and 0.35 respectively.

11.4 Role of the Polarization

Figure 11.4 shows the angular momentum and the critical current in function of the external field for different values of the polarization. The green, blue, red and cyan curves represent polarization values of 0.20, 0.25, 0.28 and 0.35 respectively. Its influence on the reversal time is predicted because of equation (10.2).

The critical current decreases as the polarization increases, which is expected, since with more polarization, there will be more spins and thus more momentum to reverse the magnetization. The A parameter behavior can be explained with the same reasoning.
The curves $A(\mu_0 H)$ present a similar slope and a pretty important shift between them. The polarization doesn't infer much with the slopes, but mostly on the values of the angular momentum. On the other hand, the polarization affects more the slopes of $I_{C_0}(\mu_0 H)$, as well as its values.

The different simulations show the parameters can greatly influence the critical current and the angular momentum. It is quite easy to obtain for the critical current the values measured experimentally by varying some parameters. It's not possible to do the same with the angular momentum, as it can be shifted but its slope nerver changes much.
This is probably a limit of the macrospin approach and the micromagnetics may be able to reproduce the experimental results, which will be described in the following chapter.

Chapitre 12

Simulations micromagnétiques

In this chapter, we will first describe the LLG Micromagnetics Simulator, the software we used for our micromagnetics simulations. Then, after a brief presentation of the parameters we chose, we will depict the reversal process.We will define the nucleation time. Thereafter, we will study the evolution of the reversal process with the exchange constant A_{ex} (not to be confused with the A parameter). We will also describe the nucleation time, and we will compare the micromagnetics simulations with the experimental results from Bedau et al.[18] last.

12.1 LLG Micromagnetics Simulator by M. Scheinfein

The software developed by Michael Scheinfein uses a micromagnetics approach to study magnetization dynamics. It solves the Landau Liftshitz Gilbert equation with Langevin dynamics by relaxation and/or integration.

The software allows all kinds of shapes for the samples, thanks to the use of masks. The magnetic layers can of course be divided in cells, the user chooses the dimensions of the magnetic layers and the number of cells per direction N_x, N_y, N_z. For each layer, all the usual parameters (damping, anisotropy...) can be input. The field and current can also take any shape as the user can, for example, use a non-uniform applied field composed of different sequences of varying intensity, duration and direction. It's also possible to tune the computation parameters.

During the computation, it's possible to watch the magnetization evolve, as well as the magnetoresistance, the different fields or the energy density among others.

Figure 12.1 shows the graphic user interface during a simulation. On the left panel is the menu, composed of many tabs, from which we can choose the different views, the computation parameters or uniform fields. On the right panel is the viewing window showing here the different cell magnetizations represented by yellow arrows.

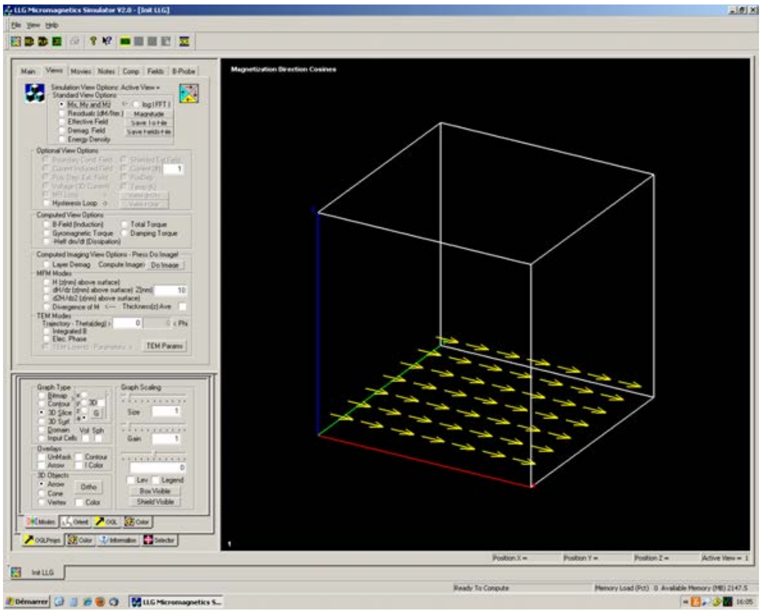

Figure 12.1: Main menu

12.2 Description of the reversal process

The magnetization reversal of a ferromagnet can be described with the Stoner Wohlfarth model (section 1.3.1), assuming a macrospin approach. However, macrospins are only appropriate for very small samples, as it requires the magnetic moments to be aligned in the same direction.

Usually, we can distinguish two steps during magnetization reversal in micromagnetics simulations. First, there is a nucleation at a specific position of the layer, depending on the shape and size. The domain nucleated is delimited by a domain wall, which will then propagate in the layer until the whole magnetization is reversed. This is due to the competition between the dipolar field created by the hard layer, and the demagnetizing field generated by the free layer. The former will favor the nucleation at the extremities, as its intensity is weaker in the center, contrary to the demagnetizing field, which will thus favor a nucleation in the center.

On Figure 12.2, we can see the evolution of the magnetization along time of a 100 nm x 200 nm hexagonal spin valve free layer. The red and blue colors respectively correspond to the up and down magnetizations. We can see the reversal starts at one of the extremities of the hexagon, and then propagates to the whole extremity. Afterwards, it continues along the longest diagonal of the hexagon.

12.3 Parameters

For the following simulations, we used a spin valve structure composed of two 100 x 100 nm^2 magnetic layers whose parameters are given in table 12.1. Each

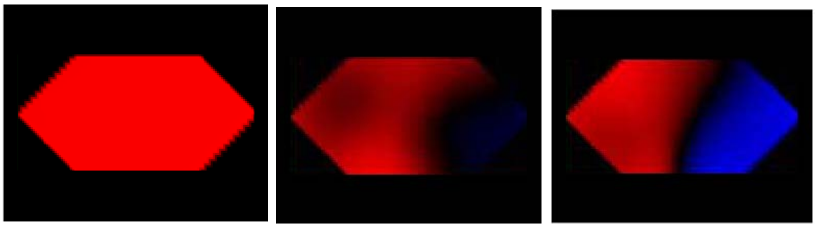

(a) initial state (b) $t = 0$ ps (c) $t = 470$ ps

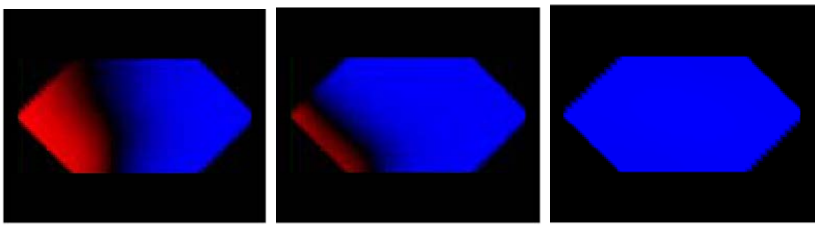

(d) $t = 840$ ps (e) $t = 1390$ ps (f) final state

Figure 12.2: Spin-current induced reversal of a 100 x 200 nm^2 hexagon nanopillar. The blue and red color correspond respectively to down and up orientation along the z direction. The parameters are the ones described in [20]. Figures extracted from [32].

layer is 2 nm thick, and the polarization is $p = 0.05$.

	Hard layer	Free Layer
M_S (A.m^{-1})	$6 \cdot 10^5$	$7.1 \cdot 10^5$
k (J·m^{-1})	$8 \cdot 10^5$	$3.6 \cdot 10^5$

Table 12.1: Parameters used for the simulations

12.4 Definition of the Nucleation Time

To determine the nucleation time, we plot the three magnetization components in function of time. It is then possible to see that m_x or m_y changes direction at a certain time which would correspond to the nucleation time. On Figure 12.3(a), we plotted the time evolution of the three components of the magnetization. m_x, m_y and m_z are respectively represented by the red, green and blue curves. We observe the change of direction for m_x and m_y at $t = 10.3$ ns.
With the LLG micromagnetics simulator, we also have access to the energy of the system, and thus we can also plot the energy in function of time. On Figure 12.3(b), we can see the energy maximum is at 10.1 ns, very close the value found $t = 10.3$ ns previously found.

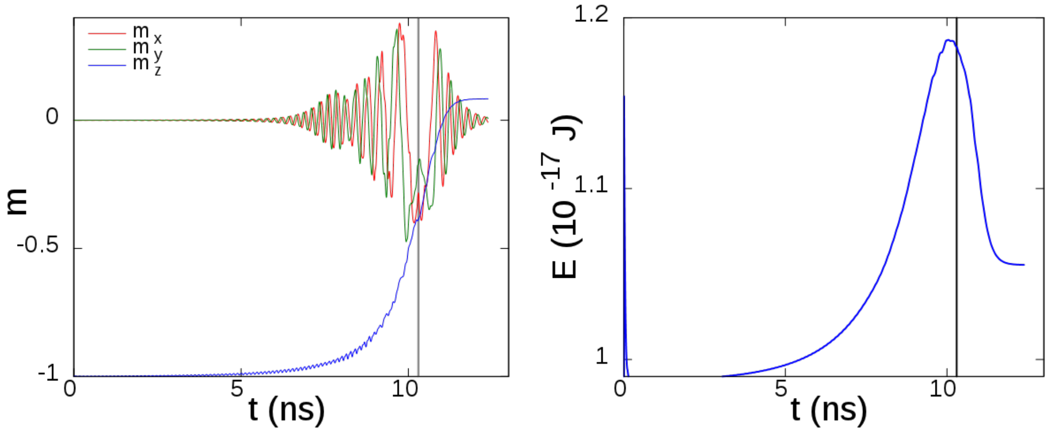

(a) Magnetization components vs. time.The red, green and blue lines represent respectively m_x, m_y and m_z.

(b) Energy vs. time

Figure 12.3: Evolution in time of the magnetization and of the energy. The exchange constant is $A_{ex} = 5 \cdot 10^{-11}$ J/m The vertical line at 10.3ns is the nucleation time.

12.5 Influence of the Exchange Constant A_{ex}

The exchange field is predominant in micromagnetics and plays a significant role in the nucleation process, and thus the fast dynamics.
Figure 12.4 shows the time evolution of the z component of the magnetization for different values of the exchange. It goes from $A_{ex} = 10^{-11}$ J/m to $A_{ex} = 3{\cdot}10^{-10}$ J/m, covrring a large range of values. Therefore, if a change in the magnetization dynamics with the exchange constant should be visible.
On Figure 12.4, it is clear that increasing the exchange constant increases the nucleation time. This behavior is expected, since we go from micromagnetics to the macrospin model, as A_{ex} increases. In the macrospin model, the whole layer magnetization needs to be reversed, thus demanding a lot of energy. With micromagnetics, much less energy is needed to reverse a small domain, which will then propagate to the rest of the sample.

To study the nucleation behavior, we need to compare the different curves plotted on Figure 12.4. We decide to plot the time when $m_z = -0.8$ in function of the exchange constant A_{ex} (see Figure 12.5).
On Figure 12.5, we can clearly see two types of behavior. The sharp change of the slope happens at $A_{ex} = 10^{-10}$ J/m. Up to that limit, the nucleation time strongly depends on the exchange constant, whereas this dependence decreases when $A_{ex} > 10^{-10}$ J/m. Therefore, the first part describes micromagnetics dynamics, while high values of the exchange will lead to the macrospin model. For an exchange constant of $A_{ex} = 10^{-10}$ J/m, the exchange length is found to be $l_{ex} = 14$ nm, which is in agreement with the size of the samples, whose size is 100 nm x 100 nm. Using small values of the exchange may thus be the key to explain the results by Bedau et al.

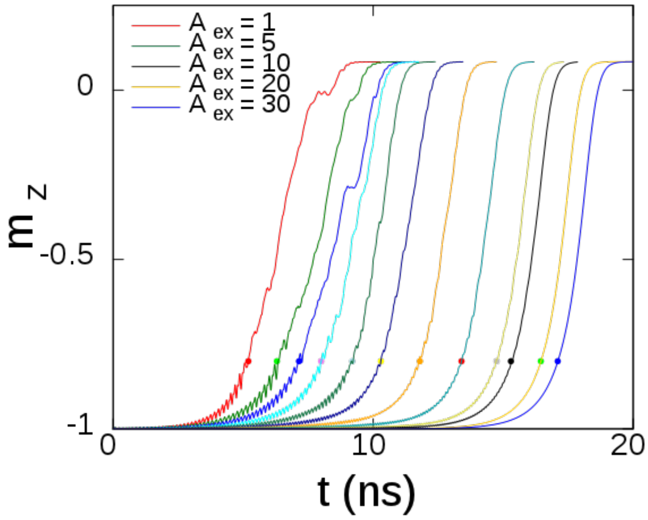

Figure 12.4: Magnetization vs Time with an injected current of 2 mA. The first 10 curves (from left to right) show the evolution of the magnetization for the exchange constant from $A_{ex} = 10^{-11}$ J/m to $A_{ex} = 10^{-10}$ J/m. The yellow and blue curves on the far right respectively represent $A_{ex} = 2 \cdot 10^{-10}$ J/m and $A_{ex} = 3 \cdot 10^{-10}$ J/m. The circles indicate the position where $m_z = -0.8$.

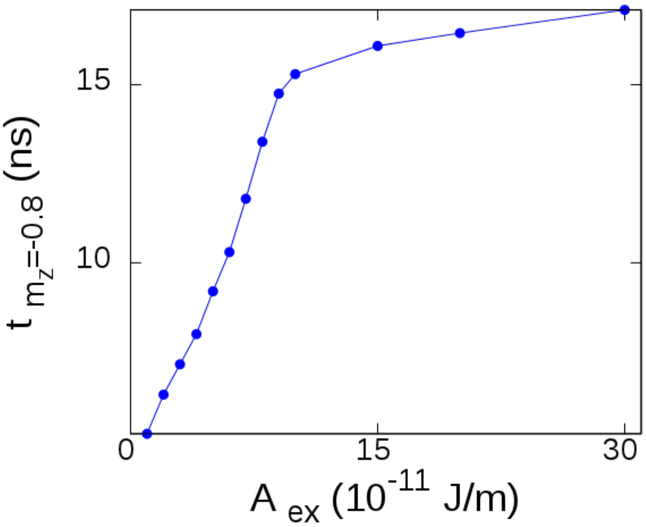

Figure 12.5: Nucleation Time vs Exchange

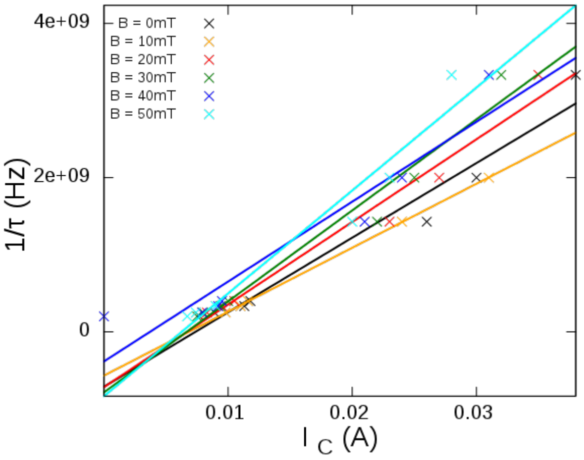

Figure 12.6: Switching rate in function of the critical current. The crosses represent the micromagnetics simulations values. The straights lines are obtained through linear regressions.

12.6 Short Time Regime

We can now compare the experimental results obtained by Bedau et al. to the micromagnetics simulations. First, we describe the process leading to the values of the zero temperature critical current I_{C_0} and the dynamic parameter A for the exchange constant $A_{ex} = 10^{-10}$ J/m and then we will see the influence of the exchange parameter.

The simulations are done with the parameters described in section 12.3, we use a rectangle shaped spin valve structure, whose configuration is initially antiparallel. After the current pulse injection, we check whether a magnetization reversal happened. In the case of a reversal, we try another pulse with the same duration but with less amplitude. Otherwise, it is increased. The critical current I_c is found when it satisfies two conditions: it can reverse the magnetization and a current I whose amplitude is given by $|I - I_C \leq 1$ mA cannot reverse the magnetization.

On Figure 12.6, we can see the switching rate in function of the current amplitude for different applied fields. As expected, we observe a linear behavior, following $1/\tau = A(I - I_{C_0})$.

We can extract the zero temperature critical current I_{C_0} and the dynamics parameters A from those curves. Although we use linear regressions, it may be noted they describe the calculated values less and less as the applied field increases. It is then possible to compare the influence of the exchange parameter A_{ex} on magnetization dynamics in the short time regime. The zero temperature critical current and the A parameter are therefore plotted on Figure 12.7. The different exchange constants $A_{ex} = 10^{-11}$ J/m, $A_{ex} = 5 \cdot 10^{-11}$ J/m and $A_{ex} = 10^{-10}$ J/m are represented by the red, blue and green lines respectively. On Figure 12.7(a), the zero temperature critical current I_{C_0} is plotted in function of the applied field. We can see the critical current increases with the exchange, meaning that more energy is needed to reverse the layer magnetization.

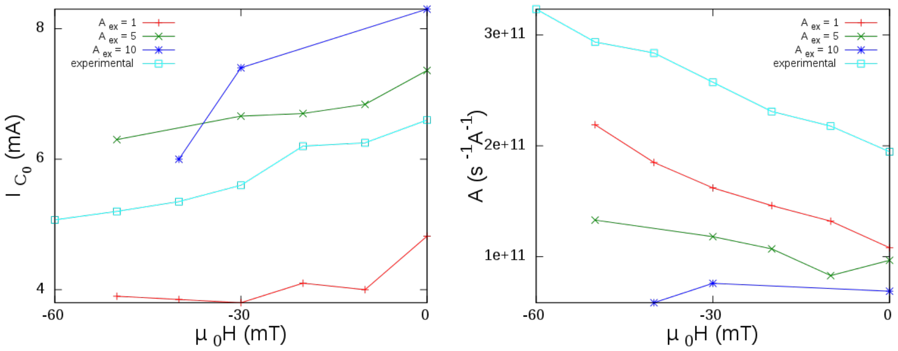

(a) Zero temperature critical current (b) Dynamic parameter A

Figure 12.7: Evolution of the critical current I_{C_0} and the A parameter with the applied field. The red, green, blue lines correspond to the exchange constant $A_{ex} = 10^{-11}$ J/m, $A_{ex} = 5 \cdot 10^{-11}$ J/m and $A_{ex} = 10^{-10}$ J/m. The cyan line corresponds to the experimental results found by Bedau et al.

It is expected, as we go from micromagnetics for $A_{ex} = 10^{-11}$ J/m, whereas the macrospin model is more appropriate when $A_{ex} = 10^{-10}$ J/m. Moreover, as the exchange increases, so does the reversal time.

The evolution of the dynamic parameter A in function of the field is plotted on Figure 12.7(b). The A parameter decreases with the exchange, in agreement with the behavior observed with the zero temperature critical current. However, it is important to note that the slope of the $A(\mu_0 H)$ curves are very dependent on the exchange constant. Indeed, for $A_{ex} = 10^{-10}$ J/m, the dynamic parameter is almost unaffected by the field. As the exchange decreases, we can see the field dependence increase.

On Figure 12.7, the experimental values are also represented by a straight cyan line. We can therefore compare the simulation values with the experimental ones. In the case of the zero temperature critical current, the experimental curve is found between the ones corresponding to $A_{ex} = 10^{-11}$ J/m and $A_{ex} = 5{\cdot}10^{-11}$ J/m. The slope is also close to the the theoritical ones.

As for the dynamics parameter A, we can see the experimental values are larger than the ones we obtained from the simulations. However, the interesting feature of Figure 12.7(b) is the comparison of the slopes. Indeed, the slope corresponding to $A_{ex} = 10^{-11}$ J/m is very close to the experimental one.

On the one hand, we described the influence of the parameters using a macrospin model, and we showed we could shift the zero temperature critical current and the A parameter. It was also possible to change the slope of the I_{C_0} curves. However, we could not explain the field dependence of the dynamic parameter.

On the other hand, we studied the effect of the exchange. It was shown it had an effect on the zero temperature critical current, mostly shifting the curve. It also considerably changes the slope of the A parameter curves, such as reproducing the experimental slope when the exchange constant is $A_{ex} = 10^{-11}$

J/m. It is thus possible to explain the experimental results with micromagnetics.

Although we showed the limit of the macrospin model and confirmed the micromagnetics was appropriate to explain the results obtained by Bedau et al., the reversal mechanisms are not fully understood. The next step would be to focus on micromagnetics and understand its origin.

Conclusion

Cette thèse a pour objet l'étude de la dynamique d'aimantation sous l'effet de transfert de spin dans des vannes de spin.

Dans cette optique, nous avons développé un logiciel simulant la dynamique de l'aimantation sous l'effet de transfert de spin dans des vannes de spin. Celui-ci résout l'équation de Landau Lifshitz Gilbert à l'aide de l'algorithme de Runge-Kutta Cash-Karp et produit des trajectoires de l'aimantation. Grâce à ces trajectoires, nous pouvons générer des cycles d'hystérésis, des diagrammes d'état ou bien encore des astroïdes. Le programme offre aussi la possibilité d'utiliser des pulses de courant afin d'accéder à la dynamique d'aimantation à l'échelle de la nanoseconde.

Dans un premier temps, nous nous sommes concentrés sur l'étude des diagrammes d'état champ courant. Ceux-ci sont particulièrement utiles pour comprendre la dynamique d'aimantation. En effet, ils permettent de cartographier les configurations possibles des vannes de spin en fonction du courant injecté et du champ magnétique appliqué. Sur les diagrammes apparaissent quatre zones correspondant à quatre états possibles des vannes de spin. Deux régions définissent une configuration toujours parallèle ou antiparallèle. Une troisième zone, située entre les deux précédentes correspond à une zone de bistabilité dont la configuration finale dépend de l'état initial. Une dernière configuration est un état dynamique de précession, où le courant compense exactement l'amortissement. De plus, d'après la théorie, le courant de retournement doit avoir un comportement linéaire par rapport au champ appliqué. Cependant, ces prédictions théoriques sont en désaccord avec les diagrammes d'état observés. En effet, les quatre régions sont bien observées mais le comportement du courant de renversement n'est pas linéaire. Il apparaît qu'à courants faibles, le courant critique semble indépendant du courant injecté. Il faut alors atteindre un courant seuil pour retrouver un comportement linéaire.

Nous avons étudié l'influence de différents paramètres sur les diagrammes d'état. L'introduction d'un angle d'anisotropie fait apparaître le comportement observé dans les diagrammes expérimentaux. On remarque aussi que plus l'angle d'anisotropie augmente, plus le courant seuil est grand. Nous avons aussi calculé des diagrammes d'état pour différentes valeurs de la constante d'anisotropie du quatrième ordre. Lorsque nous avons ajouté un faible champ d'anisotropie dans le plan, l'influence de k_2 est visible. La constante d'anisotropie augmente la valeur des courants seuil avec sa valeur. Nous pouvons en déduire que la constante d'anisotropie du quatrième ordre n'est pas capable de briser la symétrie à elle

seule mais a une influence certaine même lorsque la brisure est faible.
Le champ appliqué, quant à lui, est aussi une source possible de la brisure de symétrie. Les diagrammes calculés avec un champ appliqué ayant un angle avec l'axe facile d'aimanation montrent une zone indépendante du courant avec des courants seuils. Ces derniers augmentent aussi avec la valeur de l'angle. Néanmoins, nous pouvons observer que l'influence du champ appliqué est beaucoup plus faible que l'anisotropie. En effet, les angles du champ appliqué nécessaires pour imiter un diagramme calculé avec un angle d'anisotropie sont bien plus grands. 0.5 degrés d'anisotropie correspond à 5 degrés de champ appliqué.
Un autre candidat possible pour la brisure de symétrie est le polariseur. Nous avons donc calculé des diagrammes d'état pour différents angles du polariseur. Nous avons observé un changement des pentes du courant de retournement, ce qui est attendu d'après l'expression du courant de retournement, mais aucun courant seuil n'est apparu. Ceci nous conduit à conclure que le polariseur est incapable de brisure la symétrie.
Les diagrammes d'état, jusqu'ici, ont été mesurés à l'aide d'un faible courant alternatif dont la fréquence est connue. Un nouveau type de diagramme a été réalisé en utilisant un faible champ appliqué oscillant, en plus du champ extérieur. Ce diagramme dV/dH donne accès à des états jusqu'alors inconnus. En effet, il apparaît une branche verticale visible sur dV/dH mais pas sur dV/dI. En calculant les trajectoires correspondantes, nous avons constaté qu'il s'agit d'états cantés, ce sont des états gelés à des angles finis de l'axe facile.

La deuxième partie de la thèse fut consacrée à la dynamique d'aimantations à temps courts, c'est-à-dire de l'ordre de la nanoseconde. Le but était de rendre compte des résultats de dynamique ultra-rapide obtenus dans l'équipe d'Andrew Kent à l'Université de New York (NYU). En effet, il a été possible d'étudier la dynamique de l'aimantation lorsqu'on injecte des pulses de courant dont la durée peut varier d'une seconde à quelques centaines de picosecondes. Ces études permettent de distinguer deux régimes : un régime pour les durées de pulse longues dominé par l'activation thermique et un régime pour les pulses courts dominé par la conservation du moment cinétique.

Les théories développées par Jonathan Sun ne peuvent expliquer que partiellement les résultats obtenus expérimentalement. Nous avons donc cherché à expliquer l'origine de ce désaccord en étudiant l'importance de certains paramètres comme l'anisotropie magnétocristalline, les effets de tailles, le champ dipolaire etc...

Nos résultats montrent que les différents paramètres influent bien sur le courant critique et le moment angulaire, mais ils ne permettent pas d'expliquer les résultats expérimentaux. En effet, l'angle initial entre l'aimantation et l'axe facile d'anistropie ne modifie que très peu le courant critique, mais son influence est plus importante sur la valeur du moment angulaire, sans pour autant modifier sa pente. La constance d'amortissement ne joue que très peu sur le moment angulaire mais augmente le courant critique. Quant à la polarisation, elle diminue le courant critique et augmente la valeur du moment angulaire, en ne jouant que faiblement sur sa pente. Nous pouvons en déduire qu'un choix approprié des paramètres permet d'expliquer le courant critique, mais ceux-ci n'influencent que trop peu la pente du moment angulaire pour pouvoir expliquer les résultats expérimentaux.

Nous avons alors fait appel au logiciel de simulation micromagnétique de M. Scheinfein. Nous nous sommes rendus compte qu'en modifiant la constante A d'échange, nous changions fortement le moment angulaire ainsi que sa pente. C'est ainsi que nous avons pu reproduire la pente obtenue expérimentalement. Nous pouvons donc en conclure que l'approche micromafnétique offre une meilleure description de la dynamique ultra-rapide que le modèle macrospin.

Conclusion (English)

The aim of this thesis was to study the magnetization dynamics and spin transfer effect in spin valves.

With this in mind, we developed a software simulating magnetization dynamics with spin transfer in spin valves. It solves the Landau Lifshitz Gilbert equation with the help of the Runge-Kutta Cash-Karp algorithm and generates trajectories of the magnetization. With the trajectories, it is easy to plot hysteresis cycles, state diagrams or astroids. Current pulses can also be used to study ultra-fast dynamics of the magnetization.

We first studied current-field state diagrams. They are very useful to understand magnetization dynamics. Indeed, they allow us to map the possible configurations of spin valves in function of the injected current and the external magnetic field. We can distinguish four zones on the state diagrams corresponding to four possible states for the spin valves. Two domains describe a configuration that is always parallel or antiparallel. A third zone, located between the two previously described ones, defines a bistability region, for which the final state depends on the initial magnetization. The last configuration is a state of precession, where the current exactly compensates the damping. Furthermore, according to the theory, the switching current presents a linear behavior with respect to the magnetic field. However, those theoritical predictions disagree with the measured state diagrams. Indeed, we do observe the four regions but the switching current doesn't show a linear behavior. For small currents, the switching current seems independent on the injected current, and a threshold current needs to be reached to find a linear behavior.

We studied the influence of different parameters on the state diagrams. Introducing an anisotropy angle in the system reproduces the behavior that was observed on the measured state diagrams. We also notice the threshold current increases with the anisotropy angle. We also calculated a few state diagrams for different values of the fourth order anisotropy constant k_2. Its effect is visible when we add a small in plane anisotropy field. The threshold currents also increase with value of k_2. We can thus deduce the fourth order anisotropy constant is not able to break the symmetry of the system on its own, but its effect is important even for a small symmetry breaking. The external field can also break the symmetry. The calculated state diagrams with an angle between the external field and the easy anisotropy axis show a region where the switching current is independent on the current and threshold currents. The latter increase with the angle. However, we can see the influence of the external field is smaller than the influence of the anisotropy. Indeed, the external field angle necessary to reproduce the same effect as with an anisotropy angle is much bigger. Here, 0.5 degrees for the anisotropy match 5 degrees for the external field. Another possibility for the breaking of symmetry is the polarizer. We calculated state diagrams for different angles for the polarizer with respect to the easy anisotropy axis. We can see a change in the slopes of the switching current, which is expected from its expression, but no threshold current appears. Until now, all the state diagrams have been measured with the help of a small alternative current whose frequency is known. Another type of state diagram was measured using a small fluctuating field in addition to the external field. This dV/dH diagram shows new states we didn't have access to. Indeed, there is a vertical branch visible on dV/dH and not dV/dI. We calculated the corresponding trajectories and found canted states, for which the magnetization was frozen at certain angles.

The second part of this thesis describes fast magnetization dynamics, i.e. at the subnanosecond time scale. The goal was to explain the ultra-fast dynamics results obtained by Andrew Kent's team at New York University (NYU). Indeed, it is possible to study magnetization dynamics when a current pulse is injected, its duration lasting from one second to a hundred picoseconds. This study shows two different regimes: one for long current pulses ruled by thermal activation et one for short current pulses dominated by the angular momentum conservation.
Jonathan Sun developed a model which can only partially explain the experimental results. We thus tried to explain the origin of this disagreement by studying the influence of certain parameters, such as the magnetocrystalline anisotropy, the size effect, the dipolar field among others.

Our results show the different parameters do have an influence on the critical current and the angular momentum. However, it is not enough to explain the experimental results. Indeed, the initial angle between the magnetization and the easy anisotropy axis leaves the critical current almost unchanged, although it modifies the angular momentum but not its slope. The damping constant does not change the angular momentum, but greatly increases the critical current. The polarization decreases the critical current and increases the angular momentum, showing a small influence on the slope. Hence, we can deduce it is possible to reproduce the experimental critical current with an appropriate choice of parameters. Nevertheless, their influence of the angular momentum slope is too small to explain the experimental results.

We then used the micromagnetics software designed by M. Scheinfein. We studied the influence of the exchange parameter on fast dynamics, and noticed it changed considerably the slope of the angular momentum. Indeed, we managed to obtain the experimental slope of the angular momentum, which leads to believe micromagnetics offer a better description of ultra-fast dynamics than the macrospin approach.

Annexe : Code source du programme de simulation

Listing 12.1 – **Clock.cpp**

```
#include "Clock.h"

#include <Qt/QtXml>
#include<iostream>

Clock::Clock(NewParameters params)
{
  timeStamp=0;
  timeWindow=params.getTime()["window"];
  timeStep=params.getTime()["step"];
  maxTimeStep=params.getTime()["maxStep"];
}

Clock::~Clock()
{

}

void Clock::setTimeStamp(double value)
{
  timeStamp=value;
}

double Clock::getTimeStamp()
{
  return timeStamp;
}

void Clock::setTimeStep(double value)
{
  timeStep=value;
}

double Clock::getTimeStep()
```

```
{
  return timeStep;
}


void Clock::setTimeWindow(double value)
{
  timeWindow=value;
}

void Clock::setMaxTimeStep(double value)
{
  maxTimeStep=value;
}

double Clock::getTimeWindow()
{
  return timeWindow;
}
double Clock::getMaxTimeStep()
{
  return maxTimeStep;
}
```

Listing 12.2 – **Vector3.cpp**

```
#include "Vector3.h"

Vector3::Vector3()
{
  x=0;
  y=0;
  z=0;
}

Vector3::~Vector3()
{

}

double Vector3::getX()
{
  return x;
}

double Vector3::getY()
{
  return y;
}

double Vector3::getZ()
{
  return z;
}

void Vector3::setX(double newx)
{
  x=newx;
}

void Vector3::setY(double newy)
{
  y=newy;
}

void Vector3::setZ(double newz)
{
  z=newz;
}

void Vector3::setVector(double newx,double newy,double newz)
{
  x=newx;
```

```
  y=newy;
  z=newz;
}

void Vector3::add(Vector3 vec)
{
  x+=vec.x;
  y+=vec.y;
  z+=vec.z;
}

double Vector3::dotProduct(Vector3 vec)
{
  return (x*vec.x+y*vec.y+z*vec.z);
}

void Vector3::crossProduct(Vector3 vec)
{
  double newx=y*vec.z-z*vec.y;
  double newy=z*vec.x-x*vec.z;
  double newz=x*vec.y-y*vec.x;
  x=newx;
  y=newy;
  z=newz;
}

void Vector3::mult(double number)
{
  x=x*number;
  y=y*number;
  z=z*number;
}

void Vector3::copy(Vector3 vec)
{
  x=vec.getX();
  y=vec.getY();
  z=vec.getZ();
}
```

Listing 12.3 – **AppliedFieldVector3.cpp**

```
#include "AppliedFieldVector3.h"

#include<cmath>

#include "Constants.h"
#include "Parameters.h"

AppliedFieldVector3::AppliedFieldVector3(Clock  clock, Pulse *field)
{
    if(field->getAngle()==90)
        {
            z=0;
        }
    else
        {
            z=field->getLevel(clock.getTimeStamp())*cos(field->getAngle()*M_PI/180)/Constants::MU0;
        }
    if(field->getAngle2()==90)
        {
            x=0;
        }
    else
        {
            x=field->getLevel(clock.getTimeStamp())*sin(field->getAngle()*M_PI/180)*cos(field->getAngle2()*M_PI/180)/Constants::MU0;
        }
    //x=field->getLevel(clock.getTimeStamp())*sin(field->getAngle()*M_PI/180)*cos(field->getAngle2()*M_PI/180)/Constants::MU0;
    y=field->getLevel(clock.getTimeStamp())*sin(field->getAngle()*M_PI/180)*sin(field->getAngle2()*M_PI/180)/Constants::MU0;
    //z=field->getLevel(clock.getTimeStamp())*cos(field->getAngle()*M_PI/180)/Constants::MU0;
}

AppliedFieldVector3::~AppliedFieldVector3()
{

}
```

Listing 12.4 – **AniVector3.cpp**

```
#include "AniVector3.h"

#include <cmath>
#include <iostream>

#include "Constants.h"

AniVector3::AniVector3(Layer layer)
{
  /* Anisotropy vector for the first order only

  double Hk, CosAni;
  Vector3 A;
  Hk=2*layer.getK()/layer.getMs()/Constants::MU0;
  if (layer.getAngleAni2()==90)
    {
      A.setX(0);
    }
  else
    {
      A.setX(sin(layer.getAngleAni()/180*M_PI)*cos(layer.
          getAngleAni2()/180*M_PI));
    }
  A.setY(sin(layer.getAngleAni()/180*M_PI)*sin(layer.
      getAngleAni2()/180*M_PI));
  if (layer.getAngleAni()==90)
    {
      A.setZ(0);
    }
  else
    {
      A.setZ(cos(layer.getAngleAni()/180*M_PI));
    }
  CosAni=A.dotProduct(layer.getMag());
  x=Hk*A.getX()*CosAni;
  y=Hk*A.getY()*CosAni;
  z=Hk*A.getZ()*CosAni; */


  double Hk1,Hk2,CosAni,SinAni;
  double HkPlane,CosPlane,SinPlane;
  Vector3 A,APlane;
  Hk1=2*layer.getK1()/layer.getMs()/Constants::MU0;
  Hk2=4*layer.getK2()/layer.getMs()/Constants::MU0;
  HkPlane = 2*layer.getKPlane()/layer.getMs()/Constants::
    MU0;
  A.setX(sin(layer.getAngleAni()/180*M_PI)*cos(layer.
     getAngleAni2()/180*M_PI));
```

```
    A.setY(sin(layer.getAngleAni()/180*M_PI)*sin(layer.
        getAngleAni2()/180*M_PI));
    A.setZ(cos(layer.getAngleAni()/180*M_PI));
    APlane.setX(0);
    APlane.setY(1);
    APlane.setZ(0);
    CosAni=A.dotProduct(layer.getMag());
    SinAni=sqrt(1-pow(CosAni,2));
    CosPlane=APlane.dotProduct(layer.getMag());
    //B.setX(sin(layer.getAngleAni()/180*M_PI)*sin(layer.
        getAngleAni2()/180*M_PI));
    //B.setY(sin(layer.getAngleAni()/180*M_PI)*sin(layer.
        getAngleAni2()/180*M_PI));
    //B.setZ(sin(layer.getAngleAni()/180*M_PI));

    x=Hk1*A.getX()*CosAni+Hk2*A.getX()*CosAni*pow(SinAni,2)
        +HkPlane*APlane.getX()*CosPlane;
    y=Hk1*A.getY()*CosAni+Hk2*A.getY()*CosAni*pow(SinAni,2)
        +HkPlane*APlane.getY()*CosPlane;
    z=Hk1*A.getZ()*CosAni+Hk2*A.getZ()*CosAni*pow(SinAni,2)
        +HkPlane*APlane.getZ()*CosPlane;
    //std::cout<<"Hy="<<HkPlane<<std::endl;
    /*x=Hk1*A.getX()*CosAni+Hk2*A.getX()*pow(CosAni,3);
    y=Hk1*A.getY()*CosAni+Hk2*A.getY()*pow(CosAni,3);
    z=Hk1*A.getZ()*CosAni+Hk2*A.getZ()*pow(CosAni,3);*/

}

AniVector3::~AniVector3()
{

}

//Careful cos(90) not equal to zero
```

Listing 12.5 – **DemagVector3.cpp**

```
#include "DemagVector3.h"

DemagVector3::DemagVector3(Layer layer)
{
  x=layer.getMag().getX()*layer.getMs()*(-1)*layer.getND().getX();
  y=layer.getMag().getY()*layer.getMs()*(-1)*layer.getND().getY();
  z=layer.getMag().getZ()*layer.getMs()*(-1)*layer.getND().getZ();
}

DemagVector3::~DemagVector3()
{

}
```

Listing 12.6 – **AloneTorque.cpp**

```
#include "AloneTorque.h"

#include "AniVector3.h"
#include "DemagVector3.h"
#include "HThermVector3.h"
#include "AppliedFieldVector3.h"
#include "Constants.h"

#include <cmath>
#include <iostream>

AloneTorque::AloneTorque(Clock clock,Pulse *field,Layer
    layer)
{
  newGamma=Constants::GAMMA/(1+pow(layer.getAlpha(),2));
  newAlpha=newGamma*layer.getAlpha();
  Vector3 torque1,torque2;
  heff=AniVector3(layer);
  //std::cout<<"ani="<<heff.getX()<<"=="<<heff.getY()
      <<"=="<<heff.getZ()<<std::endl;
  heff.add(DemagVector3(layer));
  //std::cout<<"+demag="<<heff.getX()<<"=="<<heff.getY()
      <<"=="<<heff.getZ()<<std::endl;
  //heff.add(HThermVector3(mag));
  heff.add(AppliedFieldVector3(clock,field));
  //std::cout<<"+applied="<<heff.getX()<<"=="<<heff.getY
      ()<<"=="<<heff.getZ()<<std::endl;
  torque1=layer.getMag();
  torque1.crossProduct(heff);
  torque2=layer.getMag();
  torque2.crossProduct(torque1);
  torque1.mult(-newGamma);
  torque2.mult(-newAlpha);
  torque1.add(torque2);
  x=torque1.getX();
  y=torque1.getY();
  z=torque1.getZ();
  //std::cout<<x<<"=="<<y<<"=="<<z<<std::endl;
}

AloneTorque::~AloneTorque()
{

}

//didn't take Htherm into account
```

Listing 12.7 – **SpinTorque.cpp**

```
#include "SpinTorque.h"

#include "Constants.h"
#include "Polarization.h"

#include <cmath>

SpinTorque::SpinTorque(Clock clock,Pulse * current,Layer
    mag,Layer pol,NewParameters params)
{
  double polarization=0;
  if(params.getPolarizationType()=="Slonczewski")
    {
      polarization=Polarization(mag,pol).Slonczewski(mag)
          ;
    }
  if(params.getPolarizationType()=="Xiao")
    {
      polarization=Polarization(mag,pol).Xiao(params);
    }
  Vector3 torque1,torque2;
  torque1=torque2=mag.getMag();
  double betatemp=(Constants::GAMMA*Constants::HBAR*
      current->getLevel(clock.getTimeStamp())*polarization
      )/(2*Constants::MU0*Constants::E*mag.getMs()*mag.
      getThickness()*mag.getSurface());
  newBeta2=betatemp/(1+pow(mag.getAlpha(),2));
  newBeta1=newBeta2*mag.getAlpha();
  torque1.crossProduct(pol.getMag());
  torque2.crossProduct(torque1);
  torque1.mult(newBeta1);
  torque2.mult(-newBeta2);
  torque1.add(torque2);
  x=torque1.getX();
  y=torque1.getY();
  z=torque1.getZ();
}

SpinTorque::~SpinTorque()
{

}
```

Listing 12.8 – **TotalTorque.cpp**

```
#include "TotalTorque.h"

#include "SpinTorque.h"
#include "AloneTorque.h"
#include "OtherTorque.h"

#include <iostream>

TotalTorque::TotalTorque(Clock clock,Pulse *field,Pulse *
    current,MultiLayer multiLayer,int layerNumber,
    NewParameters params)
{
  downBeta1=0;downBeta2=0;upBeta1=0;upBeta2=0;
  Torque torque1,torque2,torque3;
  torque3.setVector(0,0,0);
  torque1=AloneTorque(clock,field,multiLayer[layerNumber
      ]);
  if(multiLayer.getNbLayer()<3)
    {
      if(layerNumber==0)
        {
          torque2=SpinTorque(clock,current,multiLayer[
              layerNumber],multiLayer[layerNumber+1],
              params);
          torque3=OtherTorque(multiLayer[layerNumber],
              multiLayer[layerNumber+1]);
        }
      else
        {
          torque2=SpinTorque(clock,current,multiLayer[
              layerNumber],multiLayer[0],params);
          torque3=OtherTorque(multiLayer[layerNumber],
              multiLayer[0]);
        }
      torque1.add(torque2);
      torque1.add(torque3);
    }

  else if(multiLayer.getNbLayer()==3)
    {
      if(layerNumber>0) //Spin torque from below +
          exchange coupling
        {
          torque2=SpinTorque(clock,current,multiLayer[
              layerNumber],multiLayer[layerNumber-1],
              params);
          torque3=OtherTorque(multiLayer[layerNumber],
              multiLayer[layerNumber-1]);
```

```
          torque1.add(torque2);
          torque1.add(torque3);
          downBeta1=torque2.getBeta1();
          downBeta2=torque2.getBeta2();
        }
      if((layerNumber+1)<multiLayer.getNbLayer()) //Spin
         torque from above + exchange coupling
        {
          torque2=SpinTorque(clock,current,multiLayer[
             layerNumber],multiLayer[layerNumber+1],
             params);
          torque1.add(torque2);
          torque3=OtherTorque(multiLayer[layerNumber],
             multiLayer[layerNumber+1]);
          torque1.add(torque3);
          upBeta1=torque2.getBeta1();
          upBeta2=torque2.getBeta2();
        }
    }
  //Effective field is alone torque + other torque ie
     torque1 + torque 3
  heff=torque1.getHeff();
  heff.add(torque3.getHeff());

  newAlpha=torque1.getAlpha();
  newGamma=torque1.getGamma();
  newBeta1=torque2.getBeta1(); //only good for one free
     layer
  newBeta2=torque2.getBeta2(); //only good for one free
     layer

  x=torque1.getX();
  y=torque1.getY();
  z=torque1.getZ();
}

TotalTorque::~TotalTorque()
{

}

double TotalTorque::getUpBeta1()
{
  return upBeta1;
}

double TotalTorque::getDownBeta1()
{
  return downBeta1;
}
```

```
double TotalTorque::getUpBeta2()
{
  return upBeta2;
}

double TotalTorque::getDownBeta2()
{
  return downBeta2;
}
```

Listing 12.9 – **CreateLayer.cpp**

```
#include "CreateLayer.h"

#include "NewParameters.h"

#include <QString>
#include <QDataStream>
#include <QTextStream>
#include <iostream>
CreateLayer::CreateLayer(int i,NewParameters params)
{

    number=i;
    alpha=params.getSample()[i]["alpha"];
    thickness=params.getSample()[i]["thickness"];
    surface=params.getSample()[i]["surface"];
    k1=params.getSample()[i]["k1"];
    k2=params.getSample()[i]["k2"];
    kPlane=params.getSample()[i]["kPlane"];
    angleAni=params.getSample()[i]["aniTheta"];
    angleAni2=params.getSample()[i]["aniPhi"];
    frozen=params.getSample()[i]["frozen"];
    m.setX(params.getSample()[i]["mx"]);
    m.setY(params.getSample()[i]["my"]);
    m.setZ(params.getSample()[i]["mz"]);
    nd.setX(params.getSample()[i]["ndx"]);
    nd.setY(params.getSample()[i]["nd"]);
    nd.setZ(params.getSample()[i]["ndz"]);
    nr.setX(params.getSample()[i]["nrx"]);
    nr.setY(params.getSample()[i]["nry"]);
    nr.setZ(params.getSample()[i]["nrz"]);
    ms=params.getSample()[i]["ms"];
    upExchange=params.getSample()[i]["upExchange"];
    downExchange=params.getSample()[i]["downExchange"];
    polarization=params.getSample()[i]["polarization"];
    std::cout<<"layer␣pol"<<polarization<<std::endl;
}

CreateLayer::~CreateLayer()
{

}
```

Listing 12.10 – **MultiLayer.cpp**

```
#include "MultiLayer.h"

#include "CreateLayer.h"

MultiLayer::MultiLayer(NewParameters params)
{
  nbLayer=2;
  nbFreeLayer=0;
  for(int i=0;i<nbLayer;i++)
    {
      Layer temp=CreateLayer(i,params);
      push_back(temp);
      if(temp.getFrozen()==false)
        {
          nbFreeLayer++;
          solveLayer=i;
        }
    }
  //solveLayer=p->getInt("sLayer");
  if(nbLayer==1)
    {
      Layer temp;
      temp.setMag(0,0,1);
      push_back(temp);
    }
}

MultiLayer::~MultiLayer()
{

}

int MultiLayer::getSolveLayer()
{
  return solveLayer;
}

int MultiLayer::getNbLayer()
{
  return nbLayer;
}

int MultiLayer::getNbFreeLayer()
{
  return nbFreeLayer;
}
```

Listing 12.11 – **Polarization.cpp**

```cpp
#include "Polarization.h"

#include <cmath>

Polarization::Polarization(Layer mag,Layer pol)
{
  costheta=mag.getMag().dotProduct(pol.getMag());
}

Polarization::~Polarization()
{

}

double Polarization::Slonczewski(Layer mag)
{
  QTextStream cout(stdout,QIODevice::WriteOnly);
  double P=mag.getPolarization();
  //cout<<"p="<<P<<"cos="<<costheta<<endl;
  double g=-4+(pow((1+P),3)*(3+costheta)/(4*pow(P,1.5)));
  //cout<<"1/g="<<g<<endl;
  return 1/g;
}

double Polarization::Xiao(NewParameters params)
{
  double qplus=params.getPolarization()["qplus"];
  double qminus=params.getPolarization()["qminus"];
  double b0=params.getPolarization()["b0"];
  double b1=params.getPolarization()["b1"];
  double polarization=qplus/(b0+b1*costheta)-qminus/(b0-
      b1*costheta);
  return polarization;
}
```

Listing 12.12 – **OneLayerRungeKutta.cpp**

```
#include "OneLayerRungeKutta.h"

#include <iostream>
#include <gsl/gsl_errno.h>
#include <gsl/gsl_matrix.h>
#include <gsl/gsl_odeiv.h>

#include "Clock.h"

int llg (double t, const double y[], double f[], void *
    params)
{
  double *p=(double *)params;
  double alpha=p[0];
  double gamma=p[1];
  double beta1=p[2];
  double beta2=p[3];

  double heffx=p[4];
  double heffy=p[5];
  double heffz=p[6];

  double px=p[7];
  double py=p[8];
  double pz=p[9];

  double mx=y[0];
  double my=y[1];
  double mz=y[2];

  f[0]=-gamma*(my*heffz-mz*heffy)-alpha*((mx*mx-1)*heffx+
      mx*my*heffy+mx*mz*heffz)
    +beta1*(my*pz-mz*py)-beta2*((mx*mx-1)*px+mx*my*py+mx*
        mz*pz);
  f[1]=-gamma*(mz*heffx-mx*heffz)-alpha*((my*my-1)*heffy+
      mz*my*heffz+mx*my*heffx)
    +beta1*(mz*px-mx*pz)-beta2*((my*my-1)*py+mz*my*pz+mx*
        my*px);
  f[2]=-gamma*(mx*heffy-my*heffx)-alpha*((mz*mz-1)*heffz+
      mz*mx*heffx+mz*my*heffy)
    +beta1*(mx*py-my*px)-beta2*((mz*mz-1)*pz+mz*mx*px+mz*
        my*py);

  return GSL_SUCCESS;
}

int jac (double t, const double y[], double *dfdy, double
     dfdt[], void *params)
```

```
{
  double *p=(double *)params;
  double alpha=p[0];
  double gamma=p[1];
  double beta1=p[2];
  double beta2=p[3];

  double heffx=p[4];
  double heffy=p[5];
  double heffz=p[6];

  double px=p[7];
  double py=p[8];
  double pz=p[9];

  double mx=y[0];
  double my=y[1];
  double mz=y[2];

  gsl_matrix_view dfdy_mat
    = gsl_matrix_view_array (dfdy, 3, 3);
  gsl_matrix * m = &dfdy_mat.matrix;
  gsl_matrix_set(m,0,0,-alpha*(2*mx*heffx+my*heffy+mz*
      heffz)-beta2*(2*mx*px+my*py+mz*pz));
  gsl_matrix_set(m,0,1,-gamma*heffz-alpha*mx*heffy+beta1*
      pz-beta2*mx*py);
  gsl_matrix_set(m,0,2,gamma*heffy-alpha*mx*heffz-beta1*
      py-beta2*mx*pz);
  gsl_matrix_set(m,1,0,gamma*heffz-alpha*my*heffx-beta1*
      pz-beta2*my*px);
  gsl_matrix_set(m,1,1, -alpha*(2*my*heffy+mx*heffx+mz*
      heffz)-beta2*(2*my*py+mx*px+mz*pz));
  gsl_matrix_set(m,1,2,-gamma*heffx-alpha*my*heffz+beta1*
      px-beta2*my*pz);
  gsl_matrix_set(m,2,0,-gamma*heffy-alpha*mz*heffx+beta1*
      py-beta2*mz*px);
  gsl_matrix_set(m,2,1,gamma*heffx-alpha*mz*heffy-beta1*
      px-beta2*mz*py);
  gsl_matrix_set(m,2,2,-alpha*(2*mz*heffz+mx*heffx+my*
      heffy)-beta2*(2*mz*pz+my*py+mx*px));
  dfdt[0] = 0.0;
  dfdt[1] = 0.0;
  dfdt[2] = 0.0;
  return GSL_SUCCESS;
}

double* rungekutta(Torque torque,Layer pol,Vector3 mag,
    Clock clock)
{
```

```
double *arr=new double[3];

const gsl_odeiv_step_type * T
  = gsl_odeiv_step_rkck;

gsl_odeiv_step * s
  = gsl_odeiv_step_alloc (T, 3);
gsl_odeiv_control * c
  = gsl_odeiv_control_y_new (1E-5, 1);//first is max
      absolute error second is relative
gsl_odeiv_evolve * e
  = gsl_odeiv_evolve_alloc (3);

double alpha=torque.getAlpha();
double gamma=torque.getGamma();
double beta1=torque.getBeta1();
double beta2=torque.getBeta2();

double px=pol.getMag().getX();
double py=pol.getMag().getY();
double pz=pol.getMag().getZ();

double heffx=torque.getHeff().getX();
double heffy=torque.getHeff().getY();
double heffz=torque.getHeff().getZ();

double params[9];

gsl_odeiv_system system = {llg, jac, 3, params};

params[0]=alpha;
params[1]=gamma;
params[2]=beta1;
params[3]=beta2;
params[4]=heffx;
params[5]=heffy;
params[6]=heffz;
params[7]=px;
params[8]=py;
params[9]=pz;

double t = clock.getTimeStamp(), t1 = clock.
    getTimeStamp()+clock.getTimeStep(); //t=initial time
     t1=final time
double h = 1E-10; //initial stepsize

arr[0]=mag.getX();
arr[1]=mag.getY();
arr[2]=mag.getZ();
```

```
  while (t < t1)
    {
      int status = gsl_odeiv_evolve_apply (e,c,s,&system
          ,&t,t1,&h,arr);

      if (status != GSL_SUCCESS)
        break;

      mag.setX(arr[0]);
      mag.setY(arr[1]);
      mag.setZ(arr[2]);

    }

  gsl_odeiv_evolve_free (e);
  gsl_odeiv_control_free (c);
  gsl_odeiv_step_free (s);

  return arr;
}
```

Listing 12.13 – **TwoLayerRungeKutta.cpp**

```
#include "TwoLayerRungeKutta.h"

#include <iostream>
#include <gsl/gsl_errno.h>
#include <gsl/gsl_matrix.h>
#include <gsl/gsl_odeiv.h>

#include "SpinTorque.h"
#include "AloneTorque.h"
#include "NewParameters.h"

int llg3 (double t, const double y[], double f[], void *
    params)
{

    double *p=(double *)params;
    double alpha1=p[0];
    double gamma1=p[1];
    double alpha2=p[2];
    double gamma2=p[3];

    double beta1_1P=p[4];
    double beta2_1P=p[5];
    double beta1_12=p[6];
    double beta2_12=p[7];
    double beta1_21=p[8];
    double beta2_21=p[9];

    double heffx1=p[10];
    double heffy1=p[11];
    double heffz1=p[12];
    double heffx2=p[13];
    double heffy2=p[14];
    double heffz2=p[15];

    double px=p[16];
    double py=p[17];
    double pz=p[18];

    double mx1=y[0];
    double my1=y[1];
    double mz1=y[2];

    double mx2=y[3];
    double my2=y[4];
    double mz2=y[5];
```

```
  // m1 is between the pinned layer p and the free layer
      m2
  f[0]=-gamma1*(my1*heffz1-mz1*heffy1)-alpha1*((mx1*mx1
      -1)*heffx1+mx1*my1*heffy1+mx1*mz1*heffz1)
    +beta1_1P*(my1*pz-mz1*py)-beta2_1P*((mx1*mx1-1)*px+
        mx1*my1*py+mx1*mz1*pz)
    +beta1_12*(my1*mz2-mz1*my2)-beta2_12*((mx1*mx1-1)*mx2
        +mx1*my1*my2+mx1*mz1*mz2);
  f[1]=-gamma1*(mz1*heffx1-mx1*heffz1)-alpha1*((my1*my1
      -1)*heffy1+mz1*my1*heffz1+mx1*my1*heffx1)
    +beta1_1P*(mz1*px-mx1*pz)-beta2_1P*((my1*my1-1)*py+
        mz1*my1*pz+mx1*my1*px)
    +beta1_12*(mz1*mx2-mx1*mz2)-beta2_12*((my1*my1-1)*my2
        +mz1*my1*mz2+mx1*my1*mx2);
  f[2]=-gamma1*(mx1*heffy1-my1*heffx1)-alpha1*((mz1*mz1
      -1)*heffz1+mz1*mx1*heffx1+mz1*my1*heffy1)
    +beta1_1P*(mx1*py-my1*px)-beta2_1P*((mz1*mz1-1)*pz+
        mz1*mx1*px+mz1*my1*py)
    +beta1_12*(mx1*my2-my1*mx2)-beta2_12*((mz1*mz1-1)*mz2
        +mz1*mx1*mx2+mz1*my1*my2);
  //equations for third layer m2
  f[3]=-gamma2*(my2*heffz2-mz2*heffy2)-alpha2*((mx2*mx2
      -1)*heffx2+mx2*my2*heffy2+mx2*mz2*heffz2)
    +beta1_21*(my2*mz1-mz2*my1)-beta2_21*((mx2*mx2-1)*mx1
        +mx2*my2*my1+mx2*mz2*mz1);
  f[4]=-gamma2*(mz2*heffx2-mx2*heffz2)-alpha2*((my2*my2
      -1)*heffy2+mz2*my2*heffz2+mx2*my2*heffx2)
    +beta1_21*(mz2*mx1-mx2*mz1)-beta2_21*((my2*my2-1)*my1
        +mz2*my2*mz1+mx2*my2*mx1);
  f[5]=-gamma2*(mx2*heffy2-my2*heffx2)-alpha2*((mz2*mz2
      -1)*heffz2+mz2*mx2*heffx2+mz2*my2*heffy2)
    +beta1_21*(mx2*my1-my2*mx1)-beta2_21*((mz2*mz2-1)*mz1
        +mz2*mx2*mx1+mz2*my2*my1);

  return GSL_SUCCESS;
}

int jac3 (double t, const double y[], double *dfdy,
    double dfdt[], void *params)
{

  double *p=(double *)params;
  double alpha1=p[0];
  double gamma1=p[1];
  double alpha2=p[2];
  double gamma2=p[3];

  double beta1_1P=p[4];
  double beta2_1P=p[5];
  double beta1_12=p[6];
```

```
double beta2_12=p[7];
double beta1_21=p[8];
double beta2_21=p[9];

double heffx1=p[10];
double heffy1=p[11];
double heffz1=p[12];
double heffx2=p[13];
double heffy2=p[14];
double heffz2=p[15];

double px=p[16];
double py=p[17];
double pz=p[18];

double mx1=y[0];
double my1=y[1];
double mz1=y[2];

double mx2=y[3];
double my2=y[4];
double mz2=y[5];

gsl_matrix_view dfdy_mat
  = gsl_matrix_view_array (dfdy, 6, 6);
gsl_matrix * m = &dfdy_mat.matrix;
//df[0]
gsl_matrix_set(m,0,0,alpha1*(2*mx1*heffx1+my1*heffy1+
   mz1*heffz1)-beta2_1P*(mx1*2*px+my1*py+mz1*pz)
               -beta2_12*(2*mx1*mx2+my1*my2+mz1*mz2));
gsl_matrix_set(m,0,1,-gamma1*heffz1-alpha1*+mx1*heffy1+
   beta1_1P*pz-beta2_1P*+mx1*py+beta1_12*mz2-beta2_12*
   mx1*my2);
gsl_matrix_set(m,0,2,gamma1*heffy1-alpha1*+mx1*heffz1-
   beta1_1P*py-beta2_1P*mx1*pz-beta1_12*my2-beta2_12*
   mx1*mz2);
gsl_matrix_set(m,0,3,-beta2_12*(mx1*mx1-1));
gsl_matrix_set(m,0,4,-beta1_12*mz1-beta2_12*mx1*my1);
gsl_matrix_set(m,0,5,beta1_12*my1-beta2_12*mx1*mz1);
//df[1]
gsl_matrix_set(m,1,0,gamma1*heffz1+alpha1*my1*heffx1-
   beta1_1P*pz-beta2_1P*my1*px-beta1_12*mz2-beta2_12*
   my1*mx2);
gsl_matrix_set(m,1,1,-alpha1*(2*my1*heffy1+mz1*heffz1+
   mx1*heffx1)-beta2_1P*(2*my1*py+mz1*pz+mx1*px)
               -beta2_12*(2*my1*my2+mz1*mz2+mx1*mx2));
gsl_matrix_set(m,1,2,-gamma1*mz1*heffx1-alpha1*my1*
   heffz1+beta1_1P*px-beta2_1P*my1*pz
               +beta1_12*mx2-beta2_12*my1*mz2);
gsl_matrix_set(m,1,3,beta1_12*mz1-beta2_12*mx1*my1);
```

```
  gsl_matrix_set(m,1,4,-beta2_12*(my1*my1-1));
 gsl_matrix_set(m,1,5,-beta1_12*mx1-beta2_12*mz1*my1);
 //df[2]
  gsl_matrix_set(m,2,0,-gamma1*heffy1-alpha1*+mz1*heffx1+
     beta1_1P*py-beta2_1P*mz1*px+beta1_12*my2-beta2_12*
     mz1*mx2);
  gsl_matrix_set(m,2,1,gamma1*heffx1-alpha1*mz1*heffy1-
     beta1_1P*my1*px-beta2_1P*+mz1*py-beta1_12*mx2-
     beta2_12*mz1*my2);
  gsl_matrix_set(m,2,2,-alpha1*(2*mz1*heffz1+mx1*heffx1+
     my1*heffy1)-beta2_1P*(2*mz1*pz+mx1*px+my1*py)
                 -beta2_12*(2*mz1*mz2+mx1*mx2+my1*my2));
  gsl_matrix_set(m,2,3,-beta1_12*my1-beta2_12*mz1*mx1);
  gsl_matrix_set(m,2,4,beta1_12*mx1*my2-beta2_12*mz1*my1)
     ;
  gsl_matrix_set(m,2,5,-beta2_12*(mz1*mz1-1));
  //df[3]
  gsl_matrix_set(m,3,0,-beta2_21*(mx2*mx2-1));
  gsl_matrix_set(m,3,1,-beta1_21*-mz2-beta2_21*mx2*my2);
  gsl_matrix_set(m,3,2,beta1_21*my2*mz1-beta2_21*mx2*mz2)
     ;
  gsl_matrix_set(m,3,3,-alpha2*((2*mx2-1)*heffx2+my2*
     heffy2+mz2*heffz2)-beta2_21*((2*mx2-1)*mx1+my2*my1+
     mz2*mz1));
  gsl_matrix_set(m,3,4,-gamma2*heffz2-alpha2*mx2*heffy2+
     beta1_21*mz1-beta2_21*mx2*my1);
  gsl_matrix_set(m,3,5,gamma2*mz2*heffy2-alpha2*mx2*
     heffz2-beta1_21*my1-beta2_21*mx2*mz1);
  //df[4]
  gsl_matrix_set(m,4,0,beta1_21*mz2-beta2_21*mx2*my2);
  gsl_matrix_set(m,4,1,-beta2_21*(my2*my2-1));
  gsl_matrix_set(m,4,2,-beta1_21*mx2-beta2_21*mz2*my2);
  gsl_matrix_set(m,4,3,gamma2*heffz2-alpha2*my2*heffx2-
     beta1_21*mz1-beta2_21*my2*mx1);
  gsl_matrix_set(m,4,4,-alpha2*(2*my2*heffy2+mz2*heffz2+
     mx2*heffx2)-beta2_21*(2*my2*my1+mz2*mz1+mx2*mx1));
  gsl_matrix_set(m,4,5,-gamma2*mz2*heffx2-alpha2*+my2*
     heffz2+beta1_21*mx1-beta2_21*my2*mz1);
  //df[5]
 gsl_matrix_set(m,5,0,-beta1_21*my2-beta2_21*mz2*mx2);
  gsl_matrix_set(m,5,1,beta1_21*mx2-beta2_21*mz2*mx2);
  gsl_matrix_set(m,5,2,-beta2_21*(mz2*mz2-1));
  gsl_matrix_set(m,5,3,-gamma2*heffy2-alpha2*mz2*heffx2+
     beta1_21*my1-beta2_21*mz2*mx1);
 gsl_matrix_set(m,5,4,gamma2*heffx2-alpha2*mz2*heffy2-
    beta1_21*mx1-beta2_21*mz2*my1);
 gsl_matrix_set(m,5,5,alpha2*(2*mz2*heffz2+mx2*heffx2+my2
    *heffy2)-beta2_21*(2*mz2*mz1+mx2*mx1+my2*my1));

  dfdt[0] = 0.0;
```

```
  dfdt[1] = 0.0;
  dfdt[2] = 0.0;
  dfdt[3] = 0.0;
  dfdt[4] = 0.0;
  dfdt[5] = 0.0;

  return GSL_SUCCESS;
}

double* rungekutta3(Layer mag1,Layer mag2,Layer pol,
   Torque torque1,Torque torque2,Clock clock,Pulse *
   current,NewParameters parameters)
{

  Torque storque12,storque21,storque1P;
  storque12=SpinTorque(clock,current,mag1,mag2,parameters
     );
  storque21=SpinTorque(clock,current,mag2,mag1,parameters
     );
  storque1P=SpinTorque(clock,current,mag1,pol,parameters)
     ;

 double *arr=new double[6];

  const gsl_odeiv_step_type * T
    = gsl_odeiv_step_rkck;

  gsl_odeiv_step * s
    = gsl_odeiv_step_alloc (T, 6);
  gsl_odeiv_control * c
    = gsl_odeiv_control_y_new (1E-5, 1);//first is max
       absolute error second is relative
  gsl_odeiv_evolve * e
    = gsl_odeiv_evolve_alloc (6);

  double alpha1=torque1.getAlpha();
  double gamma1=torque1.getGamma();
  double alpha2=torque2.getAlpha();
  double gamma2=torque2.getGamma();

  double beta1_1P=storque1P.getBeta1();
  double beta2_1P=storque1P.getBeta2();
  double beta1_12=storque12.getBeta1();
  double beta2_12=storque12.getBeta2();
  double beta1_21=storque21.getBeta1();
  double beta2_21=storque21.getBeta2();

  double px=pol.getMag().getX();
  double py=pol.getMag().getY();
  double pz=pol.getMag().getZ();
```

```
double heffx1=torque1.getHeff().getX();
double heffy1=torque1.getHeff().getY();
double heffz1=torque1.getHeff().getZ();

double heffx2=torque2.getHeff().getX();
double heffy2=torque2.getHeff().getY();
double heffz2=torque2.getHeff().getZ();

double params[19];

gsl_odeiv_system system = {llg3, jac3, 6, params};

params[0]=alpha1;
params[1]=gamma1;
params[2]=alpha2;
params[3]=gamma2;
params[4]=beta1_1P;
params[5]=beta2_1P;
params[6]=beta1_12;
params[7]=beta2_12;
params[8]=beta1_21;
params[9]=beta2_21;
params[10]=heffx1;
params[11]=heffy1;
params[12]=heffz1;
params[13]=heffx2;
params[14]=heffy2;
params[15]=heffz2;
params[16]=px;
params[17]=py;
params[18]=pz;

double t = clock.getTimeStamp(), t1 = clock.
    getTimeStamp()+clock.getTimeStep(); //t=initial time
     t1=final time
double h = 1E-10; //initial stepsize

arr[0]=mag1.getMag().getX();
arr[1]=mag1.getMag().getY();
arr[2]=mag1.getMag().getZ();
arr[3]=mag2.getMag().getX();
arr[4]=mag2.getMag().getY();
arr[5]=mag2.getMag().getZ();

while (t < t1)
  {

    int status = gsl_odeiv_evolve_apply (e,c,s,&system
        ,&t,t1,&h,arr);
```

```
      if (status != GSL_SUCCESS)
        break;

      mag1.setMag(arr[0], arr[1], arr[2]);
      mag2.setMag(arr[3], arr[4], arr[5]);

    }

    gsl_odeiv_evolve_free (e);
    gsl_odeiv_control_free (c);
    gsl_odeiv_step_free (s);

  return arr;
}
```

Listing 12.14 – **LimTorqueCheck.cpp**

```
#include "LimTorqueCheck.h"

#include "Parameters.h"
#include "TotalTorque.h"

#include <cmath>
#include <iostream>

LimTorqueCheck::LimTorqueCheck(Clock clock,Pulse *field, Pulse *current,MultiLayer multiLayer,NewParameters params)
{
  double norm=0;
  Vector3 torque;
  int layerNumber=multiLayer.getSolveLayer();
  check=false;

  if(multiLayer[layerNumber].getFrozen()==false)
    {
      torque=TotalTorque(clock,field,current,multiLayer,layerNumber,params);
      norm=sqrt(torque.dotProduct(torque));
      //std::cout<<"torque"<<norm<<std::endl;
      if(norm>params.getTorque()["limit"])
        check=false;
      else check=true;
    }

}

LimTorqueCheck::~LimTorqueCheck()
{

}
```

Listing 12.15 – **TrajSimul.cpp**

```
#include "TrajSimul.h"

#include "EvolveAlgo.h"
#include "TrajSave.h"
#include "LimTorqueCheck.h"

#include <iostream>

TrajSimul::TrajSimul()
{

}

TrajSimul::~TrajSimul()
{

}

MultiLayer TrajSimul::solve(Clock clock,Output output,
    Pulse *field,Pulse *current,MultiLayer multiLayer,
    NewParameters params)
{
  // int layerNumber=multiLayer.getSolveLayer();
  std::cout<<"H="<<field->getLevel(clock.getTimeStamp())
      <<std::endl;
  std::cout<<"I="<<current->getLevel(clock.getTimeStamp()
      )<<std::endl;
  Check limtorque;

  TrajSave().init(output,multiLayer);
  for(clock.setTimeStamp(0);clock.getTimeStamp()<clock.
      getTimeWindow();clock.setTimeStamp(clock.
      getTimeStamp()+clock.getTimeStep()))
    {
      if(clock.getTimeStep()>clock.getMaxTimeStep())
        {
          clock.setTimeStep(clock.getMaxTimeStep());
        }
      MultiLayer result=EvolveAlgo().solve(clock,field,
          current,multiLayer,params);
      multiLayer=result;
      //std::cout<<"trajsimul:"<<multiLayer[0].getMag().
          getZ()<<std::endl;
      TrajSave().save(clock,output,field,current,
          multiLayer);
      limtorque=LimTorqueCheck(clock,field,current,
          multiLayer,params);
      if (limtorque.getCheck()==true)
```

```
        {
          //std::cout<<"limtorque!\n"<<std::endl;
          return multiLayer;
        }
    }
  return multiLayer;

}
```

Listing 12.16 – **TrajMeanSimul.cpp**

```
#include "TrajMeanSimul.h"

#include "EvolveAlgo.h"
#include "TrajSave.h"
#include "LimTorqueCheck.h"

#include <iostream>

TrajMeanSimul::TrajMeanSimul()
{

}

TrajMeanSimul::~TrajMeanSimul()
{

}

MultiLayer TrajMeanSimul::solve(Clock clock,Output output
    ,Pulse *field,Pulse *current,MultiLayer multiLayer,
    NewParameters params)
{
  int layerNumber=multiLayer.getSolveLayer();
  std::cout<<"H="<<field->getLevel(clock.getTimeStamp())
      <<std::endl;
  std::cout<<"I="<<current->getLevel(clock.getTimeStamp()
      )<<std::endl;
  Check limtorque;

  TrajSave().init(output,multiLayer);
  for(clock.setTimeStamp(0);clock.getTimeStamp()<clock.
      getTimeWindow()-1E-9;clock.setTimeStamp(clock.
      getTimeStamp()+clock.getTimeStep()))
    {
      if(clock.getTimeStep()>clock.getMaxTimeStep())
        {
          clock.setTimeStep(clock.getMaxTimeStep());
        }
      MultiLayer result=EvolveAlgo().solve(clock,field,
          current,multiLayer,params);
      multiLayer=result;
      //std::cout<<"trajsimul:"<<multiLayer[1].getMag().
          getZ()<<std::endl;
      TrajSave().save(clock,output,field,current,
          multiLayer);
      limtorque=LimTorqueCheck(clock,field,current,
          multiLayer,params);
      if (limtorque.getCheck()==true)
```

```
        return multiLayer;
    }
  double counter=0;
  Vector3 averageMag;
  averageMag.setVector(0,0,0);
  while(clock.getTimeStamp()<clock.getTimeWindow())
    {
      if(clock.getTimeStep()>clock.getMaxTimeStep())
        clock.setTimeStep(clock.getMaxTimeStep());
      MultiLayer result=EvolveAlgo().solve(clock,field,
          current,multiLayer,params);
      multiLayer=result;
      averageMag.add(multiLayer[layerNumber].getMag());
      clock.setTimeStamp(clock.getTimeStamp()+clock.
          getTimeStep());
      counter++;
    }
  averageMag.mult(1/counter);
  multiLayer[layerNumber].setMag(averageMag);
  TrajSave().save(clock,output,field,current,multiLayer);
  return multiLayer;

}
```

Listing 12.17 – **LoopSimul.cpp**

```
#include "LoopSimul.h"

#include "TrajSimul.h"
#include "LoopSave.h"

#include <iostream>

LoopSimul::LoopSimul()
{

}

LoopSimul::~LoopSimul()
{

}

MultiLayer LoopSimul::solve(Clock clock,Output output,
    Pulse *field,Pulse *current,MultiLayer multiLayer,
    NewParameters params)
{
  LoopSave().initSave(output);
  Vector3 downMag=multiLayer[multiLayer.getSolveLayer()].
      getMag();
  MultiLayer downMultiLayer=multiLayer;
  downMag.mult(-1);
  downMultiLayer[multiLayer.getSolveLayer()].setMag(
      downMag);
  for(field->setLevel(params.getField()["min"]);field->
      getLevel(clock.getTimeStamp())<=params.getField()["
      max"];field->setLevel(field->getLevel(clock.
      getTimeStamp())+params.getField()["step"]))
    {
      output.setSave(false);
      MultiLayer result=TrajSimul().solve(clock,output,
          field,current,multiLayer,params);
      LoopSave().save(clock,output,field,current,result);
      double angle;
      angle=acos(result[multiLayer.getSolveLayer()].
          getMag().getZ());
      angle+=0.5*M_PI/180;
      //Vector3 smallAngle;
      //smallAngle.setVector(0,0,0);
      //smallAngle.add(result[multiLayer.getSolveLayer()
          ].getMag());
      //multiLayer[multiLayer.getSolveLayer()].setMag(
          smallAngle);
```

```
        multiLayer[multiLayer.getSolveLayer()].setMag(0,sin
            (angle),cos(angle));
      }
    for(field->setLevel(params.getField()["max"]);field->
        getLevel(clock.getTimeStamp())>=params.getField()["
        min"];field->setLevel(field->getLevel(clock.
        getTimeStamp())-params.getField()["step"]))
      {
        output.setSave(false);
        MultiLayer result=TrajSimul().solve(clock,output,
            field,current,multiLayer,params);
        LoopSave().save(clock,output,field,current,result);
        double angle;
        angle=acos(result[multiLayer.getSolveLayer()].
            getMag().getZ());
        angle+=0.5*M_PI/180;
        //Vector3 smallAngle;
        //smallAngle.setVector(0,0,0);
        //smallAngle.add(result[multiLayer.getSolveLayer()
            ].getMag());
        //multiLayer[multiLayer.getSolveLayer()].setMag(
            smallAngle);
        multiLayer[multiLayer.getSolveLayer()].setMag(0,sin
            (angle),cos(angle));
      }

    return multiLayer;
  }
```

Listing 12.18 – **AstroidSimul.cpp**

```
#include "AstroidSimul.h"

#include "CoerciveFieldAlgo.h"
#include "AstroidSave.h"
#include "Output.h"
#include "TrajSimul.h"
#include "NewParameters.h"

#include <string>
#include <sstream>
#include <iostream>
#include <cmath>

using namespace std;

AstroidSimul::AstroidSimul()
{

}

AstroidSimul::~AstroidSimul()
{

}

MultiLayer AstroidSimul::solve(Clock clock,Output output,
    Pulse *field,Pulse *current,MultiLayer multiLayer,
    NewParameters params)
{
  int layerNumber=multiLayer.getSolveLayer();
  output.setSave(false);
  AstroidSave().initialize(output);
  MultiLayer downMultiLayer=multiLayer;
  Vector3 downMag=multiLayer[layerNumber].getMag();
  downMag.mult(-1);
  downMultiLayer[layerNumber].setMag(downMag);

  for(field->setLevel(params.getField()["min"]);field->
      getLevel(clock.getTimeStamp())<=params.getField()["
      max"];field->setLevel(params.getField()["step"]+
      field->getLevel(clock.getTimeStamp())))
    {
      for(field->setAngle(params.getField()["thetaMin"]);
          field->getAngle()<=params.getField()["thetaMax"
          ];field->setAngle(field->getAngle()+params.
          getField()["thetaStep"]))
        {
          double smallAngle;
```

```
          //smallAngle = acos(multiLayer[layerNumber].
              getMag().getZ());
          //smallAngle+=0.5*M_PI/180;
          //multiLayer[layerNumber].setMag(0,sin(
              smallAngle),cos(smallAngle));
          MultiLayer up=TrajSimul().solve(clock,output,
              field,current,multiLayer,params);

          /*smallAngle = acos(downMultiLayer[layerNumber
              ].getMag().getZ());
          smallAngle+=0.5*M_PI/180;
          downMultiLayer[layerNumber].setMag(0,sin(
              smallAngle),cos(smallAngle));*/
          MultiLayer down=TrajSimul().solve(clock,output,
              field,current,downMultiLayer,params);
          downMag=down[layerNumber].getMag();
          downMag.add(up[layerNumber].getMag());
          downMag.mult(0.5);
          up[layerNumber].setMag(downMag.getX(),downMag.
              getY(),downMag.getZ());
          AstroidSave().save(clock,output,field,up[
              layerNumber]);
        }
    }
  return multiLayer;
}
```

Listing 12.19 – **PhDSimul.cpp**

```
#include "PhDSimul.h"

#include "TrajSimul.h"

#include "PhDSave.h"

#include <QFile>
#include <QTextStream>
#include <QString>

PhDSimul::PhDSimul()
{

}

PhDSimul::~PhDSimul()
{

}

MultiLayer PhDSimul::solve(Clock clock,Output output,
    Pulse *field,Pulse *current,MultiLayer multiLayer,
    NewParameters params)
{
  QTextStream cout(stdout,QIODevice::WriteOnly);

  //creates another layer with reverse magnetization
  MultiLayer downMultiLayer=multiLayer;
  int layerNumber=multiLayer.getSolveLayer();
  MultiLayer mup=multiLayer;
  MultiLayer mdown=multiLayer;
  QString filename;
  Vector3 tempVector;
  tempVector=multiLayer[layerNumber].getMag();
  tempVector.mult(-1);
  downMultiLayer[layerNumber].setMag(tempVector);
  PhDSave().initSave(output);

  for(current->setLevel(params.getCurrent()["min"]);
      current->getLevel(clock.getTimeStamp())<=params.
      getCurrent()["max"];current->setLevel(current->
      getLevel(clock.getTimeStamp())+params.getCurrent()["
      step"]))
    {
      for(field->setLevel(params.getField()["min"]);field
          ->getLevel(clock.getTimeStamp())<=params.
          getField()["max"];field->setLevel(field->
          getLevel(clock.getTimeStamp())+params.getField()
```

```
         ["step"]))
        {
          int nrun;
          Vector3 meanmag;
          meanmag.setVector(0,0,0);
          if(params.getTemperature()==0)
            nrun=1;
          for(int counter=0;counter<nrun;counter++)
            {
              output.setSave(false);
              mup=TrajSimul().solve(clock,output,field,
                  current,multiLayer,params);
              meanmag.add(mup[layerNumber].getMag());
            }
          meanmag.mult(1/nrun);
          mup[layerNumber].setMag(meanmag);
          filename=output.getFileName();
          filename.append("_up");
          output.setPhDFile(filename);
          PhDSave().save(output,mup[layerNumber]);
          filename=output.getFileName();
          filename.append("_down");
          meanmag.setX(0);meanmag.setY(0);meanmag.setZ(0)
              ;
          for(int counter=0;counter<nrun;counter++)
            {
              output.setSave(false);
              mdown=TrajSimul().solve(clock,output,field,
                  current,downMultiLayer,params);
              meanmag.add(mdown[layerNumber].getMag());
            }
          meanmag.mult(1/nrun);
          mdown[layerNumber].setMag(meanmag);
          output.setPhDFile(filename);
          PhDSave().save(output,mdown[layerNumber]);
          filename=output.getFileName();
          filename.append("_diff");
          output.setPhDFile(filename);
          MultiLayer mtemp=mdown;
          tempVector=mtemp[layerNumber].getMag();
          tempVector.mult(-1);
          tempVector.add(mup[layerNumber].getMag());
          mtemp[layerNumber].setMag(tempVector);
          PhDSave().save(output,mtemp[layerNumber]);
          filename=output.getFileName();
          filename.append("_sum");
          output.setPhDFile(filename);
          tempVector=mdown[layerNumber].getMag();
          tempVector.add(mup[layerNumber].getMag());
          tempVector.mult(0.5);
```

```
            mup[layerNumber].setMag(tempVector);
            PhDSave().save(output,mup[layerNumber]);
          }

        //to go to a new row
        filename=output.getFileName();
        filename.append("_up");
        output.setPhDFile(filename);
        PhDSave().save(output,"\n");
        filename=output.getFileName();
        filename.append("_down");
        output.setPhDFile(filename);
        PhDSave().save(output,"\n");
        filename=output.getFileName();
        filename.append("_diff");
        output.setPhDFile(filename);
        PhDSave().save(output,"\n");
        filename=output.getFileName();
        filename.append("_sum");
        output.setPhDFile(filename);
        PhDSave().save(output,"\n");
      }
    return multiLayer;
  }
```

Listing 12.20 – **SwitchingCheck.cpp**

```
#include "SwitchingCheck.h"

#include <QTextStream>

SwitchingCheck::SwitchingCheck(Layer layer,double tol)
{
  QTextStream cout(stdout,QIODevice::WriteOnly);
  //returns true if mag is withing swtiched mag tolerance
  //return false otherwise
  cout<<"switched_mag:"<<layer.getSwitchedMag().getX()<<
      layer.getSwitchedMag().getY()<<layer.getSwitchedMag
      ().getZ()<<endl;
  if((layer.getSwitchedMag().getX()-(tol/100)<layer.
      getMag().getX() && layer.getMag().getX()<layer.
      getSwitchedMag().getX()+(tol/100))&&
     (layer.getSwitchedMag().getY()-(tol/100)<layer.
         getMag().getY() && layer.getMag().getY()<layer.
         getSwitchedMag().getY()+(tol/100))&&
     (layer.getSwitchedMag().getZ()-(tol/100)<layer.
         getMag().getZ() && layer.getMag().getZ()<layer.
         getSwitchedMag().getZ()+(tol/100)))
    {
      //std::cout<<"switching"<<std::endl;
      check=true;
    }
  else
    {
      check=false;
      //std::cout<<"not switching"<<std::endl;
    }

}


SwitchingCheck::~SwitchingCheck()
{

}
```

Listing 12.21 – **ICritAlgo.cpp**

```
#include "ICritAlgo.h"

#include "TrajSimul.h"
#include "SwitchingCheck.h"

#include <cmath>
#include <iostream>

ICritAlgo::ICritAlgo()
{

}

ICritAlgo::~ICritAlgo()
{

}

double ICritAlgo::solve(Clock clock,Output output,Pulse *
    field,Pulse *current,MultiLayer multiLayer,
    NewParameters params)
{

  int run=params.getNrun();
  if(params.getTemperature()==0)
    run=1;
  double proba=0,nrun=0,nswitch=0;
  double iCritmax=params.getCurrent()["max"];
  double iCritmin=params.getCurrent()["min"];
  double iStep=params.getCurrent()["step"];
  MultiLayer result=multiLayer;
  bool bmin,bmax;
  current->setLevel(iCritmin);
  for(nrun=0;nrun<run;nrun++)
    {
      result=TrajSimul().solve(clock,output,field,current
          ,multiLayer,params);
      bmin=SwitchingCheck(result[multiLayer.getSolveLayer
          ()],params.getTorque()["tolerance"]).getCheck();
      if(bmin)
        {
          nswitch++;
          std::cout<<"switching"<<std::endl;
        }
      else std::cout<<"not␣switching"<<std::endl;
    }
  proba=nswitch/run;
  if(proba>=0.5)
```

```
    bmin=true;
  else bmin=false;
  //std::cout<<"switching"<<std::endl;
  //else std::cout<<"not switching"<<std::endl;
  //std::cout<<"imin :"<<proba<<std::endl;
  nswitch=0;
  current->setLevel(iCritmax);
  for(nrun=0;nrun<run;nrun++)
    {
      result=TrajSimul().solve(clock,output,field,current,multiLayer,params);
      bmax=SwitchingCheck(result[multiLayer.getSolveLayer()],params.getTorque()["tolerance"]).getCheck();
      if(bmax)
        {
          nswitch++;
          std::cout<<"switching"<<std::endl;
        }
      else std::cout<<"not␣switching"<<std::endl;
    }
  proba=nswitch/run;
  if(proba>=0.5)
    bmax=true;
  else bmax=false;
  //std::cout<<"imin :"<<proba<<std::endl;
 if(!bmin||bmax)
    {
      std::cout<<"bmax␣ou␣!bmin"<<std::endl;
      return 0;
    }
 while(fabs(iCritmax-iCritmin)>iStep)
    {
      bool btemp;
      double iTemp=(iCritmax+iCritmin)/2;
      current->setLevel(iTemp);
      nswitch=0;
      for(nrun=0;nrun<run;nrun++)
        {
          result=TrajSimul().solve(clock,output,field,current,multiLayer,params);
          btemp=SwitchingCheck(result[multiLayer.getSolveLayer()],params.getTorque()["tolerance"]).getCheck();
          if(btemp) nswitch++;
        }
      proba=nswitch/run;
      if(proba>=0.5)
        btemp=true;
      else btemp=false;
      if(btemp&&bmin)
```

```
            {
               iCritmin=iTemp;
               bmin=true;
            }
         if(!btemp&&!bmax)
            {
               iCritmax=iTemp;
               bmax=false;
            }
      }
   return iCritmin;
}
```

Listing 12.22 – **CoerciveFieldAlgo.cpp**

```
#include "CoerciveFieldAlgo.h"

#include "TrajSimul.h"
#include "SwitchingCheck.h"

#include <cmath>
#include <iostream>

CoerciveFieldAlgo::CoerciveFieldAlgo()
{

}

CoerciveFieldAlgo::~CoerciveFieldAlgo()
{

}

double CoerciveFieldAlgo::solve(Clock clock,Output output
    ,Pulse *field,Pulse *current,MultiLayer multiLayer)
{
  Parameters *p=Parameters::getInstance();
  int layerNumber=multiLayer.getSolveLayer();
  int run=p->getInt("nrun");
  if(p->getDouble("temperature")==0)
    run=1;
  double proba=0,nrun=0,nswitch=0;
  double bCritmax=p->getDouble("maxField");
  double bCritmin=p->getDouble("minField");
  double bStep=p->getDouble("fieldStep");
  MultiLayer result;
  bool bmin,bmax;
  field->setLevel(bCritmax);
  MultiLayer tempLayer=TrajSimul().solve(clock,output,
      field,current,multiLayer);
  multiLayer[layerNumber].setMag(tempLayer[layerNumber].
      getMag());
  field->setLevel(bCritmin);
  tempLayer=TrajSimul().solve(clock,output,field,current,
      multiLayer);
  multiLayer[layerNumber].setSwitchedMag(tempLayer[
      layerNumber].getMag());
  std::cout<<multiLayer[layerNumber].getMag().getZ()<<"==
      "<<multiLayer[layerNumber].getSwitchedMag().getZ()<<
      std::endl;
  if(multiLayer[layerNumber].getMag().getZ()==multiLayer[
      layerNumber].getSwitchedMag().getZ())
    return 0;
```

```
 for(nrun=0;nrun<run;nrun++)
   {
     result=TrajSimul().solve(clock,output,field ,current
         ,multiLayer);
     bmin=SwitchingCheck(result[layerNumber]).getCheck()
         ;
     if(bmin) nswitch++;
   }
 proba=nswitch/run;
 if(proba>=0.5)
   bmin=true;
 else bmin=false;
     //std::cout<<"switching"<<std::endl;
     //else std::cout<<"not switching"<<std::endl;
 std::cout<<"bmin␣:"<<proba<<std::endl;
 nswitch=0;
 field->setLevel(bCritmax);
 for(nrun=0;nrun<run;nrun++)
   {
     result=TrajSimul().solve(clock,output,field ,current
         ,multiLayer);
     bmax=SwitchingCheck(result[layerNumber]).getCheck()
         ;
     if(bmax) nswitch++;
     //std::cout<<"switching"<<std::endl;
     //else std::cout<<"not switching"<<std::endl;
   }
 proba=nswitch/run;
 if(proba>=0.5)
   bmax=true;
 else bmax=false;
std::cout<<"imin␣:"<<proba<<std::endl;
if(!bmin||bmax)
   {
     std::cout<<"bmax␣ou␣!bmin"<<std::endl;
     return 0;
   }
while(fabs(bCritmax-bCritmin)>bStep)
   {
     bool btemp;
     double bTemp=(bCritmax+bCritmin)/2;
     field->setLevel(bTemp);
     nswitch=0;
     for(nrun=0;nrun<run;nrun++)
       {
         result=TrajSimul().solve(clock,output,field ,
             current ,multiLayer);
         btemp=SwitchingCheck(result[layerNumber]).
             getCheck();
         if(btemp) nswitch++;
```

```
        }
      proba=nswitch/run;
      if(proba>=0.5)
        btemp=true;
      else btemp=false;
      if(btemp&&bmin)
        {
          bCritmin=bTemp;
          bmin=true;
        }
      if(!btemp&&!bmax)
        {
          bCritmax=bTemp;
          bmax=false;
        }
    }
  return bCritmax;
}
```

Listing 12.23 – **Parameters.xml**

```
<Parameters>
 <Time timeStep="4,999999980020986e-13" maxTimeStep="
     1,000000013351432e-10" timeWindow="5,000000058430487e
     -08"/>
 <Current value="-0,00100000047497451" min="
     -0,6000000238418579" step="0,00100000047497451" max=
     "0"/>
 <Field>
  <values value="0,1000000014901161" min="-500" step="100
      " max="500"/>
  <theta value="0" min="0" step="0" max="0"/>
  <phi value="90" min="0" step="0" max="0"/>
 </Field>
 <CurrentPulse>
  <pulse numberOfPulses="1" type="square"/>
  <length value="1,999999943436137e-09" min="
      1,000000013351432e-10" step="4,999999858590343e-10"
      max="4,999999969612645e-09"/>
 </CurrentPulse>
 <FieldPulse>
  <pulse numberOfPulses="1" type="nopulse"/>
  <length value="4,999999969612645e-09" min="
      1,000000013351432e-10" step="1,000000013351432e-10"
      max="1,999999987845058e-08"/>
 </FieldPulse>
 <DoublePulse>
  <first length="1,999999943436137e-09" amplitude="
      0,01200000010430813"/>
  <second length="7,999999773744548e-09" amplitude="
      0,01200000010430813" min="0" step="0" max="0"/>
  <delay value="5,999999941330714e-10" min="0" step="0"
      max="0"/>
 </DoublePulse>
 <Temperature value="0" nrun="1"/>
 <Torque tolerance="1" relAccuracy="0" limTorque="10"/>
 <polarization b0="1" b1="0,5" qplus="1" type="
     Slonczewski" qminus="0"/>
 <Sample>
  <Layer0>
   <material ms="500000" alpha="0,01" polarization="0,28"
       />
   <anisotropy k="3000000" theta="0" phi="90"/>
   <geometry thickness="1,800000037910365e-09" surface="
       9,9999998245167e-15"/>
   <exchange down="0" up="0"/>
   <layer number="1" frozen="1"/>
   <magnetization>
    <values x="0" y="0" z="1"/>
```

```
        <angle initial="0" step="0" final="0"/>
      </magnetization>
      <demagnetizationTensor>
        <self x="0" y="0" z="1"/>
        <mutual x="0" y="0" z="0"/>
      </demagnetizationTensor>
    </Layer0>
    <Layer1>
      <material ms="650000" alpha="0,009999999776482582"
          polarization="0,2800000011920929"/>
      <anisotropy k="330000" theta="0" phi="90"/>
      <geometry thickness="1,800000037910365e-09" surface="
          9,9999998245167e-15"/>
      <exchange down="0" up="0"/>
      <layer number="1" frozen="0"/>
      <magnetization>
        <values x="0" y="0,009999999776482582" z="
            0,9900000095367432"/>
        <angle initial="5" step="0" final="0"/>
      </magnetization>
      <demagnetizationTensor>
        <self x="0" y="0" z="1"/>
        <mutual x="0" y="0" z="0"/>
      </demagnetizationTensor>
    </Layer1>
  </Sample>
</Parameters>
```

Bibliographie

[1] M. N. Baibich, J. M. Broto, A. Fert, F. Nguyen Van Dau, F. Petroff, P. Etienne, G. Creuzet, A. Friederich, and J. Chazelas. Giant magnetoresistance of (001)fe/(001)cr magnetic superlattices. *Phys. Rev. Lett.*, 61 :2472–2475, Nov 1988. `http://link.aps.org/doi/10.1103/PhysRevLett.61.2472`.

[2] G. Binasch, P. Grünberg, F. Saurenbach, and W. Zinn. Enhanced magnetoresistance in layered magnetic structures with antiferromagnetic interlayer exchange. *Phys. Rev. B*, 39 :4828–4830, Mar 1989. `http://link.aps.org/doi/10.1103/PhysRevB.39.4828`.

[3] Jeffrey R. Childress and Robert E. Fontana Jr. Magnetic recording read head sensor technology. *Comptes Rendus Physique*, 6(9) :997 – 1012, 2005. `http://www.sciencedirect.com/science/article/pii/S1631070505001684`.

[4] I. R. McFadyen, E. E. Fullerton, and M. J. Carey. State-of-the-art magnetic hard disk drives. *MRS Bull*, 31(5) :379–383, 2006. `http://journals.cambridge.org/action/displayAbstract?fromPage=online&aid=7962837&fulltextType=RA&fileId=S0883769400010447`.

[5] J. M. Slaughter, R. W. Dave, M. DeHerrera, M. Durlam, B. N. Engel, J. Janesky, N. D. Rizzo, and S. Tehrani. Fundamentals of mram technology. *Journal of Superconductivity*, 15 :19–25, 2002. `http://dx.doi.org/10.1023/A:1014018925270`.

[6] J. C. Slonczewski. Current-driven excitation of magnetic multilayers. *Journal of Magnetism and Magnetic Materials*, 159(1-2) :L1 – L7, 1996. `http://www.sciencedirect.com/science/article/pii/0304885396000625`.

[7] L. Berger. Emission of spin waves by a magnetic multilayer traversed by a current. *Phys. Rev. B*, 54 :9353–9358, Oct 1996. `http://link.aps.org/doi/10.1103/PhysRevB.54.9353`.

[8] J. A. Katine, F. J. Albert, R. A. Buhrman, E. B. Myers, and D. C. Ralph. Current-driven magnetization reversal and spin-wave excitations in co /cu /co pillars. *Phys. Rev. Lett.*, 84 :3149–3152, Apr 2000. `http://link.aps.org/doi/10.1103/PhysRevLett.84.3149`.

[9] M. Tsoi, A. G. M. Jansen, J. Bass, W.-C. Chiang, M. Seck, V. Tsoi, and P. Wyder. Excitation of a magnetic multilayer by an electric current.

Phys. Rev. Lett., 80 :4281–4284, May 1998. http://link.aps.org/doi/10.1103/PhysRevLett.80.4281.

[10] M. Tsoi, A. G. M. Jansen, J. Bass, W.-C. Chiang, V. Tsoi, and P. Wyder. Generation and detection of phase-coherent current-driven magnons in magnetic multilayers. *Nature*, 406 :46–48, 2000. http://dx.doi.org/10.1038/35017512.

[11] J. Grollier, P. Boulenc, V. Cros, A. Hamzić, A. Vaurès, A. Fert, and G. Faini. Switching a spin valve back and forth by current-induced domain wall motion. *Applied Physics Letters*, 83(3) :509–511, 2003. http://link.aip.org/link/?APL/83/509/1.

[12] J.A. Katine and Eric E. Fullerton. Device implications of spin-transfer torques. *Journal of Magnetism and Magnetic Materials*, 320(7) :1217 – 1226, 2008. http://www.sciencedirect.com/science/article/pii/S0304885307010189.

[13] S. I. Kiselev, J. C. Sankey, I. N. Krivorotov, N. C. Emley, R. J. Schoelkopf, R. A. Buhrman, and D. C. Ralph. Microwave oscillations of a nanomagnet driven by a spin-polarized current. *Nature*, 425 :380 – 383, 2003. http://dx.doi.org/10.1038/nature01967.

[14] W. H. Rippard, M. R. Pufall, S. Kaka, S. E. Russek, and T. J. Silva. Direct-current induced dynamics in $co_{90}fe_{10}/ni_{80}fe_{20}$ point contacts. *Phys. Rev. Lett.*, 92 :027201, Jan 2004. http://link.aps.org/doi/10.1103/PhysRevLett.92.027201.

[15] Stuart S. P. Parkin, Masamitsu Hayashi, and Luc Thomas. Magnetic domain-wall racetrack memory. *Science*, 320(5873) :190–194, 2008. http://www.sciencemag.org/content/320/5873/190.abstract.

[16] L Néel. Théorie du traînage magnétique des ferromagnétiques en grains fins avec applications aux terres cuites. *Ann. géophys.*, 1949.

[17] J. Z. Sun. Spin-current interaction with a monodomain magnetic body : A model study. *Phys. Rev. B*, 62 :570–578, Jul 2000. http://link.aps.org/doi/10.1103/PhysRevB.62.570.

[18] D. Bedau, H. Liu, J.-J. Bouzaglou, A. D. Kent, J. Z. Sun, J. A. Katine, E. E. Fullerton, and S. Mangin. Ultrafast spin-transfer switching in spin valve nanopillars with perpendicular anisotropy. *Applied Physics Letters*, 96(2) :022514, 2010. http://link.aip.org/link/?APL/96/022514/1.

[19] D. Bedau, H. Liu, J. Z. Sun, J. A. Katine, E. E. Fullerton, S. Mangin, and A. D. Kent. Spin-transfer pulse switching : From the dynamic to the thermally activated regime. *Applied Physics Letters*, 97(26) :262502, 2010. http://link.aip.org/link/?APL/97/262502/1.

[20] S. Mangin, D. Ravelosona, JA Katine, MJ Carey, BD Terris, and E.E. Fullerton. Current-induced magnetization reversal in nanopillars with perpendicular anisotropy. *Nature Materials*, 5(3) :210–215, 2006. http://www.nature.com/nmat/journal/v5/n3/full/nmat1595.html.

[21] T. Seki, S. Mitani, K. Yakushiji, and K. Takanashi. Spin-polarized current-induced magnetization reversal in perpendicularly magnetized l1[sub 0]-fept layers. *Applied Physics Letters*, 88(17) :172504, 2006. http://link.aip.org/link/?APL/88/172504/1.

[22] E. Du Trémolet de Lacheisserie. *Magnétisme : Fondements*. Number vol. 1 à 2 in Collection Grenoble Sciences. EDP Sciences, 1999.

[23] Matthias Gottwald. *Nouveaux systÃ¨mes modÃ¨les Ã aimantation perpendiculaire pour l'Ã©tude des effets de transfert de spin*. PhD thesis, Université de Lorraine, 2011.

[24] E. C. Stoner and E. P. Wohlfarth. A mechanism of magnetic hysteresis in heterogeneous alloys. *Philosophical Transactions of the Royal Society of London. Series A, Mathematical and Physical Sciences*, 240(826) :599–642, 1948. http://rsta.royalsocietypublishing.org/content/240/826/599.abstract.

[25] L. Landau and E Lifschitz. On the theory of the dispersion of magnetic permeability in ferromagnetic bodies. *Phys. Z. Sowjetunion*, 8 :153–169, 1935. http://www.ujp.bitp.kiev.ua/files/file/papers/53/special_issue/53SI06p.pdf.

[26] Gilbert. 1956.

[27] W. Thomson. On the electro-dynamic qualities of metals :–effects of magnetization on the electric conductivity of nickel and of iron. *Proceedings of the Royal Society of London*, 8 :546–550, 1856. http://www.jstor.org/stable/111415.

[28] T. McGuire and R. Potter. Anisotropic magnetoresistance in ferromagnetic 3d alloys. *IEEE Transactions on Magnetics*, 11 :1018–1038, July 1975.

[29] W. P. Pratt, S.-F. Lee, J. M. Slaughter, R. Loloee, P. A. Schroeder, and J. Bass. Perpendicular giant magnetoresistances of ag/co multilayers. *Phys. Rev. Lett.*, 66 :3060–3063, Jun 1991. http://link.aps.org/doi/10.1103/PhysRevLett.66.3060.

[30] N. F. Mott. The electrical conductivity of transition metals. 153(880) :699–717, 1936. http://rspa.royalsocietypublishing.org/content/153/880/699.short.

[31] A. Fert and A. Campbell. Two-current conduction model in nickel. *Phys. Rev. Lett.*, 21 :1190–1192, Oct 1968. http://prl.aps.org/abstract/PRL/v21/i16/p1190_1.

[32] Julien Cucchiara. *Effets de transfert de spin dans des nanopiliers aux aimantations perpendiculaires*. PhD thesis, Université de Lorraine, 2011.

[33] Mark Stiles and Jacques Miltat. Spin-transfer torque and dynamics. In Burkard Hillebrands and AndrÃ© Thiaville, editors, *Spin Dynamics in Confined Magnetic Structures III*, volume 101 of *Topics in Applied Physics*, pages 225–308. Springer Berlin / Heidelberg, 2006. http://dx.doi.org/10.1007/10938171_7.

[34] D.C. Ralph and M.D. Stiles. Spin transfer torques. *Journal of Magnetism and Magnetic Materials*, 320(7) :1190 – 1216, 2008. `http://www.sciencedirect.com/science/article/pii/S0304885307010116`.

[35] Jiang Xiao, A. Zangwill, and M. D. Stiles. Boltzmann test of slonczewski's theory of spin-transfer torque. *Phys. Rev. B*, 70 :172405, Nov 2004. `http://link.aps.org/doi/10.1103/PhysRevB.70.172405`.

[36] J. Barnas, A. Fert, M. Gmitra, I. Weymann, and V. K. Dugaev. From giant magnetoresistance to current-induced switching by spin transfer. *Phys. Rev. B*, 72 :024426, Jul 2005.

[37] F. J. Albert, J. A. Katine, R. A. Buhrman, and D. C. Ralph. Spin-polarized current switching of a co thin film nanomagnet. *Applied Physics Letters*, 77(23) :3809–3811, 2000. `http://link.aip.org/link/?APL/77/3809/1`.

[38] Jonathan Z. Sun, T. S. Kuan, J. A. Katine, and Roger H. Koch. Spin angular momentum transfer in a current-perpendicular spin-valve nanomagnet. volume 5359, pages 445–455. SPIE, 2004. `http://link.aip.org/link/?PSI/5359/445/1`.

[39] Ya. B. Bazaliy, B. A. Jones, and S. C. Zhang. Towards metallic magnetic memory : How to interpret experimental results on magnetic switching induced by spin-polarized currents. *Journal of Applied Physics*, 89(11) :6793–6795, 2001. `http://link.aip.org/link/?JAP/89/6793/1`.

[40] A. Deac, K. J. Lee, Y. Liu, O. Redon, M. Li, P. Wang, J. P. Nozières, and B. Dieny. Current-induced magnetization switching in exchange-biased spin valves for current-perpendicular-to-plane giant magnetoresistance heads. *Phys. Rev. B*, 73 :064414, Feb 2006. `http://link.aps.org/doi/10.1103/PhysRevB.73.064414`.

[41] Jiang Xiao, A. Zangwill, and M. D. Stiles. Macrospin models of spin transfer dynamics. *Phys. Rev. B*, 72 :014446, Jul 2005. `http://link.aps.org/doi/10.1103/PhysRevB.72.014446`.

[42] S. Mangin, Y. Henry, D. Ravelosona, J. A. Katine, and Eric E. Fullerton. Reducing the critical current for spin-transfer switching of perpendicularly magnetized nanomagnets. *Applied Physics Letters*, 94(1) :012502, 2009. `http://link.aip.org/link/?APL/94/012502/1`.

[43] Ioan Tudosa, J. A. Katine, S. Mangin, and Eric E. Fullerton. Perpendicular spin-torque switching with a synthetic antiferromagnetic reference layer. *Applied Physics Letters*, 96(21) :212504, 2010. `http://link.aip.org/link/?APL/96/212504/1`.

[44] Weiwei Lin, J. Cucchiara, C. Berthelot, T. Hauet, Y. Henry, J. A. Katine, Eric E. Fullerton, and S. Mangin. Magnetic susceptibility measurements as a probe of spin transfer driven magnetization dynamics. *Applied Physics Letters*, 96(25) :252503, 2010. `http://link.aip.org/link/?APL/96/252503/1`.

[45] N. Reckers, J. Cucchiara, O. Posth, C. Hassel, F. M. Römer, R. Narkowicz, R. A. Gallardo, P. Landeros, H. Zähres, S. Mangin, J. A. Katine, E. E. Fullerton, G. Dumpich, R. Meckenstock, J. Lindner, and M. Farle. Effect of microwave irradiation on spin-torque-driven magnetization precession in nanopillars with magnetic perpendicular anisotropy. *Phys. Rev. B*, 83 :184427, May 2011. http://link.aps.org/doi/10.1103/PhysRevB.83.184427.

[46] Ru Zhu and P. B. Visscher. Spin torque switching in perpendicular films at finite temperature. *Journal of Applied Physics*, 103(7) :07A722, 2008. http://link.aip.org/link/?JAP/103/07A722/1.

[47] Takeshi Seki, Seiji Mitani, and Koki Takanashi. Nucleation-type magnetization reversal by spin-polarized current in perpendicularly magnetized fept layers. *Phys. Rev. B*, 77 :214414, Jun 2008. http://link.aps.org/doi/10.1103/PhysRevB.77.214414.

[48] U. Ebels, D. Houssameddine, I. Firastrau, D. Gusakova, C. Thirion, B. Dieny, and L. D. Buda-Prejbeanu. Macrospin description of the perpendicular polarizer-planar free-layer spin-torque oscillator. *Phys. Rev. B*, 78 :024436, Jul 2008. http://link.aps.org/doi/10.1103/PhysRevB.78.024436.

[49] I. Firastrau, U. Ebels, L. Buda-Prejbeanu, J.-C. Toussaint, C. Thirion, and B. Dieny. State diagram for spin current-induced magnetization dynamics using a perpendicular polarizer and a planar free layer. *Journal of Magnetism and Magnetic Materials*, 310(2, Part 3) :2029 – 2031, 2007. http://www.sciencedirect.com/science/article/pii/S0304885306021512.

[50] I. Firastrau, D. Gusakova, D. Houssameddine, U. Ebels, M.-C. Cyrille, B. Delaet, B. Dieny, O. Redon, J.-Ch. Toussaint, and L. D. Buda-Prejbeanu. Modeling of the perpendicular polarizer-planar free layer spin torque oscillator : Micromagnetic simulations. *Phys. Rev. B*, 78 :024437, Jul 2008. http://link.aps.org/doi/10.1103/PhysRevB.78.024437.

[51] Ri-Xing Wang, Peng-Bin He, Zai-Dong Li, An-Lian Pan, and Quan-Hui Liu. Phase diagram of magnetic multilayers with tilted dual spin torques. *Journal of Applied Physics*, 109(3) :033905, 2011. http://link.aip.org/link/?JAP/109/033905/1.

[52] G. D. Fuchs, I. N. Krivorotov, P. M. Braganca, N. C. Emley, A. G. F. Garcia, D. C. Ralph, and R. A. Buhrman. Adjustable spin torque in magnetic tunnel junctions with two fixed layers. *Applied Physics Letters*, 86(15) :152509, 2005. http://link.aip.org/link/?APL/86/152509/1.

[53] Se-Chung Oh, Seung-Young Park, Aurelien Manchon, Mairbek Chshiev, Jae-Ho Han, Hyun-Woo Lee, Jang-Eun Lee, Kyung-Tae Nam, Younghun Jo, Yo-Chan Kong, Bernard Dieny, and Kyung-Jin Lee. Bias-voltage dependence of perpendicular spin-transfer torque in asymmetric mgo-based magnetic tunnel junctions. *Nat Phys*, 5 :898–902, 2009. http://www.nature.com/nphys/journal/v5/n12/suppinfo/nphys1427_S1.html.

[54] D. C. Worledge, G. Hu, David W. Abraham, J. Z. Sun, P. L. Trouilloud, J. Nowak, S. Brown, M. C. Gaidis, E. J. O'Sullivan, and R. P. Robertazzi. Spin torque switching of perpendicular ta|cofeb|mgo-based magnetic tunnel

junctions. *Applied Physics Letters*, 98(2) :022501, 2011. `http://link.aip.org/link/?APL/98/022501/1`.

[55] J. Z. Sun, D. J. Monsma, D. W. Abraham, M. J. Rooks, and R. H. Koch. Batch-fabricated spin-injection magnetic switches. *Applied Physics Letters*, 81(12) :2202–2204, 2002. `http://link.aip.org/link/?APL/81/2202/1`.

[56] J.Z. Sun. Spin angular momentum transfer in current-perpendicular nanomagnetic junctions. *IBM journal of research and development*, 50(1) :81–100, 2006.

[57] Runge-kutta methods. `http://en.wikipedia.org/wiki/Runge-kutta`.

[58] List of runge-kutta methods. `http://en.wikipedia.org/wiki/List_of_Runge-Kutta_methods#Cash-Karp`.

[59] J. R. Cash and Alan H. Karp. A variable order runge-kutta method for initial value problems with rapidly varying right-hand sides. *ACM Trans. Math. Softw.*, 16(3) :201–222, September 1990. `http://doi.acm.org/10.1145/79505.79507`.

[60] P. F. Carcia. Perpendicular magnetic anisotropy in pd/co and pt/co thin-film layered structures. *Journal of Applied Physics*, 63(10) :5066–5073, 1988. `http://link.aip.org/link/?JAP/63/5066/1`.

[61] G. H. O. Daalderop, P. J. Kelly, and F. J. A. den Broeder. Prediction and confirmation of perpendicular magnetic anisotropy in co/ni multilayers. *Phys. Rev. Lett.*, 68 :682–685, Feb 1992. `http://link.aps.org/doi/10.1103/PhysRevLett.68.682`.

[62] J.Z Sun. Current-driven magnetic switching in manganite trilayer junctions. *Journal of Magnetism and Magnetic Materials*, 202(1) :157 – 162, 1999. `http://www.sciencedirect.com/science/article/pii/S0304885399002899`.

[63] A.D. Kent. Spintronics : A nanomagnet oscillator. *Nature Materials*, 6(6) :399–400, 2007.

[64] Thibaut Devolder. Scalability of magnetic random access memories based on an in-plane magnetized free layer. *Applied Physics Express*, 4(9) :093001, 2011. `http://apex.jsap.jp/link?APEX/4/093001/`.

[65] Hao Meng and Jian-Ping Wang. Spin transfer in nanomagnetic devices with perpendicular anisotropy. *Applied Physics Letters*, 88(17) :172506, 2006. `http://link.aip.org/link/?APL/88/172506/1`.

[66] A. D. Kent, B. Özyilmaz, and E. del Barco. Spin-transfer-induced precessional magnetization reversal. *Applied Physics Letters*, 84(19) :3897–3899, 2004. `http://link.aip.org/link/?APL/84/3897/1`.

[67] K. J. Lee, O. Redon, and B. Dieny. Analytical investigation of spin-transfer dynamics using a perpendicular-to-plane polarizer. *Applied Physics Letters*, 86(2) :022505, 2005. `http://link.aip.org/link/?APL/86/022505/1`.

[68] Hiroaki Yoda, Tatsuya Kishi, Toshihiko Nagase, Masatoshi Yoshikawa, Katsuya Nishiyama, Eiji Kitagawa, Tadaomi Daibou, Minoru Amano, Naoharu Shimomura, Shigeki Takahashi, Tadashi Kai, Masahiko Nakayama, Hisanori Aikawa, Sumio Ikegawa, Makoto Nagamine, Junichi Ozeki, Shigemi Mizukami, Mikihiko Oogane, Yasuo Ando, Shinji Yuasa, Kei Yakushiji, Hitoshi Kubota, Yoshishige Suzuki, Yoshinobu Nakatani, Terunobu Miyazaki, and Koji Ando. High efficient spin transfer torque writing on perpendicular magnetic tunnel junctions for high density mrams. *Current Applied Physics*, 10(1, Supplement) :e87 – e89, 2010. `http://www.sciencedirect.com/science/article/pii/S1567173909006087`.

[69] I. Yulaev, M. V. Lubarda, S. Mangin, V. Lomakin, and Eric E. Fullerton. Spin-transfer-torque reversal in perpendicular anisotropy spin valves with composite free layers. *Applied Physics Letters*, 99(13) :132502, 2011. `http://link.aip.org/link/?APL/99/132502/1`.

[70] Eric E. Fullerton and Stephane Mangin. Origin of the magneto[mdash]thermogalvanic voltage in cluster-assembled metallic nanostructures. *Nat Mater*, 7 :257, 2008. `http://dx.doi.org/10.1038/nmat2153a`.

[71] J. Cucchiara, Eric E. Fullerton, A. D. Kent, J. Z. Sun, Y. Henry, and S. Mangin. Current-induced magnetization reversal in terms of power dissipation. *Phys. Rev. B*, 84 :100405, Sep 2011. `http://link.aps.org/doi/10.1103/PhysRevB.84.100405`.

[72] Y. Henry, S. Mangin, J. Cucchiara, J. A. Katine, and Eric E. Fullerton. Distortion of the stoner-wohlfarth astroid by a spin-polarized current. *Phys. Rev. B*, 79 :214422, Jun 2009. `http://link.aps.org/doi/10.1103/PhysRevB.79.214422`.

[73] Vincent Cros, Olivier Boulle, J. Grollier, Amir Hamzić, M. Munoz, Luis Gustavo Pereira, and Frédéric Petroff. Spin transfer torque : a new method to excite or reverse a magnetization. *Comptes Rendus Physique*, 6(9) :956 – 965, 2005. `http://www.sciencedirect.com/science/article/pii/S1631070505001465`.

[74] Hirofumi Morise and Shiho Nakamura. Stable magnetization states under a spin-polarized current and a magnetic field. *Phys. Rev. B*, 71 :014439, Jan 2005. `http://link.aps.org/doi/10.1103/PhysRevB.71.014439`.

[75] Juhani Kurkijärvi. Intrinsic fluctuations in a superconducting ring closed with a josephson junction. *Phys. Rev. B*, 6 :832–835, Aug 1972. `http://link.aps.org/doi/10.1103/PhysRevB.6.832`.

[76] D. B. Gopman, D. Bedau, S. Mangin, C. H. Lambert, E. E. Fullerton, J. A. Katine, and A. D. Kent. Asymmetric switching behavior in perpendicularly magnetized spin-valve nanopillars due to the polarizer dipole field. *Applied Physics Letters*, 100(6) :062404, 2012. `http://link.aip.org/link/?APL/100/062404/1`.

[77] D. Ravelosona, S. Mangin, Y. Lemaho, J. A. Katine, B. D. Terris, and Eric E. Fullerton. Domain wall creation in nanostructures driven by a

spin-polarized current. *Phys. Rev. Lett.*, 96 :186604, May 2006. http://link.aps.org/doi/10.1103/PhysRevLett.96.186604.

[78] D. Ravelosona, S. Mangin, J. A. Katine, Eric E. Fullerton, and B. D. Terris. Threshold currents to move domain walls in films with perpendicular anisotropy. *Applied Physics Letters*, 90(7) :072508, 2007. http://link.aip.org/link/?APL/90/072508/1.

[79] C. Burrowes, D. Ravelosona, C. Chappert, S. Mangin, Eric E. Fullerton, J. A. Katine, and B. D. Terris. Role of pinning in current driven domain wall motion in wires with perpendicular anisotropy. *Applied Physics Letters*, 93(17) :172513, 2008. http://link.aip.org/link/?APL/93/172513/1.

[80] J. Cucchiara, Y. Henry, D. Ravelosona, D. Lacour, E. E. Fullerton, J. A. Katine, and S. Mangin. Telegraph noise due to domain wall motion driven by spin current in perpendicular magnetized nanopillars. *Applied Physics Letters*, 94(10) :102503, 2009.

[81] S. Girod, M. Gottwald, S. Andrieu, S. Mangin, J. McCord, Eric E. Fullerton, J.-M. L. Beaujour, B. J. Krishnatreya, and A. D. Kent. Strong perpendicular magnetic anisotropy in ni/co(111) single crystal superlattices. *Applied Physics Letters*, 94(26) :262504, 2009. http://link.aip.org/link/?APL/94/262504/1.

[82] David P. Bernstein, Björn Bräuer, Roopali Kukreja, Joachim Stöhr, Thomas Hauet, Julien Cucchiara, Stéphane Mangin, Jordan A. Katine, Tolek Tyliszczak, Kang W. Chou, and Yves Acremann. Nonuniform switching of the perpendicular magnetization in a spin-torque-driven magnetic nanopillar. *Phys. Rev. B*, 83 :180410, May 2011. http://link.aps.org/doi/10.1103/PhysRevB.83.180410.

[83] Ya. B. Bazaliy, B. A. Jones, and Shou-Cheng Zhang. Current-induced magnetization switching in small domains of different anisotropies. *Phys. Rev. B*, 69 :094421, Mar 2004. http://link.aps.org/doi/10.1103/PhysRevB.69.094421.

[84] H. Neal Bertram and Vladimir L. Safonov. The effect of uniaxial quartic anisotropy on thermal stability of magnetic nanograins. *Applied Physics Letters*, 79(26) :4402–4404, 2001. http://link.aip.org/link/?APL/79/4402/1.

[85] Alexander Shukh and Johannes van Ek. Micromagnetic modeling of low noise perpendicular media. *Journal of Applied Physics*, 91(10) :8375–8377, 2002. http://link.aip.org/link/?JAP/91/8375/1.

[86] O. Posth, C. Hassel, M. Spasova, G. Dumpich, J. Lindner, and S. Mangin. Influence of growth parameters on the perpendicular magnetic anisotropy of [co/ni] multilayers and its temperature dependence. *Journal of Applied Physics*, 106(2) :023919, 2009. http://link.aip.org/link/?JAP/106/023919/1.

[87] M. Gottwald, S. Andrieu, F. Gimbert, E. Shipton, L. Calmels, C. Magen, E. Snoeck, M. Liberati, T. Hauet, E. Arenholz, S. Mangin, and E. E. Fullerton. 2012. submitted.

[88] S. Ikeda, K. Miura, H. Yamamoto, K. Mizunuma, HD Gan, M. Endo, S. Kanai, J. Hayakawa, F. Matsukura, and H. Ohno. A perpendicular-anisotropy cofeb–mgo magnetic tunnel junction. *Nature Materials*, 9(9) :721–724, 2010.

[89] E. B. Myers, D. C. Ralph, J. A. Katine, R. N. Louie, and R. A. Buhrman. Current-induced switching of domains in magnetic multilayer devices. *Science*, 285(5429) :867–870, 1999. `http://www.sciencemag.org/content/285/5429/867.abstract`.

[90] J.E. Wegrowe, Q.A. Nguyen, and T.L. Wade. Measuring entropy generated by spin-transfer. *Magnetics, IEEE Transactions on*, 46(3) :866–874, 2010.

[91] Simon Granville, Haiming Yu, Julie Dubois, Laurent Gravier, and Jean-Philippe Ansermet. Temperature derivative of the resistance of spin valves. *Journal of Magnetism and Magnetic Materials*, 322(9-12) :1464 – 1466, 2010. `http://www.sciencedirect.com/science/article/pii/S030488530900290X`.

[92] Santiago Serrano-Guisan, Giulia di Domenicantonio, Mohamed Abid, Jean-Pierre Abid, Matthias Hillenkamp, Laurent Gravier, Jean-Philippe Ansermet, and Christian Felix. Enhanced magnetic field sensitivity of spin-dependent transport in cluster-assembled metallic nanostructures. *Nat Mater*, 5 :730–734, 2006. `http://www.nature.com/nmat/journal/v5/n9/suppinfo/nmat1713_S1.html`.

[93] B. Dieny, V. S. Speriosu, S. S. P. Parkin, B. A. Gurney, D. R. Wilhoit, and D. Mauri. Giant magnetoresistive in soft ferromagnetic multilayers. *Phys. Rev. B*, 43 :1297–1300, Jan 1991. `http://link.aps.org/doi/10.1103/PhysRevB.43.1297`.

Résumé

Depuis sa prédiction, le transfert de spin est devenu un sujet de recherche important et certaines applications ont déjà été commercialisées. Cependant, ce domaine laisse encore de nombreuses questions quant aux processus physiques mis en jeu. Notre travail s'est consacré à l'étude de la dynamique d'aimantation sous l'effet de transfert de spin dans des vannes de spin avec une aimantation perpendiculaire au plan, ces dernières présentant une meilleure efficacité. Pour cela, nous avons dans un premier temps développé un programme de simulation macrospin que nous avons par la suite confronté aux résultats expérimentaux.

Notre étude s'est d'abord focalisée sur les diagrammes d'état champ-courant, qui donnent une perspective globale du comportement de l'aimantation. Nous avons pu montrer que le champ extérieur ou l'anisotropie sont capables de briser la symétrie du système et ainsi expliquer la différence entre prédictions et observations. Nous avons ensuite mis en évidence des états cantés, qui sont des états où l'aimantation est figée à un angle précis.

La dernière partie de cette thèse fut consacrée à la dynamique d'aimantation à différentes échelles de temps de la seconde à la centaine de picosecondes. C'est ainsi que nous avons pu constater les limites du modèle macrospin, incapable d'expliquer les résultats expérimentaux. Nous nous sommes alors tournés vers un modèle micromagnétique, et avons pu montrer qu'il permet de mieux décrire les résultats expérimentaux.

Mots-clés : Electronique de spin, Transfert de spin, Anisotropie magnétocristalline perpendiculaire

---

Summary

Ever since its prediction, spin transfer has spawned a lot of interest, and some applications have already been commercialized. However the spin transfer effect is still not fully understood. This thesis focused on magnetization dynamics and spin transfer effect in spin valves with out of plane magnetization, proven to be more efficient. With this in mind, we developped a software simulating magnetization dynamics in spin valve. We then confronted the software with experimental results to check our model and its hypotheses veracity.

Another part of this thesis was to study current-field state diagrams, which offer a global perspective on magnetization behavior. We managed to show the applied field and the anisotropy could produce a symmetry breaking of the system and thus explain the experimental results. We were also able to highlight canted states of the magnetization. Those are frozen states of the magnetization for certain angles.

The last part describes magnetization dynamics at different time scales from a second to a hundred picoseconds. We showed the macrospin model is not appropriate for short current pulses, although we could highlight the influence of some parameters. We finally the micromagnetics model allowed for a better description of the experimental results.

Keywords : Spintronics, Spin-transfer, Perpendicular magnetocrystalline anisotropy